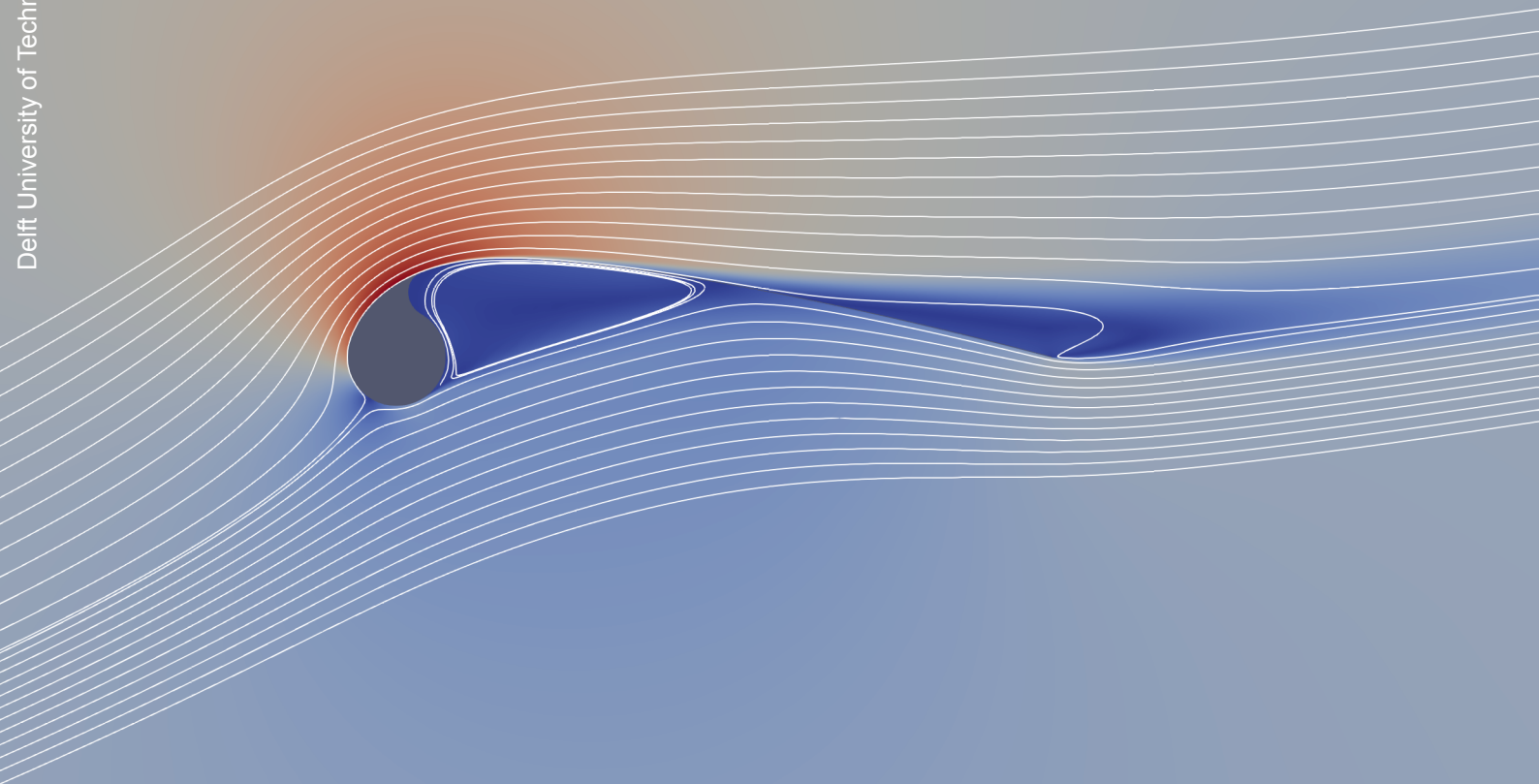


Aerodynamic Load Modelling for Leading Edge Inflatable Kites

J.P. Watchorn

Delft University of Technology





Copyright © J.P. Watchorn, 2023
All rights reserved.

Aerodynamic Load Modelling for Leading Edge Inflatable Kites

by

J.P. Watchorn

to obtain the degree of Master of Science in aerospace engineering

at the Delft University of Technology

to be defended publicly on Tuesday August 29th, 2023 at 14:30.

Student number:	4351398	
Thesis Supervisors:	Dr.-Ing. R. Schmehl,	TU Delft
	Prof.dr.ir. A.C. Viré,	TU Delft
Thesis Committee:	Dr.-Ing. R. Schmehl,	TU Delft
	Prof.dr.ir. A.C. Viré,	TU Delft
	Dr.ir. A.H. van Zuijlen	TU Delft

An electronic version of this thesis is available at <http://repository.tudelft.nl/>.

Cover image: Normalised velocity field contour and streamlines around a 2D LEI wing profile inclined at an angle-of-attack of 15° (based on simulations conducted within the scope of this study).

Preface

I first came to be aware of the concept of airborne wind energy when looking for a thesis topic. Looking at the various areas of research in aerodynamics and wind energy at the *Faculty of Aerospace Engineering*, I was instantly drawn to the *Kite Power* research group. What I found most fascinating is the fact that airborne wind energy systems are active systems requiring far less material than passive counterparts such as the conventional horizontal-axis wind turbine. As such, not only the means of generating energy is sustainable, but also the construction of the system itself.

Now after that first spark of interest comes a new body of work ready for future use, scrutiny and further development. For this, I would like to thank Roland for his guidance and supervision, as well as Jelle for his encouraging feedback. I would also like to thank Gabriel, who helped me with adapting his code for the purposes of this work. In my immediate circle, I would like to thank my parents Emilia and Peter for their support. Finally, I would like to thank my partner Jie for her care and support.

J.P. Watchorn
The Hague, August 2023

Abstract

The purpose of this study has been to develop an aerodynamic load model for leading edge inflatable (LEI) kites by means of multivariate polynomial regression analysis. The load model expresses the aerodynamic coefficients C_l , C_d and C_m as polynomial functions of the angle-of-attack α and 2D non-dimensional (relative to the chord length) shape parameters. The numerical data used for the regression analysis has been acquired from computational fluid dynamics (CFD) simulations of 2D parameterised LEI wing profiles.

The parameterisation and subsequent geometric construction of LEI wing profiles has been a key aspect of this study. The cross section of a LEI wing comprises the circular profile of the leading-edge (LE) tube, to which is attached the profile of the thin membrane canopy on the upper side near the leading edge. The thin 2D membrane canopy is equivalent to the camber line of the complete profile, implying that the highest vertical point of the membrane canopy is the maximum camber magnitude. Based on these observations, the defining non-dimensional shape parameters (relative to the chord length) are the maximum camber magnitude κ , the airfoil thickness (i.e. non-dimensional tube diameter) t and the chordwise position of maximum camber η . Parameterised profiles suitable for meshing and subsequent CFD simulation have been constructed using a smooth interpolating spline system that functions with minimal spline intersection points.

Data acquisition by means of CFD was deemed necessary since LEI kite airfoils are subject to flow separation even at relatively low angles-of-attack. Therefore, flow fields have been simulated by means of the Reynolds-averaged Navier-Stokes (RANS) equations, closed by the $k - \omega$ shear stress transport (SST) turbulence model, using the open-source CFD software OpenFOAM. Transition modelling has been omitted due to the assumption of near instant laminar-to-turbulent transition upon the flow encountering the surface of the wing due to protruding stitched seams near the leading edge. RANS simulations grant a favourable trade-off between computational cost and simulation accuracy for the purposes of this work. In this manner, viscous flow effects are captured and replicated by the revised aerodynamic load model.

In order to construct the revised aerodynamic load model, a wide range of airfoil configurations have been examined. A total of 64 unique parameterised LEI wing profiles have each been simulated at $\alpha = [0^\circ, 5^\circ, 10^\circ, 15^\circ]$ given a constant Reynolds number of 5×10^6 , leading to a total of 256 data points for the regression analysis. The parameterised profiles were generated using all possible combinations of $\eta = [0.22, 0.24, 0.26, 0.28]$, $\kappa = [0.14, 0.16, 0.18, 0.20]$ and $t = [0.06, 0.08, 0.12, 0.14]$. Whilst the fitted equations for C_d and C_m are statistically satisfactory, the fitted polynomial describing C_l is dubious due to distinct signs of over-fitting (i.e. random error is also modelled). All measurements of C_m have been taken about the quarter-chord point.

Simulation results show that the maximum camber magnitude κ and its chordwise position η generally have a more prominent effect on the flow over the suction side of a LEI wing profile, whilst the influences of the non-dimensional tube diameter t are predominantly relegated to the pressure side. In the event of the flow separating from the suction side, the chordwise position of the separation point along the surface moves further downstream for larger values of η . As such, η has a distinct impact on C_l and C_d given reversed flow over the suction side. Results also show that κ affects the flow stability at high angles-of-attack since the simulations of flow fields around profiles with $\kappa = 0.30$ given $\alpha = 15^\circ$ did not converge, thus insinuating the exacerbation of transient flow phenomena. All simulations that met the condition $t/2 \leq \kappa \leq 0.2$ given $\alpha = 15^\circ$ did converge. Nevertheless, the critical angle-of-attack decreases with increasing κ within the aforementioned range of values.

Contents

Preface	i
Abstract	ii
List of Figures	vi
List of Tables	ix
Nomenclature	x
1 Introduction	1
2 Literature Study	3
2.1 Reference Aerodynamic Load Model	3
2.1.1 Description	3
2.1.2 Derivations	4
2.1.3 Airfoil Geometry & Parameterisation	8
2.1.4 Limitations	10
2.2 Computational Fluid Dynamics (CFD) Simulation Methods	11
2.2.1 Direct Numerical Simulation (DNS)	11
2.2.2 Large-Eddy Simulation (LES)	12
2.2.3 Reynolds-Averaged Navier-Stokes (RANS) Simulation	12
2.3 In-Flight Measurements	15
2.4 Research Questions	17
3 Research Method	18
4 Computational Fluid Dynamics	20
4.1 Reynolds-Averaged Navier-Stokes (RANS) Equations	20
4.2 Turbulence Modelling	21

4.3	Discretisation	23
4.4	CFD Solver	24
4.4.1	OpenFOAM	24
4.4.2	SIMPLE Algorithm	24
5	Airfoil Geometry	27
5.1	Geometric Components, Constraints & Parameters	27
5.2	Spline Interpolation	30
6	Mesh Generation & Simulation Set-Up	32
6.1	Mesh Generation	32
6.1.1	Geometric Approximations	32
6.1.2	Mesh Characteristics & Parameters	33
6.1.3	Mesh Convergence	38
6.2	Simulation Set-Up	40
6.2.1	Simulation Platform	40
6.2.2	Boundary Conditions & Initial Values	40
6.2.3	Numerical Schemes & Solver Control Settings	42
6.2.4	Convergence Monitoring	45
7	LEI Wing Profile Aerodynamics	47
7.1	Shape Parameter Effects	47
7.1.1	Non-dimensional LE Tube Diameter t	49
7.1.2	Chordwise Position of Maximum Camber η	56
7.1.3	Maximum Camber Magnitude κ	63
7.2	Comparisons with Literature	70
8	Regression Analysis	73
8.1	Method of Least Squares	73
8.1.1	Normal Equations	73
8.1.2	QR Decomposition	74

8.2 Statistical Quality Indicators 75

8.3 Polynomial Equations of Aerodynamic Coefficients 76

9 Conclusions & Recommendations 79

Bibliography 81

List of Figures

2.1	Depiction of airfoil model where c_i denotes the horizontal distance of a node from the leading edge and L_i denotes the lift force acting on a node [7].	7
2.2	2D hybrid grid of a LEI wing profile with a chord length of 1 m [7].	8
2.3	Discrete model of LEI wing airfoil at angle-of-attack α with apparent wind velocity V_a given tube diameter d and maximum canopy height b [42].	8
2.4	Parameterised sail-wing airfoil model [17].	9
2.5	Moment coefficient C_m versus angle-of-attack α as estimated by the aerodynamic load model of Breukels [7] for LEI wing profiles with different values of camber [10].	10
2.6	2D normalised velocity field contours of the flow around a 3D LEI kite at zero angle of attack [13].	11
2.7	LEI wing lift (left plot) and drag (right plot) polars given for different Re numbers. Solid lines are with $\gamma - \overline{Re}_{\theta t}$ transition model, whereas dashed lines are without [16].	14
2.8	Protruding stitched seams near the leading edge of a LEI kite.	14
2.9	In-flight measurements of the apparent wind velocity v_a and inflow angles α_m and β_s over the time range of a representative traction phase of the V3 LEI kite model flying in AWE operations [33].	15
2.10	In-flight measurements of the apparent wind velocity and height above the ground over the full operation time of the V2 LEI kite model flying AWE manoeuvres [15]. Note that the legend is incorrect: The blue curve displays altitude measurements, whereas apparent wind velocity measurements are given by the red curve.	16
3.1	Flowchart describing the workflow of this study.	19
5.1	Geometric components and constraints of a LEI kite airfoil ($t = 0.1, \kappa = 0.1, \eta = 0.2$). . .	28
5.2	Geometric components of a LEI kite airfoil suitable for meshing ($t = 0.1, \kappa = 0.1, \eta = 0.2, t_{canopy} = 0.02$).	29
5.3	Angles $\theta_{suction}$ ($= 20^\circ$) and θ_{edge} ($= 40^\circ$) control the ends of the circular LE tube profile (close-up of Figure 5.2).	29
5.4	Comparison of LEI wing profiles with different tension parameters at spline point $(x/c, y/c) = (1, 0)$ given $t = 0.1, \kappa = 0.1, \eta = 0.2, \theta_{suction} = 20^\circ, \theta_{edge} = 40^\circ$ and $t_{canopy} = 0.02$. . .	31

6.1	LEI wing profile at the mid-section (left image) and 3D CAD model (right image) with smoothed features. The dashed line indicates the original design profile, whereas the solid line indicates the approximated filled profile [43].	33
6.2	Regions of structured mesh with O-grid topology of a LEI wing profile with shape parameters $t = 0.05$, $\kappa = 0.1$ and $\eta = 0.2$ (grid resolution of 576×201).	34
6.3	Grid point distribution along the surface of a LEI wing profile with shape parameters $t = 0.05$, $\kappa = 0.1$ and $\eta = 0.2$ (grid resolution of 576×201).	35
6.4	Mesh of the profile used to determine suitable smoothing coefficients. Shape parameters are $t = 0.15$, $\kappa = 0.3$ and $\eta = 0.4$. Grid resolution is 575×201	37
6.5	Aerodynamic coefficients per mesh refinement levels of a parameterised LEI wing airfoil with shape parameters $t = 0.15$, $\kappa = 0.3$ and $\eta = 0.4$ at $\alpha = 10^\circ$ given $Re = 5 \times 10^6$	39
6.6	Example of converged simulation of LEI wing profile with parameters $t = 0.15$, $\kappa = 0.3$ and $\eta = 0.4$ at $\alpha = 10^\circ$	45
6.7	Example of non-converged simulation of LEI wing profile with parameters $t = 0.15$, $\kappa = 0.3$ and $\eta = 0.4$ at $\alpha = 15^\circ$	46
7.1	C_l versus t given a constant $\eta = 0.22$ and varying κ	49
7.2	C_d versus t given a constant $\eta = 0.22$ and varying κ	50
7.3	C_m versus t given a constant $\eta = 0.22$ and varying κ	51
7.4	Chordwise distributions of $c_{f,x}$ for different values of t given $\alpha = 0^\circ$, $\kappa = 0.14$ and $\eta = 0.22$	52
7.5	Chordwise distributions of $c_{f,x}$ for different values of t given $\alpha = 15^\circ$, $\kappa = 0.14$ and $\eta = 0.22$	52
7.6	Chordwise distributions of C_p for different values of t given $\alpha = 0^\circ$, $\kappa = 0.14$ and $\eta = 0.22$	53
7.7	Chordwise distributions of C_p for different values of t given $\alpha = 15^\circ$, $\kappa = 0.14$ and $\eta = 0.22$	53
7.8	Visualisation of normalised flow velocity and streamlines around LEI wing profile with shape parameters $\eta = 0.22$, $\kappa = 0.14$ and $t = 0.14$ at $\alpha = 0^\circ$	54
7.9	Aerodynamic coefficients versus α for varying values of t given a constant $\eta = 0.22$ and $\kappa = 0.14$	55
7.10	C_l versus η given a constant $\kappa = 0.16$ and varying t	56
7.11	C_d versus η given a constant $\kappa = 0.16$ and varying t	57
7.12	C_m versus η given a constant $\kappa = 0.16$ and varying t	58
7.13	Chordwise distributions of $c_{f,x}$ for different values of η given $\alpha = 0^\circ$, $\kappa = 0.16$ and $t = 0.14$	59
7.14	Chordwise distributions of $c_{f,x}$ for different values of η given $\alpha = 15^\circ$, $\kappa = 0.16$ and $t = 0.14$	59
7.15	Chordwise distributions of C_p for different values of η given $\alpha = 0^\circ$, $\kappa = 0.16$ and $t = 0.14$	60
7.16	Chordwise distributions of C_p for different values of η given $\alpha = 15^\circ$, $\kappa = 0.16$ and $t = 0.14$	60

7.17	Visualisation of normalised flow velocity and streamlines around LEI wing profile with shape parameters $\eta = 0.22$, $\kappa = 0.16$ and $t = 0.14$ at $\alpha = 15^\circ$	61
7.18	Aerodynamic coefficients versus α for varying values of η given a constant $\kappa = 0.16$ and $t = 0.14$	62
7.19	C_l versus κ given a constant $\eta = 0.22$ and varying t	63
7.20	C_d versus κ given a constant $\eta = 0.22$ and varying t	64
7.21	C_m versus κ given a constant $\eta = 0.22$ and varying t	65
7.22	Chordwise distributions of $c_{f,x}$ for different values of κ given $\alpha = 0^\circ$, $\eta = 0.22$ and $t = 0.14$	66
7.23	Chordwise distributions of $c_{f,x}$ for different values of κ given $\alpha = 15^\circ$, $\eta = 0.22$ and $t = 0.14$	66
7.24	Chordwise distributions of C_p for different values of κ given $\alpha = 0^\circ$, $\eta = 0.22$ and $t = 0.14$	67
7.25	Chordwise distributions of C_p for different values of κ given $\alpha = 15^\circ$, $\eta = 0.22$ and $t = 0.14$	67
7.26	Visualisation of normalised flow velocity and streamlines around LEI wing profile with shape parameters $\eta = 0.22$, $\kappa = 0.20$ and $t = 0.14$ at $\alpha = 15^\circ$	68
7.27	Aerodynamic coefficients versus α for varying values of κ given a constant $\eta = 0.22$ and $t = 0.14$	69
7.28	Aerodynamic coefficients computed in this study (solid lines) compared to numerical results from the work of Folkersma et al. [21] (dashed lines). The shape parameters κ and η of the airfoil examined in the study of Folkersma et al. [21] have been estimated according to the definitions used in this study (see Section 2.1.3).	70
7.29	Turbulence intensity contour plot from the work of Breukels [7]. The displayed LEI wing profile is inclined at $\alpha = 0^\circ$ and has a camber of 8% according to the definition of "airfoil camber" used by Breukels [7]. According to the definition of "maximum camber magnitude" used in this study, $\kappa \approx 0.17$ for the displayed airfoil.	71
7.30	Aerodynamic coefficients computed in this study (solid lines) compared to numerical results from the work of Breukels [7] (dashed lines). Note that the maximum camber magnitude κ of the reference has been estimated according to the definition used in this study (see Section 2.1.3).	72
8.1	Example plots of aerodynamic coefficients versus α given a constant $\eta = 0.22$ and $t = 0.06$	77

List of Tables

2.1	Numerical values of coefficients governing Equation (2.4). [8]	5
2.2	Numerical values of coefficients governing Equation (2.6). [8]	5
2.3	Numerical values of coefficients governing Equation (2.7). [8]	6
4.1	Empirical constants of $k - \omega$ SST model [32]	23
5.1	Values of fixed geometric parameters used to construct LEI wing profiles for meshing and simulation.	30
6.1	Values of hyperbolic extrusion smoothing parameters (see visual representations Figure 6.2 and Figure 6.4).	37
6.2	Computed aerodynamic coefficients (rounded to three significant figures) given $Re = 5 \times 10^6$ for different mesh resolutions tangent to the surface of an airfoil with shape parameter specifications $t = 0.15$, $\kappa = 0.3$ and $\eta = 0.4$.	38
6.3	Computed aerodynamic coefficients (rounded to three significant figures) given $\alpha = 10^\circ$ for different mesh resolutions normal to the surface of an airfoil with shape parameter specifications $t = 0.15$, $\kappa = 0.3$ and $\eta = 0.4$.	39
6.4	OpenFOAM initial values and boundary conditions	41
6.5	Applied numerical schemes	43
6.6	Applied solver control settings	44
8.1	Parameter estimates governing Equation (8.11) [$R^2 = 0.9582$, $RMSE = 0.1181$].	78
8.2	Parameter estimates governing Equation (8.12) [$R^2 = 0.8971$, $RMSE = 0.0184$].	78
8.3	Parameter estimates governing Equation (8.13) [$R^2 = 0.9791$, $RMSE = 0.0088$].	78

Nomenclature

Acronyms

2D	Two-dimensional
3D	Three-dimensional
AoA	Angle-of-Attack
AWE	Airborne Wind Energy
AWES	Airborne Wind Energy System
BST	Baseline Stress Transport
CAD	Computer-Aided Design
CFD	Computational Fluid Dynamics
DNS	Direct Numerical Simulation
FDM	Finite Difference Method
FEM	Finite Element Method
FSI	Fluid-Structure Interaction
FVM	Finite Volume Method
GAMG	Geometric agglomerated Algebraic Multi-Grid
HAWT	Horizontal-Axis Wind Turbine
KCU	Kite Control Unit
LE	Leading Edge
LEI	Leading Edge Inflatable
LES	Large-Eddy Simulation
NACA	National Advisory Committee for Aeronautics
RANS	Reynolds-Averaged Navier-Stokes
SIMPLE	Semi-Implicit Method for Pressure Linked Equations
SIMPLEC	Semi-Implicit Method for Pressure Linked Equations Consistent
SST	Shear Stress Transport
TE	Trailing Edge
TKE	Turbulent Kinetic Energy

Latin Symbols

c	Chord length
-----	--------------

m

C_d	2D drag coefficient	[–]
c_f	Local skin friction coefficient	[–]
$c_{f,x}$	Streamwise component of local skin friction coefficient	[–]
C_l	2D lift coefficient	[–]
C_m	2D moment coefficient	[–]
C_p	Pressure coefficient	[–]
D	Aerodynamic drag	kg m s^{-2}
I	Turbulence intensity	[–]
k	Turbulent kinetic energy	$\text{m}^2 \text{s}^{-2}$
L	Aerodynamic lift	kg m s^{-2}
M	Aerodynamic moment	$\text{kg m}^2 \text{s}^{-2}$
p	Pressure	$\text{kg m}^{-1} \text{s}^{-2}$
Re	Reynolds number	[–]
$\widetilde{\text{Re}}_{\theta t}$	Transition onset momentum thickness Reynolds number	[–]
S_r	Reference area (for 2D cases $S_r = c \cdot 1$)	m^2
t	Non-dimensional tube diameter (relative to c)	[–]
t_{canopy}	Non-dimensional membrane canopy thickness (relative to c)	[–]
U_∞	Free-stream velocity magnitude	m s^{-1}
u_τ	Friction velocity	m s^{-1}
v_a	Apparent wind speed	m s^{-1}
v_k	Velocity of the kite	m s^{-1}
v_w	Wind speed	m s^{-1}
y^*	Non-dimensional wall distance, turbulent kinetic energy based	[–]
y^+	Non-dimensional wall distance, wall shear stress based	[–]

Greek Symbols

α	Angle-of-attack	$^\circ$
γ	Intermittency parameter	[–]
δ_{ij}	Kronecker delta	[–]
ϵ	Turbulent dissipation rate	$\text{m}^2 \text{s}^{-3}$
η	Max. camber chordwise position (relative to c)	[–]
θ_{edge}	Angular position of edge-tube intersection point (relative to LE tube centre)	$^\circ$
$\theta_{suction}$	Angular position of tube-canopy intersection point (relative to LE tube centre)	$^\circ$
κ	Max. camber magnitude (relative to c)	[–]
μ	Dynamic viscosity	$\text{kg m}^{-1} \text{s}^{-1}$

ν	Kinematic viscosity	$\text{m}^2 \text{s}^{-1}$
ν_t	Eddy viscosity	$\text{m}^2 \text{s}^{-1}$
ρ	Density	kg m^{-3}
τ_w	Wall shear stress	$\text{kg m}^{-1} \text{s}^{-2}$
$\tau_{w,x}$	Streamwise component of wall shear stress	$\text{kg m}^{-1} \text{s}^{-2}$
ω	Specific turbulent dissipation rate	s^{-1}

Introduction

With the rapid onset of climate change and the increasing scarcity of natural resources, there is a greater urgency for modern industrialised societies to transition from a predominantly fossil-fuel based energy infrastructure to a fully renewable one. Among the most prominent sources of renewable energy is wind energy, which is conventionally harnessed with both on- and off-shore horizontal-axis wind turbines (HAWTs) that form part of the contemporary (partially renewable) energy infrastructure. However, material and structural constraints impose height restrictions on conventional wind turbines, preventing them from harvesting energy from stronger high-altitude winds [3, 43]. In order to take advantage of the larger energy potential further up in the Earth's atmosphere, one can resort to airborne wind energy (AWE) systems. A novel form of wind energy conversion, it is increasingly becoming a viable alternative to conventional wind turbines.

There is a diverse range of AWE systems currently in development. For example, there are concepts that incorporate lighter-than-air aircraft, vertical take-off and landing drones, or wings that fly in a cross-wind manoeuvre, just to name a few [1, 38]. This thesis concerns the last mentioned AWE concept, where the wing in question is attached to a tether that drives a generator on the ground. More specifically, there will be a focus on soft membrane wings more commonly associated with recreational sports such as paragliding or kite-surfing [1, 38]. The scope of this project is further narrowed down to investigating leading edge inflatable (LEI) kites, where the membrane canopy is rigidised by (as the name suggests) an inflatable tube at the leading edge of the wing, along with inflatable chordwise struts stationed at intervals along the span [29]. Sharing similar structural characteristics and application methods, ram-air kites are also categorised as "flexible" or "soft" membrane wings. In this case, the wing is made up of membrane cells with openings at the leading edge, whereby the incoming flow pressurises the wing [22].

A common characteristic of lightweight membrane wings is that they are flexible structures, implying that aerodynamic loads lead to large structural deformations (compared to wings with more rigid structures). Therefore, LEI and ram-air kites pose a strongly coupled fluid-structure interaction (FSI) problem [21, 22, 43]. A pure aerodynamic analysis, in which the membrane wing is assumed to be a rigid body, does provide insight into the flow field around the kite (as shown by Viré et al. [43] and Folkersma et al. [21] for LEI kites). But the omission of structural deformations is an approximation that neglects the substantial aeroelastic effects observed in flight. A more accurate representation of the flow field would account for load and design shape changes due to fluid-structure interactions, as considered by Folkersma et al. [22] for ram-air kites and by Bosch et al. [5] for LEI wings. Both FSI studies applied a partitioned two-way coupling scheme in which the aeroelastic simulation framework comprises individual aerodynamic and structural solvers. The work of Bosch et al. [5] made use of the two-dimensional LEI wing load model developed by Breukels [7] as the aerodynamic solver component.

The aerodynamic load model developed by Breukels [7] estimates the surface loading of a LEI kite. Results from two-dimensional computational fluid dynamics (CFD) simulations served as the basis of this polynomial regression model describing the aerodynamic lift, drag and moment coefficients as functions of the angle-of-attack and non-dimensional shape parameters. A versatile tool for preliminary calculations, its limitations nonetheless necessitate a thorough revision. As argued by van Kappel [42] and Cayon [10], including the chordwise position of maximum camber as an input parameter is expected to produce an improved two-dimensional load model that more accurately captures the surface loading of a LEI kite. As such, the main goal of this project is to revise the aerodynamic load model developed by Breukels [7] for LEI wings.

Therefore, the research objective of this thesis is:

“To develop a CFD based polynomial regression model that accurately describes the aerodynamic wing loading of a leading edge inflatable kite used in airborne wind energy operations”

The above stated research objective has served as a guide for the literature review, the findings of which can be found in Chapter 2. Stemming from the literature study is the research plan of this thesis given in Chapter 3. In Chapter 4, the underlying theory of CFD has been described as it is the means by which flow fields have been simulated in this study. Afterwards is an explanation of how the parameterised LEI wing profiles have been constructed in Chapter 5, followed by descriptions of the method of mesh generation and the simulation set-up in Chapter 6. The numerical data acquired from the CFD simulations has been visualised, plotted and scrutinised in Chapter 7, then utilised for the development of the aerodynamic load model in Chapter 8. Finally, the conclusions of this study and recommendations for further research are to be found in Chapter 9.

2

Literature Study

The following chapter presents the findings of the literature study, starting with a summary and scrutiny of the reference aerodynamic load model devised by Breukels [7] in Section 2.1. This chapter concludes with an examination of the leading CFD simulation methods in Section 2.2, also comprising a discussion of the results attained from studies of 2D and 3D LEI wing aerodynamics.

2.1. Reference Aerodynamic Load Model

The following section describes and examines the aerodynamic load model developed by Breukels [7] since the research objective of this thesis is to revise it. The derivations of the equations used in the model have been reproduced. This section concludes with a discussion of the limitations that arise from the applied approximations.

2.1.1. Description

The steady-state aerodynamic load model developed by Breukels [7] is a polynomial regression model that expresses the local aerodynamic coefficients of a LEI wing as functions of non-dimensional airfoil shape parameters and local inflow conditions. More specifically, the independent variables are the airfoil thickness t , camber κ and angle-of-attack α :

$$C_l = f(\alpha, \kappa, t)$$

$$C_d = g(\alpha, \kappa, t)$$

$$C_m = h(\alpha, \kappa, t)$$

Assuming a circular profile, the diameter of the leading edge tube is controlled via the shape parameter t . The profile of the membrane canopy is assumed to have the shape of a concave downward curve that is equivalent to the mean camber line. The vertical position of the maximum camber point defines the shape of the canopy (i.e. the mean camber line), which is controlled via the shape parameter κ . It should be noted that the horizontal position of the maximum camber point is invariable. Both shape parameters are non-dimensional.

As described by de Groot et al. [14], the load model solely relies on static input parameters (i.e. time invariant), implying that the outputs are instantaneous values. The inclusion of time derivatives would account for the effects of continuous structural deformations due to aerodynamic loads. However,

changes in canopy shape as a result of structural deformations are not known *a priori*, thus necessitating the omission of time-dependent variables.

A two-dimensional LEI wing undergoes flow separation even at relatively low angles-of-attack [5]. Therefore, in order to incorporate viscous effects into the aerodynamic load model, Breukels [7] conducted two-dimensional steady-state CFD simulations of a wide combination of airfoil shapes and inflow conditions. The numerical measurements acquired from the simulations were subsequently used as the basis of the polynomial regression analysis, leading to the approximating equations described in Section 2.1.2.

2.1.2. Derivations

The derivations presented by Breukels [7] give insight into the assumptions and approximations used to develop the load model. The modelling of the aerodynamic coefficients has been summarised, followed by a description of the lift distribution and calculation of the airfoil moment.

Aerodynamic Coefficients

The derivation of the empirical model starts with a polynomial regression analysis, which is a statistical process in which the relationship between a dependent variable and a set of independent variables is approximated as a polynomial. The relationship between the values of the independent variables and the corresponding conditional mean of the dependent variable is modelled as non-linear.

Where simple linear regression may fail to produce a suitable model, polynomial regression analysis can serve as an alternative solution. Such is the case when modelling the lift coefficient in terms of the angle-of-attack, which is represented by a third order polynomial within the range $-20^\circ \leq \alpha \leq 20^\circ$ [7]:

$$C_l = \lambda_1 \alpha^3 + \lambda_2 \alpha^2 + \lambda_3 \alpha + \lambda_4, \quad -20^\circ \leq \alpha \leq 20^\circ \quad (2.1)$$

Breukels [7] continued the derivation by expressing the coefficients λ_n in terms of the camber magnitude κ as first order polynomials:

$$\lambda_1 = S_1 \kappa + S_2 \quad (2.2a)$$

$$\lambda_2 = S_3 \kappa + S_4 \quad (2.2b)$$

$$\lambda_3 = S_5 \kappa + S_6 \quad (2.2c)$$

$$\lambda_4 = S_7 \kappa + S_8 \quad (2.2d)$$

Second order polynomials represent the coefficients S_n in terms of the airfoil thickness t :

$$S_1 = C_1 t^2 + C_2 t + C_3 \quad (2.3a)$$

$$S_2 = C_4 t^2 + C_5 t + C_6 \quad (2.3b)$$

$$S_3 = C_7 t^2 + C_8 t + C_9 \quad (2.3c)$$

$$S_4 = C_{10} t^2 + C_{11} t + C_{12} \quad (2.3d)$$

$$S_5 = C_{13} t^2 + C_{14} t + C_{15} \quad (2.3e)$$

$$S_6 = C_{16} t^2 + C_{17} t + C_{18} \quad (2.3f)$$

$$S_7 = C_{19} t^2 + C_{20} t + C_{21} \quad (2.3g)$$

$$S_8 = C_{22} t^2 + C_{23} t + C_{24} \quad (2.3h)$$

The final stage of the derivation gives the lift coefficient as a function of the camber magnitude κ , airfoil

thickness t and angle-of-attack α :

$$\begin{aligned}
C_l = & [(C_1 t^2 + C_2 t + C_3) \kappa + (C_4 t^2 + C_5 t + C_6)] \alpha^3 \\
& + [(C_7 t^2 + C_8 t + C_9) \kappa + (C_{10} t^2 + C_{11} t + C_{12})] \alpha^2 \\
& + [(C_{13} t^2 + C_{14} t + C_{15}) \kappa + (C_{16} t^2 + C_{17} t + C_{18})] \alpha \\
& + [(C_{19} t^2 + C_{20} t + C_{21}) \kappa + (C_{22} t^2 + C_{23} t + C_{24})], \quad -20^\circ \leq \alpha \leq 20^\circ
\end{aligned} \tag{2.4}$$

Data fitting using the method of least squares resulted in the following values of the coefficients C_n :

Table 2.1: Numerical values of coefficients governing Equation (2.4). [8]

C_n	Value	C_n	Value
C_1	-0.008 011	C_{13}	0
C_2	-0.000 336	C_{14}	0
C_3	0.000 992	C_{15}	0
C_4	0.013 936	C_{16}	-3.371 000
C_5	-0.003 838	C_{17}	0.858 039
C_6	-0.000 161	C_{18}	0.141 600
C_7	0.001 243	C_{19}	7.201 140
C_8	-0.009 288	C_{20}	-0.676 007
C_9	-0.002 124	C_{21}	0.806 629
C_{10}	0.012 267	C_{22}	0.170 454
C_{11}	-0.002 398	C_{23}	-0.390 563
C_{12}	-0.000 274	C_{24}	0.101 966

The fidelity of the empirical model was subsequently scrutinised by calculating the statistical error introduced by the regression analysis. The type of error under consideration, which regards discrepancies between the CFD data and the empirical model, is defined as follows:

$$\varepsilon = \frac{\sqrt{\sum_{i=1}^n (C_{l,fit} - C_{l,CFD})^2}}{\sqrt{\sum_{i=1}^n (C_{l,CFD})^2}} \tag{2.5}$$

Based on Equation (2.5), the data fitting error calculated by Breukels [7] amounts to approximately 5.5%.

Similar steps were taken with regard to modelling the drag and moment coefficients (Breukels [7] has omitted the derivation of Equation (2.6) and Equation (2.7)). The drag coefficient as a function of camber magnitude κ , airfoil thickness t and angle-of-attack α is:

$$\begin{aligned}
C_d = & [(C_{25} t + C_{26}) \kappa^2 + (C_{27} t + C_{28}) \kappa + (C_{29} t + C_{30})] \alpha^2 \\
& + [(C_{31} t + C_{32}) \kappa + (C_{33} t^2 + C_{34} t + C_{35})], \quad -20^\circ \leq \alpha \leq 20^\circ
\end{aligned} \tag{2.6}$$

Table 2.2: Numerical values of coefficients governing Equation (2.6). [8]

C_n	Value	C_n	Value
C_{25}	0.546 094	C_{31}	0.123 685
C_{26}	0.022 247	C_{32}	0.143 755
C_{27}	-0.071 462	C_{33}	0.495 159
C_{28}	-0.006 527	C_{34}	-0.105 362
C_{29}	0.002 733	C_{35}	0.033 468
C_{30}	0.000 686		

The moment coefficient in terms of the same independent variables is:

$$C_m = [(C_{36}t + C_{37})\kappa + (C_{38}t + C_{39})]\alpha^2 + [(C_{40}t + C_{41})\kappa + (C_{42}t + C_{43})], \quad -20^\circ \leq \alpha \leq 20^\circ \quad (2.7)$$

Table 2.3: Numerical values of coefficients governing Equation (2.7). [8]

C_n	Value	C_n	Value
C_{36}	-0.284 793	C_{41}	-1.787 703
C_{37}	-0.026 199	C_{42}	0.352 443
C_{39}	-0.024 060	C_{43}	-0.839 323
C_{40}	0.000 559	C_{44}	0.137 932

This concludes the modelling of the aerodynamic coefficients within the range $-20^\circ \leq \alpha \leq 20^\circ$. Beyond the bounds of this range, the steady-state assumption is no longer valid due to unsteady flow. Accurately capturing transient flow phenomena observed beyond the given range would necessitate the acquisition of data via a computationally expensive transient solver.

Based on the work of Spierenburg [40], Breukels [7] assumes similar aerodynamic characteristics to the flow over a flat plate for $-180^\circ \leq \alpha \leq -20^\circ$ and $20^\circ \leq \alpha \leq 180^\circ$, leading to the following equations:

$$C_l = 2 \cos(\alpha) \sin^2(\alpha) \quad (2.8)$$

$$C_d = 2 \sin^3(\alpha) \quad (2.9)$$

Equation (2.8) and Equation (2.9) are empirical relations that express respectively the lift coefficient and drag coefficient of a flat plate solely as functions of the angle-of-attack. With the intent of developing continuously differentiable functions, a step function permits switching between the equations applicable to the *operational range* ($-20^\circ \leq \alpha \leq 20^\circ$) and the *non-operational range* ($-180^\circ \leq \alpha \leq -20^\circ$ or $20^\circ \leq \alpha \leq 180^\circ$).

Airfoil Moment

Along with the aerodynamic coefficients, Breukels [7] also modelled the chordwise distribution of lift and the subsequent aerodynamic moment acting on the airfoil. A schematic representation of the lift distribution is displayed in Figure 2.1 which depicts a discrete model comprised of five nodes acting as load points. The total lift acting on the airfoil is the sum of the lift forces acting on the nodes:

$$L = L_1 + L_2 + L_3 + L_4 + L_5$$

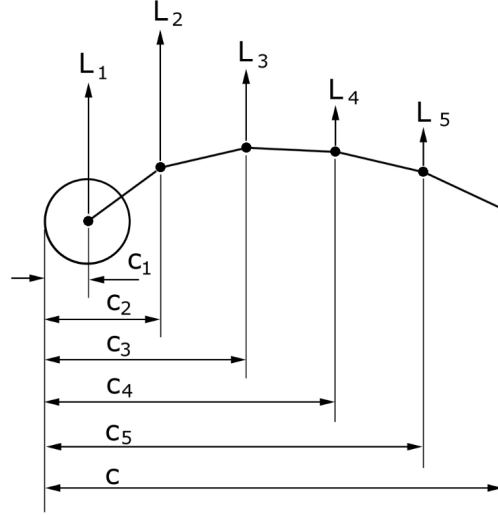


Figure 2.1: Depiction of airfoil model where c_i denotes the horizontal distance of a node from the leading edge and L_i denotes the lift force acting on a node [7].

Pressure data from CFD simulations was used to develop the airfoil model depicted in Figure 2.1 since the pressure distribution across the surface of an airfoil dictates the chordwise load distribution. The drag forces acting on the nodes are assumed to have a negligible effect on the aerodynamic moment due to smaller magnitudes and moment arms relative to the nodal lift forces.

An aerodynamic moment acts on an airfoil if the resultant aerodynamic force is not applied at the centre of pressure. Such is the case for the airfoil model displayed in Figure 2.1, where the resultant aerodynamic force is assumed to act at the quarter chord point $c/4$. Knowing this, the aerodynamic moment expressed as a function of the nodal lift forces is:

$$M = L_1 \left(\frac{1}{4}c - c_1 \right) + L_2 \left(\frac{1}{4}c - c_2 \right) + L_3 \left(\frac{1}{4}c - c_3 \right) + L_4 \left(\frac{1}{4}c - c_4 \right) + L_5 \left(\frac{1}{4}c - c_5 \right) \quad (2.10)$$

The aerodynamic forces acting on the nodes are dependent on the inflow conditions and the geometry of the airfoil. The distribution of lift was discretised using weight factors w_i that account for varying inflow conditions. Introducing these weight factors along with terms that govern their rate of variation (denoted by u_i) into the model leads to the following:

$$L = L(w_1 + u_1 a) + L(w_2 + u_2 a) + L(w_3 + u_3 a) + L(w_4 + u_4 a) + L(w_5 + u_5 a) \quad (2.11a)$$

$$w_1 + w_2 + w_3 + w_4 + w_5 = 1 \quad (2.11b)$$

$$u_1 + u_2 + u_3 + u_4 + u_5 = 0 \quad (2.11c)$$

The w_i and u_i terms act as constant coefficients, implying that the variable a controls the lift distribution and aerodynamic moment at a constant total lift L . Given Equation (2.11) and Equation (2.10), one can solve for the arbitrary increment of change variable a :

$$a = \frac{\frac{1}{4}c - (w_1 c_1 + w_2 c_2 + w_3 c_3 + w_4 c_4 + w_5 c_5) - \frac{M}{L}}{u_1 c_1 + u_2 c_2 + u_3 c_3 + u_4 c_4 + u_5 c_5} \quad (2.12)$$

According to this model, the correct aerodynamic moment is acquired by varying the lift force.

2.1.3. Airfoil Geometry & Parameterisation

When simulating the flow field around a LEI wing cross-section, one must come to terms with the fact that there are no standard and widely accepted equations defining the shape of such a profile. In order to construct a LEI wing profile suitable for meshing and subsequent aerodynamic simulations, Folkersma et al. [21] relied on spline interpolations using spatial coordinate files likely acquired from the kite design software tool SurfPlan™. The same method has been applied in the work of Deaves [15] and Sachdeva [37]. However, the availability of such spatial coordinate files is limited and the range of profile shapes arising from the spline interpolations is not extensive enough for the purposes of this study. The method of Breukels [7] overcomes this limitation by resorting to airfoil parameterisation, similarly observed in conventional airfoils such as the NACA series. This method permits a wider range of airfoil configurations necessary for a polynomial regression analysis. However, the method used to generate the profile geometry with the assigned airfoil shape parameters has not been explicitly described, nor is it clear how the shape parameters are defined.

Given the unconventional design shape of a LEI wing profile, further elaboration of how the shape parameters are defined and control the airfoil geometry should be a prerequisite in order to impart a correct interpretation of the load model. The airfoil shape parameters in question are referred to as the “thickness” t and “camber” κ in the work of Breukels [7]. The former shape parameter is said to affect the radius of the leading-edge tube, which has a distinct circular profile evident in Figure 2.2. What is not apparent though is how the thin membrane canopy is generated and at which points the suction and pressure sides merge with the leading-edge tube. Nor is the position of the trailing edge relative to the leading-edge tube clear.

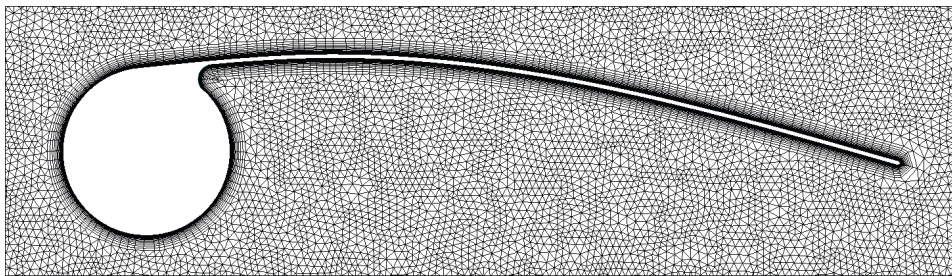


Figure 2.2: 2D hybrid grid of a LEI wing profile with a chord length of 1 m [7].

The ambiguity of the primary source necessitates a deeper scrutiny of studies that have attempted to interpret and subsequently utilise the original aerodynamic load model. The studies of van Kappel [42] and Berens [4] have applied the interpretation visualised in Figure 2.3 and define the airfoil shape parameters t and κ as non-dimensional relative to the chord length c .

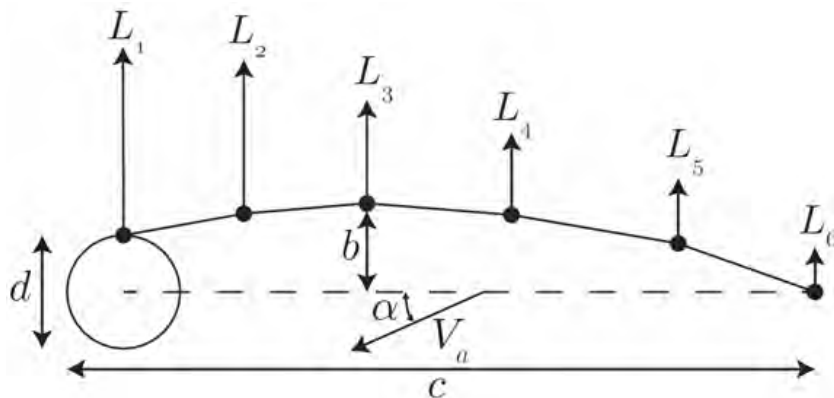


Figure 2.3: Discrete model of LEI wing airfoil at angle-of-attack α with apparent wind velocity V_a given tube diameter d and maximum canopy height b [42].

Using the same notation as in Figure 2.3, van Kappel [42], Berens [4] and Bosch [6] all apply the same definitions of the non-dimensional airfoil parameters (similarly employed by the kite design software tool SurfPlan™, but with different terminologies):

- The airfoil thickness t is the tube diameter d relative to the chord length c (also referred to as the “non-dimensional tube diameter”): $t = \frac{d}{c}$
- The airfoil camber κ is the maximum canopy height b relative to the chord length c (also referred to as the “maximum camber magnitude”): $\kappa = \frac{b}{c}$

The above definitions give rise to an inconsistency with the source material since Breukels [7] claims to have conducted simulations with zero-cambered airfoils ($\kappa = 0$). Judging from Figure 2.2 and Figure 2.3, such a configuration is intuitively improbable with the given definition of camber since it would lead to an impractical shape without the characteristic concave downward curvature of the membrane canopy. Another observation from both Figure 2.2 and Figure 2.3 is the fact that the tube radius $d/2$ cannot exceed the maximum canopy height b since a violation of this condition would similarly lead to an impractical shape of the membrane canopy and eliminate the concave downward curvature. From this, another inconsistency with the source material arises since Breukels [7] claims the profile displayed in Figure 2.2 has a “thickness” of 20% and a “camber” of 4%. If applying the same definitions and assuming the percentages are relative to the chord length, then the shape of the membrane canopy of the profile displayed in Figure 2.2 is incompatible with the alleged non-dimensional shape parameters. As such, Breukels [7] has either provided erroneous values or applied different definitions of the non-dimensional parameters.

Upon closer examination, it seems to be the case that the definition of camber as the maximum canopy height b relative to the chord length c is a misinterpretation. It would appear that the actual definitions of the non-dimensional shape parameters applied by Breukels [7] are based on the method of sail-wing airfoil parameterisation utilised by den Boer [17], which has been visualised in Figure 2.4. The reason behind this assumption is the fact that Breukels [7] makes comparisons with the wind-tunnel measurements of den Boer [17], specifically scrutinising differences in airfoil shape given the same flow conditions. According to den Boer [17], “camber” is defined as the orthogonal distance, relative to the chord length, between the straight line connecting the canopy-tube intersection point to the trailing edge and the parallel line tangent to the vertex (i.e. turning point) of the curved canopy. Therefore, according to this definition, the sail-wing profile displayed in Figure 2.4 has a camber of 10%. This interpretation of camber is consistent with the profile displayed in Figure 2.2 and allows for a zero cambered airfoil configuration in which the membrane canopy shape has no curvature and is thus represented by the straight line from the canopy-tube intersection point to the trailing edge. The interpretation of airfoil “thickness” as the diameter of the leading-edge tube d relative to the chord length c appears to be correct since the same manner of non-dimensionalisation has been applied to the circular profile displayed in Figure 2.4 (but has not been referred to as “thickness” in the work of den Boer [17]). On these grounds, the airfoil displayed in Figure 2.4 has a thickness of 6.70%.

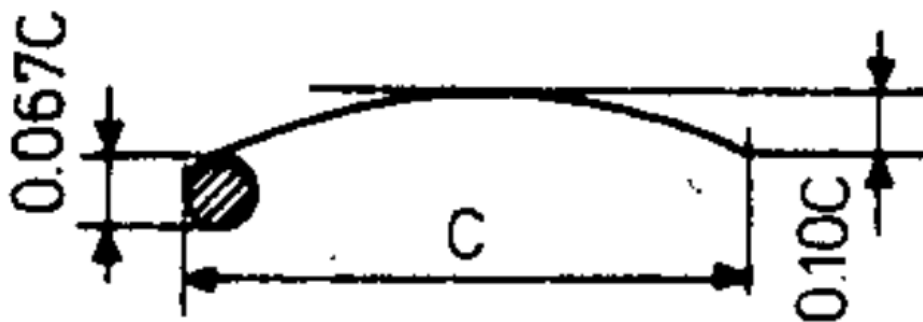


Figure 2.4: Parameterised sail-wing airfoil model [17].

Nevertheless, the definitions of the non-dimensional airfoil parameters based on Figure 2.3 have been used as the basis of the revised aerodynamic load model in order to promote compatibility with SurfPlan™. The assumption of a vertical alignment between the trailing edge and the centre of the circular leading-edge tube profile evident in Figure 2.3 has also been adopted in this work since this also features in LEI profiles created with SurfPlan™.

2.1.4. Limitations

The aerodynamic load model of Breukels [7] has seen extensive use as an aerodynamic solver in aeroelastic studies of LEI kites. As such, the limitations of the polynomial regression model are evident and well documented.

In the studies of van Kappel [42] and Cayon [10], the accuracy of the moment coefficient C_m estimator has been called into question due to poor predictions, especially with regard to high angle-of-attack flows that fall within the $-20^\circ \leq \alpha \leq 20^\circ$ range of applicability. Figure 2.5 shows that the magnitude of the moment coefficient estimated by the model of Breukels [7] can reach higher than $|C_m| = 1$ within the given angle-of-attack range of applicability. But the CFD results used to conduct the regression analysis show that the magnitude of the moment coefficient does not exceed $|C_m| = 0.3$ given the same camber and within the same range of angle-of-attack [7]. Such a large discrepancy warrants a revision and redevelopment of the aerodynamic load model.

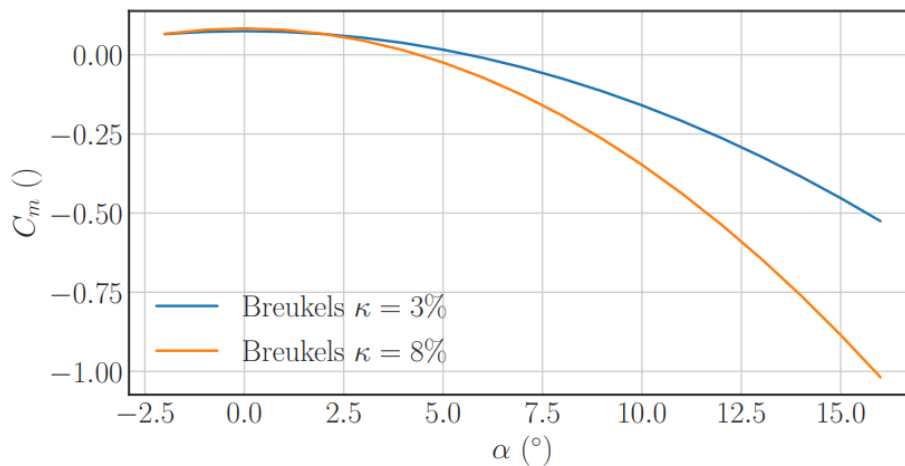


Figure 2.5: Moment coefficient C_m versus angle-of-attack α as estimated by the aerodynamic load model of Breukels [7] for LEI wing profiles with different values of camber [10].

Another point of contention regarding the work of Breukels [7] is the omission of a mesh convergence study, a crucial aspect of the mesh generation process in order to select a grid resolution that facilitates a suitable balance between simulation accuracy and computational cost. Furthermore, the Reynolds number used to simulate the flow fields has not been specified. This complicates the process of comparing the numerical data attained for the purposes of this work with the results of Breukels [7] since a defining characteristic of the simulated flow fields is unknown.

2.2. Computational Fluid Dynamics (CFD) Simulation Methods

The present section describes the available CFD simulation methods that are suitable for modelling incompressible flow fields. The results from past studies provide valuable insight on the flow characteristics since a high level of detail can be achieved using these methods. As such, the CFD methods described here are the most suitable aerodynamic modelling approaches if the goal is to accurately simulate the flow physics of an airfoil.

2.2.1. Direct Numerical Simulation (DNS)

On a conceptual level, a direct numerical simulation is the most straightforward approach with regards to the simulation of turbulence. The full range of spatial and temporal scales of turbulent motion are resolved, thus eliminating the need for a turbulence model. The fact that the Navier-Stokes equations are solved for all scales of motion implies that DNS is the most accurate approach for simulating turbulence. However, the high level of accuracy comes at a significant computational cost that scales with Re_L^3 . As such, DNS is limited to low Reynolds number flows and is typically reserved for fundamental research rather than practical engineering applications. [19, 36]

Nevertheless, DNS studies of the flow over a three-dimensional rigid model of a LEI kite have been carried out, such as the analysis conducted by Coudou [13] for unsteady flow at $Re = 1000$ and $Re = 5000$. Judging from Figure 2.6, the flow recirculates behind the leading edge at both Reynolds numbers, but appears to be much less turbulent at $Re = 1000$ than at $Re = 5000$. At $Re = 5000$, one can also distinguish a faint recirculating bubble at the trailing edge on the suction side of the canopy in Figure 2.6b. The strong interaction between the canopy and the vortices shed by the leading edge at $Re = 5000$ is also expected to occur at higher Reynolds number flows. Simulating the flow around the LEI wing at moderate-to-high Reynolds numbers will require the application of a turbulence model in order to avoid the excessively high computational costs encountered with DNS.

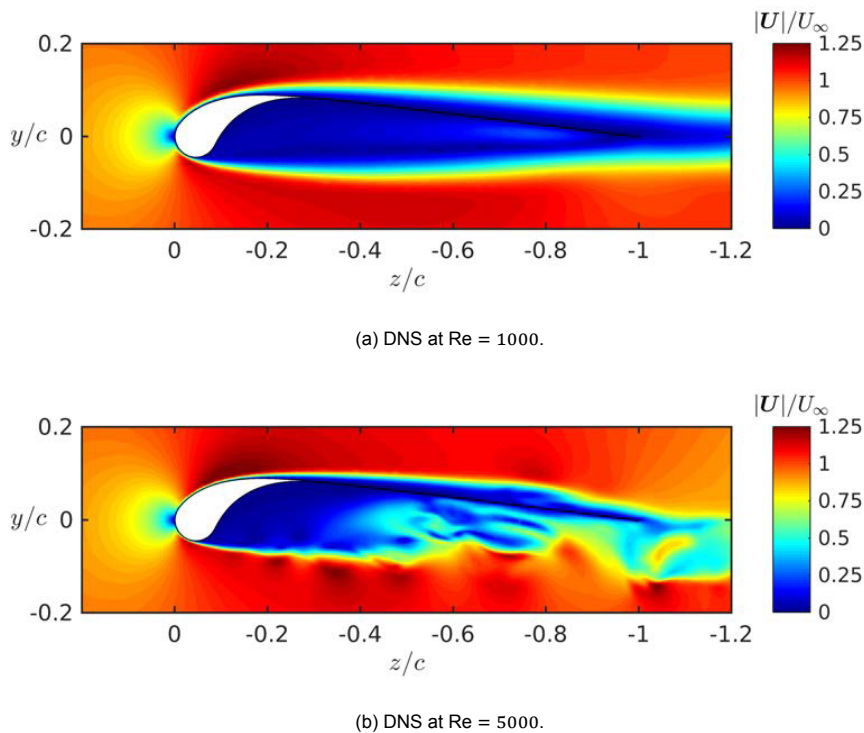


Figure 2.6: 2D normalised velocity field contours of the flow around a 3D LEI kite at zero angle of attack [13].

Gouttière [24] has drawn similar conclusions as Coudou [13] by means of a DNS analysis of the same rigid model at $Re = 5000$ and a zero degree angle of attack. The suction side of the rigid LEI wing is subject to similar flow phenomena as experienced by a conventional airfoil, whilst the pressure side sees the formation of a recirculation zone behind the leading edge tube. At low Reynolds numbers, the mean velocities are highest on the pressure side of the kite, resulting in a negative mean lift coefficient due to the lower pressure below the membrane. This is explained by the fact that flow separation from the laminar boundary layer occurs earlier at lower Reynolds numbers. The separation point moves further downstream for larger Reynolds numbers, which subsequently leads to an upward lift induced by the lower pressure above the membrane.

To summarise, DNS is not a viable option for moderate-to-high Reynolds number flows. For this reason, only the results of simulations have been discussed since DNS studies provide insight into the details of turbulent flow structures. The software implementation and meshing strategies have been omitted and the reader is referred to Coudou [13] and Gouttière [24] for further information.

2.2.2. Large-Eddy Simulation (LES)

Large-scale turbulent structures are inherently more energetic than smaller scaled counterparts. As such, a more efficient transportation of conserved quantities is observed with large-scale turbulent motions. Based on this phenomenon, the LES method resorts to resolving only large-scale turbulent structures and modelling less energetic small-scale turbulent motions. This overcomes a prominent limitation encountered with DNS, which is that the majority of computational resources are directed towards resolving small-scale turbulent structures. Therefore, with regard to both computational cost and flow simulation accuracy, the LES method lies between DNS and the RANS simulation approach given the same flow conditions. [19, 36]

Nevertheless, LES remains a computationally demanding solution for complex geometries immersed in high Reynolds number flows. Therefore, LES is not deemed to be a suitable option given the scope and purposes of this work. At the time of writing, no LES studies of LEI wings could be found.

2.2.3. Reynolds-Averaged Navier-Stokes (RANS) Simulation

The RANS approach is more suitable for simulating higher Reynolds number flows since all turbulent scales are modelled, thus significantly scaling down the computational cost. As neither large nor small scale turbulent structures are resolved, RANS simulations are less accurate than LES or DNS for the same flow conditions. Nevertheless, RANS is the most widely used CFD method for practical flow simulations due to its high computational efficiency.

The main principle of Reynolds averaging is to examine the time-averaged flow rather than the instantaneous time-dependent flow. Variables are decomposed into a mean value and an instantaneous fluctuation (known as Reynolds decomposition), then substituted into the Navier-Stokes equations and time-averaged. The end result of this process leads to the so-called RANS equations. However, there are more unknown variables than equations, implying that the RANS equations are not closed. Therefore, empirical approximations known as turbulence models are required to close the set of equations. [45]

Turbulence Modelling

There are a wide range of available turbulence models that close the RANS equations, but none of them are universally applicable. The suitability of a certain turbulence model strongly depends on the type of flow that is to be simulated. The two most widely used turbulence models are the $k - \epsilon$ and $k - \omega$ models, which belong to the *two-equation* class of turbulence models. As the name suggests, a total of two transport equations are solved, given that an individual transport equation is solved for

each independent turbulence quantity. In the case of the $k - \epsilon$ turbulence model, the two turbulence quantities are the turbulent kinetic energy k and the turbulent dissipation ϵ . The $k - \omega$ model utilises the specific turbulent dissipation ω instead. The two turbulence quantities are then used to derive a length scale, a time scale and the eddy viscosity ν_t . The turbulence models within this class, known as *eddy-viscosity models*, describe the eddy viscosity without having to explicitly prescribe the length scale. [19, 36]

Alternatively, the $k - \omega$ shear-stress transport (SST) model developed by Menter [31] combines the standard $k - \epsilon$ model with the original $k - \omega$ model into a single two-equation eddy-viscosity model. The $k - \omega$ SST model activates either of the two underlying turbulence models based on the distance from the surface immersed in the flow field. It operates such that the $k - \omega$ model is activated for distances within the boundary layer, whereas the $k - \epsilon$ model comes into effect for distances outside of the boundary layer. In the case of modelling the flow over a flexible single-surface membrane airfoil, Smith and Shyy [39] came to the conclusion that the $k - \omega$ SST model is more suitable than the standard $k - \epsilon$ model. The study conducted by Collie et al. [12] presents similar findings with regard to the turbulent flow across an upwind yacht sail. It is apparent that the aerodynamic force coefficients predicted for separated flows at high angles-of-attack by the $k - \epsilon$ model do not stand up to scrutiny. As such, Collie et al. [12] also recommend the $k - \omega$ SST turbulence model as a suitable alternative for modelling separated flows. The studies conducted by Breukels [7], Folkersma et al. [21], Folkersma et al. [22], Demkowicz [16] and Lebesque [29] all made use of the $k - \omega$ SST turbulence model to describe the motion of turbulent flow over soft membrane wings used in AWE applications.

Transition Modelling

An important assumption of the most commonly used turbulence models is that the boundary layer is continuously turbulent, which is the case for the approaches to turbulence modelling previously described. As such, a transition model may be required to accurately predict the transition from laminar to turbulent flow, which strongly depends on the Reynolds number and surface roughness. For certain high Reynolds number flows, a transition model can be omitted since transition occurs almost instantly upon the flow coming into contact with the surface. But when the Reynolds number is not particularly high, transition may occur later over a smooth surface, implying that a portion of the boundary layer is laminar. For such a case, a transition model would be needed to accurately simulate the flow. [21, 43]

The simulations carried out by Demkowicz [16] and Lebesque [29] relied upon the $k - \omega$ SST turbulence model and the $\gamma - \tilde{Re}_{\theta_t}$ transition model (developed by Langtry and Menter [27]) to accurately simulate the steady-state flow over a smooth surfaced 3D LEI wing for a large range of Reynolds numbers. The $\gamma - \tilde{Re}_{\theta_t}$ transition model does not reproduce the actual real-world flow physics that characterises flow transition. Instead, use is made of an experimental database comprised of an array of flow conditions and physical geometries in order to form empirical transition correlations. The transition model encompasses individual transport equations for both the intermittency parameter γ and the transition onset momentum thickness Reynolds number \tilde{Re}_{θ_t} . The intermittency parameter γ represents the probability that a specific point in the flow field is contained within a region undergoing turbulence. As such, the local flow field quantities and the wall distance define its transport equation.

Assuming a perfectly smooth surface, Demkowicz [16] came to the conclusion that $Re = 3 \times 10^6$ is the threshold below which the transition model would need to be implemented, as is evident from Figure 2.7. The lift and drag polars show how stall prediction suffers a drop in accuracy if the transition model is omitted for $Re = 5 \times 10^5$ and $Re = 3 \times 10^6$. But for $Re = 10 \times 10^6$, the transition model has a negligible effect on the stall prediction. Another observation from Figure 2.7 is that the effect of the transition model appears to be minimal for angles of attack below stall, regardless of the Reynolds number.

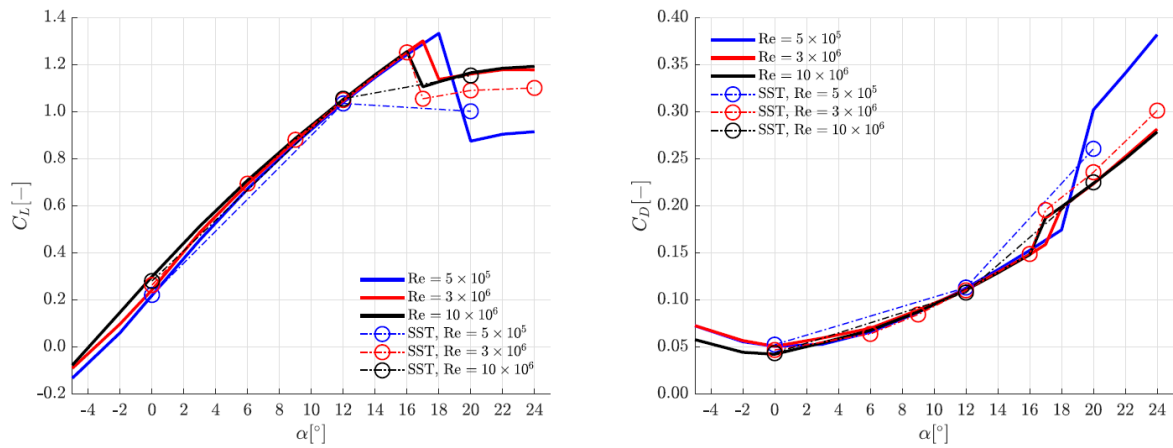


Figure 2.7: LEI wing lift (left plot) and drag (right plot) polars given for different Re numbers. Solid lines are with $\gamma - \widetilde{Re}_{\theta_t}$ transition model, whereas dashed lines are without [16].

Folkersma et al. [21] conducted a steady-state two-dimensional analysis of the flow across a smooth surfaced LEI airfoil with the $k - \omega$ SST turbulence model and the $\gamma - \widetilde{Re}_{\theta_t}$ transition model. Similar to what was concluded by Demkowicz [16], it is apparent that the inclusion of a transition model for low Reynolds number flows (for this case in the range of $Re < 2 \times 10^7$) leads to more accurate results that are closer to the relevant experimental data. Demkowicz [16] confirmed that the three-dimensional polars demonstrate similar trends to the two-dimensional polars acquired by Folkersma et al. [21]. However, the three-dimensional analysis of the LEI wing immersed in a flow field did reveal the presence of a strong spanwise cross-flow effect that is inherently absent within the context of a two-dimensional examination.

The inclusion of a transition model for low Reynolds number simulations of a LEI wing allows for the acquisition of numerical data suitable for comparisons with wind tunnel data acquired from a scaled polished metal wing model [44]. However, considering that an actual LEI kite is comprised of textile material and stitched seams as shown in Figure 2.8, prominent surface roughness and protruding features are expected to perturb the flow and cause an early onset of boundary layer transition [20]. Therefore, transition modelling can be omitted if the stitched seams near the leading edge are assumed to trigger laminar-to-turbulent transition almost instantly upon the flow encountering the leading edge of the wing.

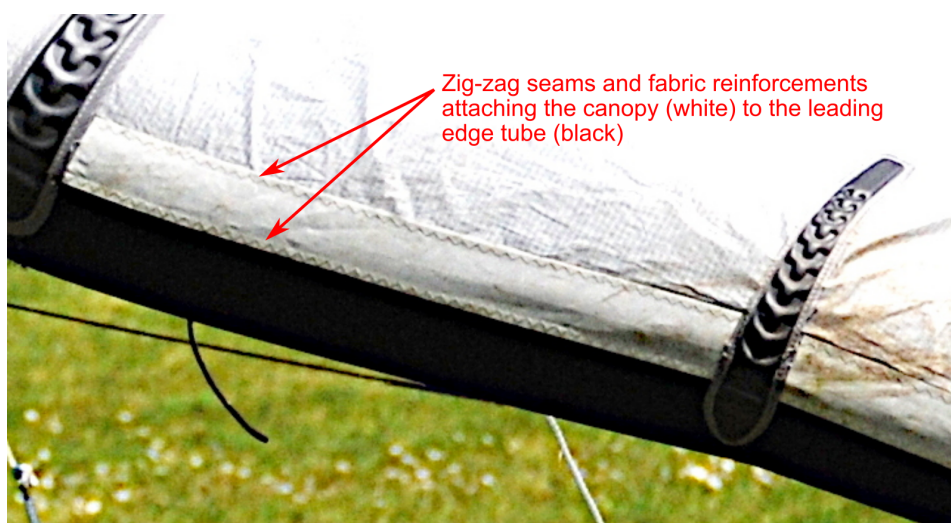


Figure 2.8: Protruding stitched seams near the leading edge of a LEI kite.

2.3. In-Flight Measurements

Assessing in-flight measurements attained from LEI kites operating in an AWE context gives insight into the range of Reynolds numbers observed during flight. The Reynolds number estimations have been based on the apparent wind velocity v_a , which is the vector difference between the wind speed v_w and the velocity of the kite v_k : $\vec{v}_a = \vec{v}_w - \vec{v}_k$

Given the free-stream air density ρ_∞ , free-stream dynamic viscosity μ_∞ and the chord length c as the characteristic length scale, the Reynolds numbers observed during flight tests have been estimated using the following expression:

$$\text{Re} = \frac{\rho_\infty v_a c}{\mu_\infty} \quad (2.13)$$

In the work of Oehler and Schmehl [33], measurements of the apparent wind velocity v_a have been attained from a representative traction phase of a test flight of the V3 LEI kite model, which has a maximum chord length of $c = 2.7$ m. The measurements displayed in Figure 2.9 show that the apparent wind velocity roughly fluctuates between 14 m s^{-1} and 24 m s^{-1} over the time range of the representative traction phase.

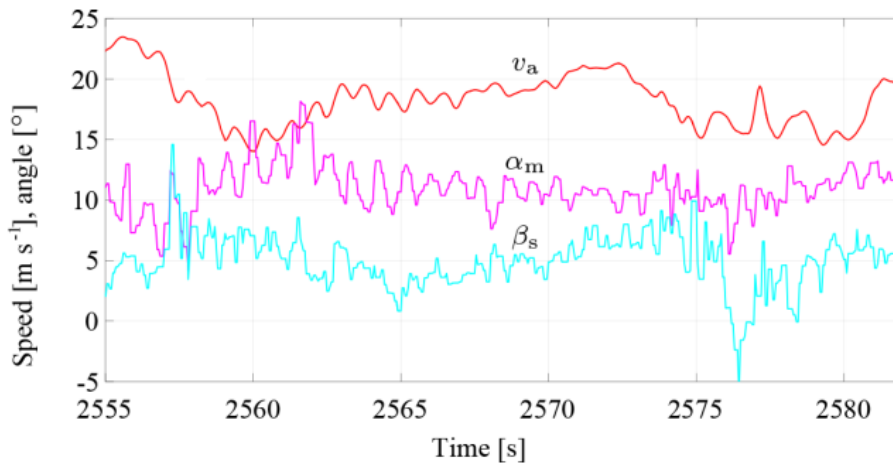


Figure 2.9: In-flight measurements of the apparent wind velocity v_a and inflow angles α_m and β_s over the time range of a representative traction phase of the V3 LEI kite model flying in AWE operations [33].

Assuming standard sea-level conditions (i.e. $\rho_\infty = 1.225 \text{ kg m}^{-3}$ and $\mu_\infty = 1.789 \times 10^{-5} \text{ kg m}^{-1} \text{ s}^{-1}$ [2]) and using the maximum chord length $c = 2.7$ m as the characteristic length scale, the range of observed Reynolds numbers is approximately within the limits of $2.6 \times 10^6 \leq \text{Re} \leq 4.4 \times 10^6$.

A larger range of traction phase Reynolds numbers have been estimated based on the in-flight measurements presented in Figure 2.10, which have been gathered from a flight test of the V2 LEI kite model in Valkenburg around June 2012 [37]. The results presented in Figure 2.10 are over the entire temporal range of the flight test, thus capturing several pumping cycles. During the traction phases (indicated by increasing height over time), the apparent wind velocity approximately varies between 20 m s^{-1} and 40 m s^{-1} .

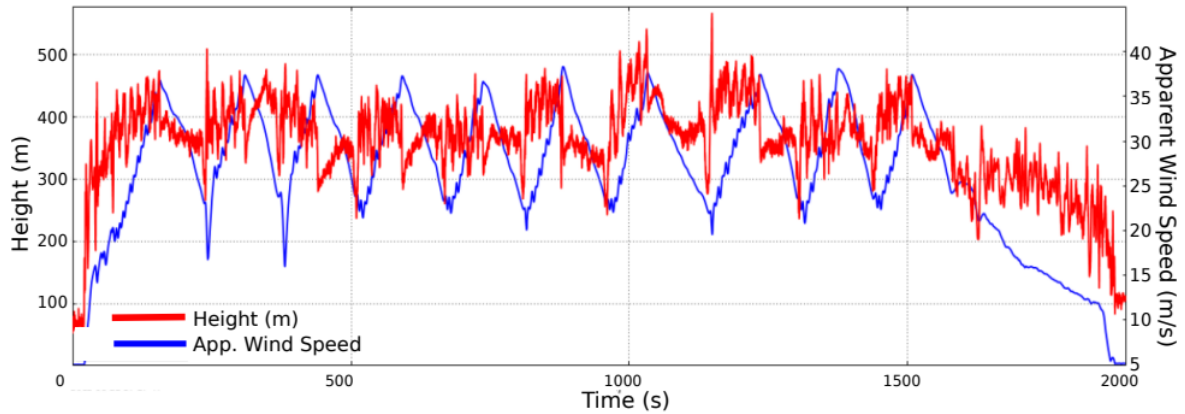


Figure 2.10: In-flight measurements of the apparent wind velocity and height above the ground over the full operation time of the V2 LEI kite model flying AWE manoeuvres [15]. Note that the legend is incorrect: The blue curve displays altitude measurements, whereas apparent wind velocity measurements are given by the red curve.

The V2 LEI kite model has a mid-span chord length of $c = 2.72$ m, which is inherently the largest chord length along the span of the wing. Using $c = 2.72$ m as the characteristic length scale and assuming standard sea-level conditions, given the relatively low altitudes at which the kite is flying, the Reynolds number range representative of the flow field around the kite during the traction phase is roughly within the limits of $3.7 \times 10^6 \leq Re \leq 7.5 \times 10^6$.

It is evident that the traction phase of a LEI kite operating in an AWE context is subjected to a limited range of Reynolds numbers. As such, in the interest of substantially reducing the number of simulations required to develop the revised aerodynamic load model, the Reynolds number can be omitted as an input variable. The implication of this approach is that all numerical simulations conducted for the purpose of building the revised model should be prescribed the same Reynolds number.

2.4. Research Questions

Based on the reviewed literature, a revision of the aerodynamic load model for LEI kites devised by Breukels [7] is warranted. The ambiguity surrounding the airfoil parameterisation and geometric construction in the primary source has led to contradicting interpretations of the model in succeeding studies. Furthermore, inconsistencies abound in the primary source, further sowing doubt in the efficacy of the load model. As such, it is the goal of this study to rectify the problems and limitations described in Section 2.1.3.

Another limitation of the work of Breukels [7] is the omission of the chordwise position of maximum camber as an input variable of the aerodynamic load model. This entails the assumption that a deforming canopy only moves vertically when subjected to an aerodynamic load, when in reality there is also horizontal movement [17, 42]. Therefore, the incorporation of the chordwise position of maximum camber as an additional input variable is expected to produce a more representative aerodynamic load model.

Based on these findings, the research questions of this thesis are:

1. What is the minimum set of two-dimensional shape parameters required to describe the flow around a leading edge inflatable kite airfoil?
 - (a) What is the effect of adding the chordwise position of maximum camber as an input parameter (along with the maximum camber magnitude, tube diameter and angle-of-attack)?
 - (b) To what extent is the revised polynomial regression model an improvement over the original version developed by Breukels [7]?

Another goal of this literature review has been to research suitable CFD methods that would lead to an acceptable balance between solution fidelity and simulation run-time. Based on the reviewed literature and the current state-of-the-art, the RANS simulation approach appears to offer a suitable cost-versus-accuracy trade-off for the purposes of this work. The CFD software package OpenFOAM is deemed to be a versatile tool for numerical data acquisition.

3

Research Method

Following the literature study presented in Chapter 2, a research plan for this thesis has been devised. This chapter delves into the holistic approach towards answering the research questions established in Section 2.4. The flowchart displayed in Figure 3.1 presents a visualisation of the research workflow.

Starting with the method of flow field simulation, a thorough understanding of the underlying theory is warranted in order to justify the utilisation of the applied method and to ensure it is applied accordingly. As such, Chapter 4 presents a description of the underlying theory of CFD and the reasons behind the choices of simulation method and turbulence model.

Prior to simulating the flow field around a lifting body is the establishment of the shape of the lifting body itself. As there is no standardised means of generating a parameterised LEI wing profile suitable for meshing, the parameterisation and geometric construction of LEI wing profiles simulated for the purposes of this work have been explained in Chapter 5.

Having devised a method of parameterisation and geometric construction of LEI wing profiles, one can proceed with generating suitable numerical grids. The approach to mesh generation has been rationalised in Chapter 6.

Following the data acquisition is the visualisation and interpretation of the results in Chapter 7. This serves as a means to gauge the efficacy of the numerical data used to develop the aerodynamic load model presented in Chapter 8. The conclusions of this work and recommendations for further research described in Chapter 9 stem from the findings of the results.

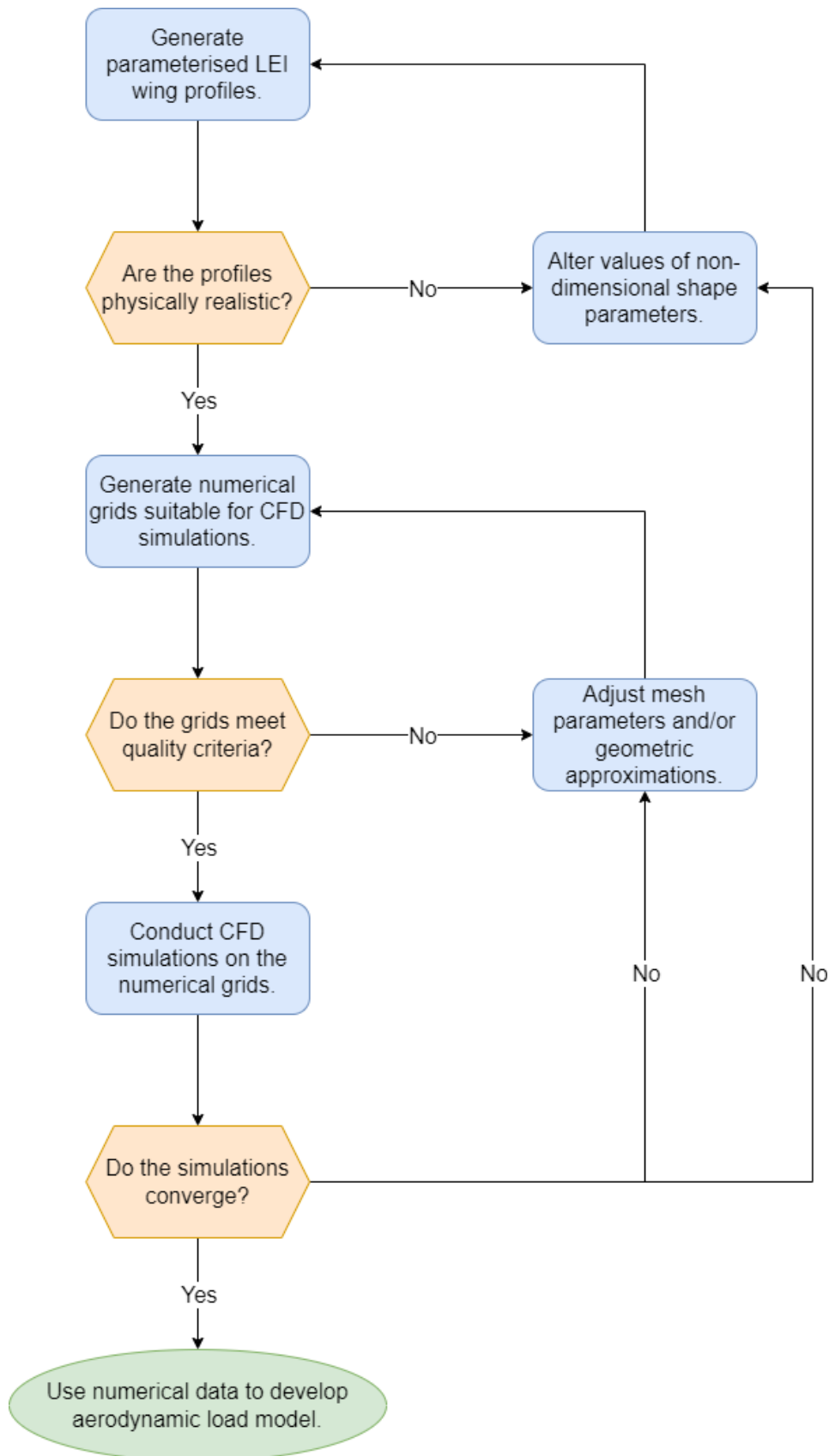
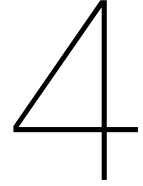


Figure 3.1: Flowchart describing the workflow of this study.



Computational Fluid Dynamics

A crucial demand of this study is the acquisition of numerical data by means of CFD, thus calling for an elucidation of the underlying theory. This chapter starts with the derivation of the RANS equations in Section 4.1, followed by an in-depth description of the applied turbulence model in Section 4.2. Next is a concise explanation of the method used to discretise the equations in Section 4.3. Concluding this chapter are descriptions of the CFD solver and the applied solution algorithm in Section 4.4.

4.1. Reynolds-Averaged Navier-Stokes (RANS) Equations

Judging from the CFD simulation methods reviewed in Section 2.2, the RANS equations grant a suitable balance between simulation accuracy and computational cost given the scope of this work. Based on the work of Folkersma et al. [21], the flow is assumed to be steady-state and incompressible. The latter assumption is justified by the relatively low speeds (and subsequent low Mach numbers) at which a LEI kite operates in an AWE context. The assumption of incompressible flow implies a constant air density ρ . Further assuming a constant dynamic viscosity μ leads to a constant kinematic viscosity $\nu (\equiv \mu/\rho)$.

Regarding steady-state incompressible turbulent flow without body forces, the instantaneous Navier-Stokes equations expressed in Cartesian coordinates and tensor notation are the following:

$$\frac{\partial u_i}{\partial x_i} = 0 \quad (4.1a)$$

$$u_j \frac{\partial u_i}{\partial x_j} = -\frac{1}{\rho} \frac{\partial p}{\partial x_i} + \nu \frac{\partial^2 u_i}{\partial x_j^2} \quad (4.1b)$$

The velocity vector $u_i = (u_1, u_2, u_3) = (u, v, w)$ adopts a coordinate system in which u is the velocity component parallel to the free-stream, v is the velocity component normal to the wall and w is the velocity component lateral to the free-stream. Note that the presence of repeated indices in a single term implies summation: $\frac{\partial u_i}{\partial x_i} = \frac{\partial u}{\partial x} + \frac{\partial v}{\partial y} + \frac{\partial w}{\partial z}$

The instantaneous velocity vector u_i and instantaneous pressure field p are subsequently subjected to Reynolds decomposition:

$$u_i(x_i, t) = \bar{u}_i(x_i) + u'_i(x_i, t) \quad (4.2a)$$

$$p(x_i, t) = \bar{p}(x_i) + p'(x_i, t) \quad (4.2b)$$

The mean velocity vector and mean pressure are denoted by \bar{u}_i and \bar{p} respectively, whereas u'_i denotes the velocity fluctuation vector and p' denotes the pressure fluctuation. A property of Reynolds decomposition is that the time average of a fluctuation is equal to zero: $\overline{u'_i} = 0$, $\overline{p'} = 0$

Substituting the Reynolds decomposed expressions into the instantaneous Navier-Stokes equations and subsequently taking the time averages leads to the RANS equations:

$$\frac{\partial \bar{u}_i}{\partial x_i} = 0 \quad (4.3a)$$

$$\bar{u}_j \frac{\partial \bar{u}_i}{\partial x_j} = -\frac{1}{\rho} \frac{\partial \bar{p}}{\partial x_i} + \nu \frac{\partial^2 \bar{u}_i}{\partial x_j^2} - \frac{\partial \overline{u'_i u'_j}}{\partial x_j} \quad (4.3b)$$

The final step introduces the velocity covariances $\overline{u'_i u'_j}$ representing the fluctuating velocity field effects. Even though the *Reynolds stress tensor* is by definition $-\rho \overline{u'_i u'_j}$ (given the dimension of stress), it is common practice to refer to $\overline{u'_i u'_j}$ as such [36].

The presence of the Reynolds stresses in Equation (4.3b) shows that there are more unknown variables than equations, proving that the RANS equations are not closed. Deriving an equation for the Reynolds stress tensor will simply introduce more unknown variables that need to be modelled. Therefore, the $k - \omega$ SST turbulence model is introduced in order to close the set of equations.

4.2. Turbulence Modelling

Among the empirical approximations reviewed in Section 2.2.3, the $k - \omega$ SST turbulence model emerges as the most fitting solution by which the RANS equations can be closed. Eddy-viscosity models such as the $k - \omega$ SST turbulence model adhere to the assumption that Reynolds stresses are related to the mean velocity gradients via the *eddy viscosity* ν_t (also referred to as *turbulent viscosity*), a hypothesis devised by J. Boussinesq in the year 1877 [36, 45]:

$$\overline{u'_i u'_j} = -\nu_t \left(\frac{\partial \bar{u}_i}{\partial x_j} + \frac{\partial \bar{u}_j}{\partial x_i} \right) + \frac{2}{3} \delta_{ij} k \quad (4.4)$$

Note that Equation (4.4) is a simplified expression based on the assumption of incompressible flow. The δ_{ij} term denotes the Kronecker delta, whereas k is the turbulent kinetic energy:

$$\delta_{ij} = \begin{cases} 1, & \text{if } i = j \\ 0, & \text{if } i \neq j \end{cases} \quad (4.5)$$

$$k = \frac{1}{2} \overline{u'_i u'_i} = \frac{1}{2} \left(\overline{u' u'} + \overline{v' v'} + \overline{w' w'} \right) \quad (4.6)$$

This approach to turbulence modelling is mathematically analogous to the relation between stress and rate-of-strain for Newtonian fluids since the eddy viscosity ν_t is a scalar quantity with the same dimension as the kinematic viscosity ν . However, a key distinction is the fact that the eddy viscosity ν_t is not a fluid property like the kinematic viscosity ν but a field quantity. Substituting Equation (4.4) into the Navier-Stokes equations reduces the number of unknown variables to a single scalar field, namely the eddy viscosity ν_t . What follows is the modelling of this scalar field by means of dimensional analysis. In the case of *two-equation* models, the eddy viscosity is defined in terms of two independent turbulence quantities for which individual transport equations are solved. [19, 36, 45]

The transport equations of the $k - \omega$ SST turbulence model are:

$$\bar{u}_j \frac{\partial k}{\partial x_j} = \tilde{P}_k - \beta^* k \omega + \frac{\partial}{\partial x_j} \left[(v + \sigma_k v_t) \frac{\partial k}{\partial x_j} \right] \quad (4.7a)$$

$$\bar{u}_j \frac{\partial \omega}{\partial x_j} = \frac{\gamma}{v_t} \tilde{P}_k - \beta \omega^2 + \frac{\partial}{\partial x_j} \left[(v + \sigma_\omega v_t) \frac{\partial \omega}{\partial x_j} \right] + 2(1 - F_1) \sigma_{\omega 2} \frac{1}{\omega} \frac{\partial k}{\partial x_j} \frac{\partial \omega}{\partial x_j} \quad (4.7b)$$

Defined as a *blending function*, the F_1 term in Equation (4.7b) permits smooth transitioning between the standard $k - \epsilon$ and original $k - \omega$ models based on the distance from the closest wall y :

$$F_1 = \tanh \left[\left[\min \left[\max \left(\frac{\sqrt{k}}{\beta^* \omega y}, \frac{500\nu}{y^2 \omega} \right), \frac{4\sigma_{\omega 2} k}{CD_{k\omega} y^2} \right] \right]^4 \right] \quad (4.8)$$

The $CD_{k\omega}$ term in Equation (4.8) denotes the positive cross diffusion in Equation (4.7b) and is calculated as follows:

$$CD_{k\omega} = \max \left(2\sigma_{\omega 2} \frac{1}{\omega} \frac{\partial k}{\partial x_j} \frac{\partial \omega}{\partial x_j}, 10^{-10} \right) \quad (4.9)$$

A smooth blend of the two underlying turbulence models is made possible by the fact that F_1 can take any value between zero and one ($0 \leq F_1 \leq 1$). The blending function takes a value of $F_1 = 0$ for distances far away from the closest wall, thus activating the standard $k - \epsilon$ model. Close to the wall, the original $k - \omega$ model is enabled by setting $F_1 = 1$.

Another blending function F_2 , also dependent on the distance from the closest wall y , is introduced for the purpose of calculating the eddy viscosity v_t :

$$v_t = \frac{a_1 k}{\max(a_1 \omega, |S| F_2)} \quad (4.10)$$

$$F_2 = \tanh \left[\left[\max \left(\frac{2\sqrt{k}}{\beta^* \omega y}, \frac{500\nu}{y^2 \omega} \right) \right]^2 \right] \quad (4.11)$$

The application of an eddy viscosity limiter, as defined by Equation (4.10), is what sets the $k - \omega$ SST model apart from the $k - \omega$ BST (*Baseline Stress Transport*) model [31]. The latter solution is defined by the same transport equations, but with different empirical constants and the standard form of the eddy viscosity $v_t = \frac{k}{\omega}$. The purpose of the eddy viscosity limiter in the $k - \omega$ SST model is to prevent over-prediction of the wall shear stress, thus leading to more accurate numerical representations of mildly separated flows.

The final term in the transport equations requiring further elaboration is the limited production term \tilde{P}_k :

$$\tilde{P}_k = \min(P_k, 10\beta^* k \omega) \quad (4.12)$$

$$P_k = v_t \frac{\partial \bar{u}_i}{\partial x_j} \left(\frac{\partial \bar{u}_i}{\partial x_j} + \frac{\partial \bar{u}_j}{\partial x_i} \right) \quad (4.13)$$

The purpose of the production limiter is to regulate turbulence production and prevent amplification in stagnation regions.

The reader should be aware of the fact that the equations reproduced thus far are of the revised $k - \omega$ SST model of Menter et al. [32] (NB the ω transport equation written in the aforementioned paper contains a typographical error that gives an incorrect production term, refer to Equation (4.7b) instead).

The magnitude of the strain rate tensor S replaces the absolute value of the vorticity from the initial formulation of the eddy viscosity limiter proposed by Menter [31]. The second term in Equation (4.9) is 10^{-20} instead of 10^{-10} in the original version of Menter [31]. The production limiter proposed by Menter [30] has been further utilised by Menter [31], whereby the second term in Equation (4.12) is multiplied by a factor of 20 instead of 10.

The choice between different versions of the $k - \omega$ SST model also affects the empirical constants, where blending between the underlying turbulence models is governed by a linear interpolation using the blending function F_1 :

$$\phi = F_1 \phi_1 + (1 - F_1) \phi_2 \quad (4.14)$$

Equation (4.14) defines an arbitrary empirical constant ϕ in terms of ϕ_1 and ϕ_2 , which are the corresponding model constants of the original $k - \omega$ and standard $k - \epsilon$ models respectively.

The empirical constants established by Menter et al. [32] are the following:

Table 4.1: Empirical constants of $k - \omega$ SST model [32]

Set 1: ϕ_1				Set 2: ϕ_2					
β_1	γ_1	σ_{k1}	$\sigma_{\omega 1}$	β_2	γ_2	σ_{k2}	$\sigma_{\omega 2}$	β^*	a_1
3/40	5/9	0.85	0.5	0.0828	0.44	1	0.856	0.09	0.31

This concludes the breakdown of the $k - \omega$ SST turbulence model. The reader should be aware of the assumption of a continuously turbulent boundary layer. Regarding flow cases in which delayed laminar-to-turbulent transition is expected, transition modelling overcomes the inherent assumption of constant turbulent flow. However, in the case of a LEI wing operating in an AWE context, transition to turbulent flow is expected to occur almost instantly due to surface roughness and protruding features near the leading edge. As such, transition modelling has been omitted from this study since the assumption of continuously turbulent flow is not expected to impede the solution accuracy.

This approach strays from the methods of Foldersma et al. [21], Demkowicz [16] and Lebesque [29], each having utilised the $\gamma - \widetilde{Re}_{\theta t}$ transition model together with the $k - \omega$ SST turbulence model. This additional modelling step permits the acquisition of numerical data suitable for comparisons with wind tunnel measurements obtained from a smooth polished metal wing model. The smooth surface of the model causes a delay in laminar-to-turbulent transition, thus spawning a prominent laminar portion of the boundary layer. Such an outcome is not expected for an actual LEI kite flying in AWE operations.

4.3. Discretisation

Applying the Navier-Stokes equations in a CFD context requires a reformulation of the continuous equations by means of an established discretisation method. This entails the approximation of partial differential equations as a system of algebraic equations. The *finite volume method* (FVM) has been used for this purpose.

The finite volume method applies the conservation equations, in integral form, to a finite set of contiguous control volumes that form the discretised solution domain. The values of the flow variables are calculated at a computational node stored at the centroid of each control volume. This is followed by an interpolation of the flow variables, based on the computed centroid values, towards the control volume surfaces. Quadrature formulae approximate the surface and volume integrals. As such, each control volume is defined by an algebraic equation expressed in terms of the flow variable values computed at the neighbouring nodes. [19]

The finite volume method is suitable for discretising the flow field around complex geometries due to its applicability to any type of grid. A grid is generated such that the computational nodes are assigned to the control volume centres. Control volume boundaries are defined by the grid such that it does not

have to be related to a coordinate system. Control volumes with a shared boundary have the same surface integrals, implying that the finite volume method is inherently conservative. This means that the flux entering a control volume is equal to the flux exiting the neighbouring one. [19]

4.4. CFD Solver

The CFD solver used in this study, namely OpenFOAM, is concisely summarised in Section 4.4.1. A description of the employed discrete solution algorithm is subsequently provided in Section 4.4.2.

4.4.1. OpenFOAM

The aerodynamic simulation of the various airfoil configurations has been realised with OpenFOAM v2006, a free and open source C++ based CFD toolbox that allows for the development of custom numerical solvers [11]. The turbulent motion of fluids can be simulated using standard libraries and solvers that incorporate the turbulence and transition models described in Section 2.2.3. The discretisation of the Navier-Stokes equations is based on the finite volume method explained in Section 4.3. Although OpenFOAM allows for the simulation of compressibility effects, the low free-stream Mach number of the flow over a LEI wing permits the assumption of incompressibility, thus simplifying the RANS equations (see Equation (4.3)). Assuming steady-state flow, the simpleFOAM solver can be used to simulate the incompressible flow over a flexible membrane wing, as demonstrated by Folkersma et al. [22] and Folkersma et al. [21]. The latter study also notes that OpenFOAM only functions on a three-dimensional domain, which is accounted for in two-dimensional flow simulations by extruding the domain by one cell length in the out-of-plane spanwise direction. The simpleFoam solver utilises the *Semi-Implicit Method for Pressure-Linked Equations* (SIMPLE) algorithm to solve the Navier-Stokes equations.

4.4.2. SIMPLE Algorithm

A pressure-velocity coupling algorithm first developed by Patankar and Spalding [35], the SIMPLE algorithm derives an equation for the kinematic pressure $P = p/\rho$ based on the continuity and momentum equations (Equation (4.1a) and Equation (4.1b) respectively).

The algorithm starts by expressing the discrete algebraic momentum equations in matrix form:

$$\mathcal{M}\vec{u} = -\nabla P \quad (4.15)$$

Matrix \mathcal{M} comprises the coefficients that arise from the finite volume discretisation of the terms in the momentum equations.

To further elaborate, the matrix form of the algebraic momentum equation in the x -direction (with velocity component u) is given:

$$\begin{bmatrix} M_{1,1} & M_{1,2} & M_{1,3} & \dots & M_{1,m} \\ M_{2,1} & M_{2,2} & M_{2,3} & \dots & M_{2,m} \\ M_{3,1} & M_{3,2} & M_{3,3} & \dots & M_{3,m} \\ \vdots & \vdots & \vdots & \ddots & \vdots \\ M_{m,1} & M_{m,2} & M_{m,3} & \dots & M_{m,m} \end{bmatrix} \begin{bmatrix} u_1 \\ u_2 \\ u_3 \\ \vdots \\ u_m \end{bmatrix} = - \begin{bmatrix} (\partial P / \partial x)_1 \\ (\partial P / \partial x)_2 \\ (\partial P / \partial x)_3 \\ \vdots \\ (\partial P / \partial x)_m \end{bmatrix}$$

The above matrix expression presents an equation for the centroid of each control volume in the discretised domain. As such, the matrix size m is equivalent to the number of cells in the mesh domain.

A decomposition of the coefficient matrix \mathcal{M} is subsequently executed such that diagonal and off-

diagonal components are separated into matrix \mathcal{A} and matrix $\mathcal{H} = \mathcal{H}(\vec{u})$ respectively:

$$\mathcal{M}\vec{u} = \mathcal{A}\vec{u} - \mathcal{H} \quad (4.16)$$

Then the algebraic momentum equations are expressed in decomposed form:

$$\mathcal{A}\vec{u} - \mathcal{H} = -\nabla P \quad (4.17)$$

An expression for \vec{u} can be derived by rearranging Equation (4.17):

$$\vec{u} = \mathcal{A}^{-1}\mathcal{H} - \mathcal{A}^{-1}\nabla P \quad (4.18)$$

Equation (4.18), referred to as the velocity correction equation, is then substituted into the continuity equation:

$$\nabla \cdot [\mathcal{A}^{-1}\mathcal{H} - \mathcal{A}^{-1}\nabla P] = 0 \quad (4.19)$$

Rearranging Equation (4.19) leads to an equation for the kinematic pressure:

$$\nabla \cdot \mathcal{A}^{-1}\nabla P = \nabla \cdot \mathcal{A}^{-1}\mathcal{H} \quad (4.20)$$

The above equations are employed by the SIMPLE algorithm in the following process:

1. Progress to time step t_{n+1} . Either use the boundary conditions or the converged solutions from the preceding time step t_n to initialise \vec{u}^{n+1} and P^{n+1} .
2. Update \vec{u}^{n+1} and P^{n+1} with the latest predictions of \vec{u} and P respectively.
3. Assemble the algebraic momentum equations in matrix form:

$$\mathcal{M}\vec{u} = -\nabla P$$

Apply implicit under-relaxation and then solve the momentum equations, thus acquiring a new prediction for \vec{u}^{n+1} .

4. Assemble the algebraic equation for the pressure:

$$\nabla \cdot \mathcal{A}^{-1}\nabla P = \nabla \cdot \mathcal{A}^{-1}\mathcal{H}$$

Solve the pressure equation, thus acquiring a new prediction for P^{n+1} .

5. Apply the flux correction equation to ϕ^{n+1} :

$$\phi = \vec{u}_f \cdot \vec{S}_f = [\mathcal{A}^{-1}\mathcal{H} - \mathcal{A}^{-1}\nabla P]_f \cdot \vec{S}_f$$

The cell face velocity vector \vec{u}_f is acquired by interpolating Equation (4.18) towards the control volume edges. The outward pointing vector \vec{S}_f comprises the cell face areas.

6. Apply explicit under-relaxation to P^{n+1} .
7. Apply the velocity correction equation to \vec{u}^{n+1} :

$$\vec{u} = \mathcal{A}^{-1}\mathcal{H} - \mathcal{A}^{-1}\nabla P$$

8. Return to *step 2* if the solutions are not yet converged. What constitutes solution convergence is when both the momentum and continuity equations are satisfied by the velocity field. If this is the case, advance to the next time step.

As documented by Patankar [34], the SIMPLE algorithm has been subject to adaptations over time. One such adaptation is the *Semi-Implicit Method for Pressure-Linked Equations-Consistent* (SIMPLEC) algorithm developed by van Doormaal and Raithby [41], which has been used to simulate steady-state flow fields throughout this study.

The SIMPLEC algorithm omits the under-relaxation of the pressure field since the computational cost is approximately equivalent to using the optimal pressure under-relaxation factor in the SIMPLE algorithm. Using the SIMPLEC algorithm eliminates the need to optimise the under-relaxation factor for the pressure field, which is case dependent and not known *a priori*.

For further elaboration of the SIMPLEC algorithm, the reader is referred to van Doormaal and Raithby [41].

5

Airfoil Geometry

The parameterisation and subsequent geometric construction of a LEI wing profile is a key aspect of this study, thus necessitating an individual chapter demonstrating the applied methodology. The geometric components and constraints used to construct a complete LEI wing profile suitable for meshing have been described in Section 5.1. This is followed by a summary of the spline interpolation system used to generate the relevant geometric components in Section 5.2.

5.1. Geometric Components, Constraints & Parameters

A prominent approximation of the aerodynamic load model developed by Breukels [7] is the assumption that the deforming canopy of a LEI wing is not subjected to variations in chordwise position of maximum camber and only experiences changes in camber magnitude [8]. However, a deforming canopy is expected to undergo changes in both magnitude and chordwise position of camber [42]. The experimental study of a sailwing airfoil conducted by den Boer [17] concludes that with increasing angle-of-attack, the maximum camber of a deforming flexible membrane airfoil shifts towards the leading edge. As such, both van Kappel [42] and Cayon [10] have proposed incorporating the chordwise position of maximum camber as an additional airfoil shape parameter in the polynomial regression model of Breukels [7]. This entails the development of a revised aerodynamic load model that permits user control over the chordwise position of maximum camber along with the original airfoil shape parameters defined in Section 2.1.3.

Therefore, the defining non-dimensional parameters are the maximum camber κ , the relative thickness t and the chordwise position of maximum camber η . As displayed in Figure 5.1, the fundamental geometrical constraints comprise of a point constraint at the trailing edge $(x/c, y/c) = (1, 0)$, a zero-gradient constraint at the point of maximum camber $(x/c, y/c) = (\eta, \kappa)$, a tangent continuity constraint at the point of intersection between the canopy and tube profiles and finally a point constraint for the centre of the circular tube profile at $(x/c, y/c) = (t/2, 0)$. The leading-edge tube profile is represented by a circle of non-dimensional radius $t/2$ with its centre located at $(x/c, y/c) = (t/2, 0)$ such that the point furthest to the left (the leading edge) is positioned at about $(x/c, y/c) = (0, 0)$. The membrane canopy profile has been split into forward and rearward components, both represented by cubic Bézier curves. This approach allows full control over both the magnitude of the maximum camber κ and its chordwise location η , as opposed to a single curve representing the entire canopy profile that would only allow control over one of these parameters. Tangential continuity at the point of maximum camber is inherent.

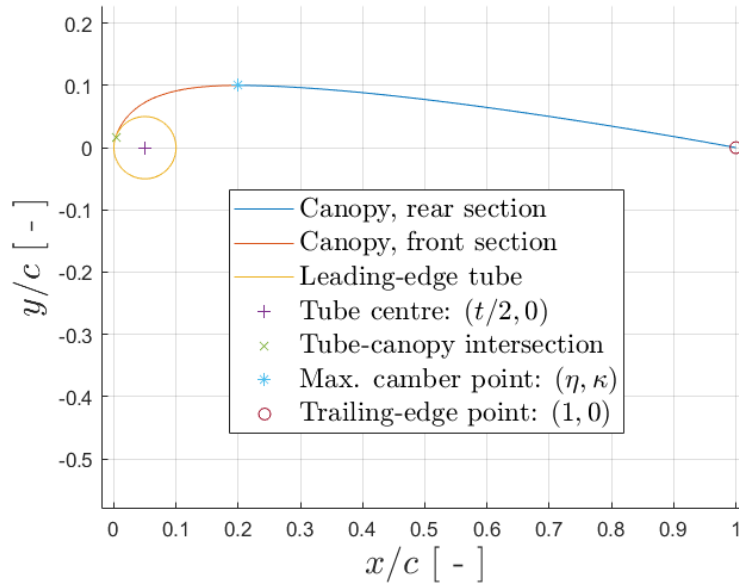


Figure 5.1: Geometric components and constraints of a LEI kite airfoil ($t = 0.1$, $\kappa = 0.1$, $\eta = 0.2$).

The profile displayed in Figure 5.1 only serves as a visualisation of the geometric components and constraints used to construct a LEI wing airfoil. But it is not suitable for mesh generation based on the guidelines summarised in Section 6.1.1. Mesh quality rapidly deteriorates towards sharp corners and edges such as the area near the point of intersection between the tube and canopy profiles. Therefore, a similar smoothing feature as demonstrated in Figure 6.1 has been implemented in order to alleviate the subsequent decline in mesh quality, thus leading to the profile displayed in Figure 5.2. The applied geometric smoothing component is referred to as an ‘edge fillet’, defined by a cubic Bézier curve with its ends tangent to the pressure side of the canopy and the LE tube at the points of intersection. This smoothing component is implemented purely for the purpose of mitigating the limitations of contemporary meshing practices. This leads to a trade-off between accurate representation of geometry and mitigation of meshing constraints. A more sunken edge fillet leads to a more representative airfoil but a less smooth mesh, whereas a more prominent edge fillet allows for better mesh quality but strays further away from reality.

An outcome of the edge fillet approximation is the introduction of a non-dimensional finite canopy thickness t_{canopy} relative to the chord length c . Despite the fact that the membrane canopy has a negligible thickness, contemporary meshing practices necessitate an amplified effective canopy thickness, leading to a similar trade-off as observed with the edge fillet approximation. A larger value of t_{canopy} is less representative of the actual membrane canopy thickness but grants better mesh quality, whereas a smaller value is more accurate but leads to a deterioration in mesh quality. The value of t_{canopy} used to generate the airfoil displayed in Figure 5.2 is an exaggerated quantity in order to emphasise the semi-circular profile of the trailing edge (with diameter t_{canopy}). The rearward canopy section on the pressure side is characterised by a cubic Bézier curve based on the suction side equivalent such that the ends of the semi-circular trailing-edge profile are tangentially continuous at the points of intersection with the rearward canopy curves. Similar to the suction side of the canopy, a zero-gradient constraint is imposed at the point of intersection between the rearward and forward components of the pressure side $(x/c, y/c) = (\eta, \kappa - t_{canopy})$, which also implies tangential continuity.

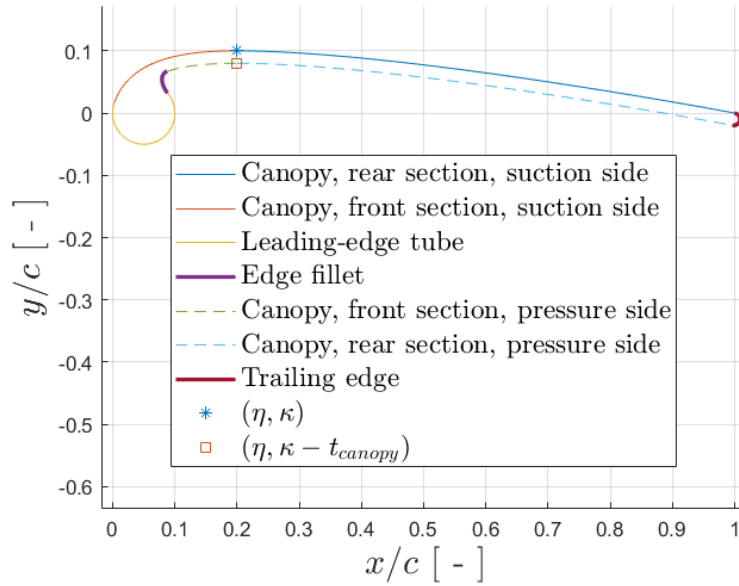


Figure 5.2: Geometric components of a LEI kite airfoil suitable for meshing ($t = 0.1$, $\kappa = 0.1$, $\eta = 0.2$, $t_{canopy} = 0.02$).

In order to enforce tangential continuity at the tube-canopy and edge-tube intersections, the gradients at these points are established by first constructing the circular profile of the LE tube. The locations of the intersection points are governed by the angles displayed in Figure 5.3, where $\theta_{suction}$ controls the tube-canopy intersection point and θ_{edge} provides the edge-tube intersection point. The former angle affects how much of the circular tube profile is present on the suction side near the leading edge, whereas the latter angle dictates the prominence of the edge fillet. Note that the value of θ_{edge} used to construct the profile displayed in Figure 5.2 was purposely chosen to emphasise the edge fillet.

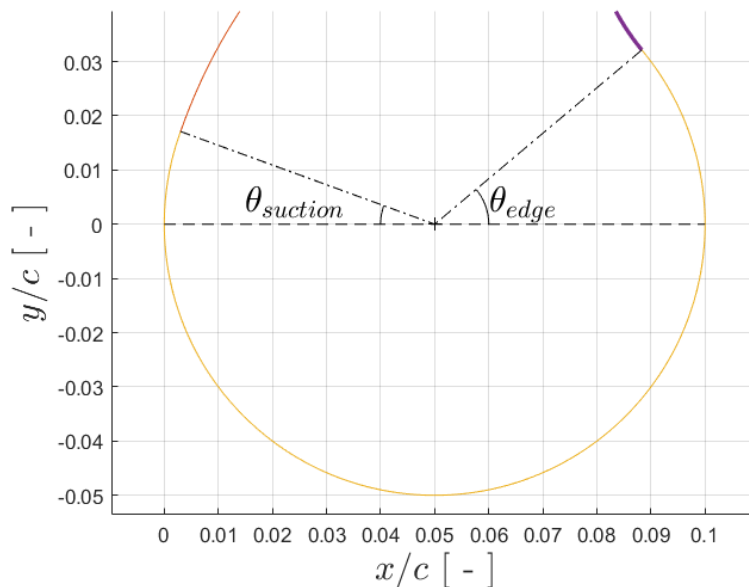


Figure 5.3: Angles $\theta_{suction}$ ($= 20^\circ$) and θ_{edge} ($= 40^\circ$) control the ends of the circular LE tube profile (close-up of Figure 5.2).

The methods used to construct each geometric component displayed in Figure 5.2 foster a holistic tangential continuity of the complete LEI wing profile, the benefits of which are observed when generating

the mesh. The outcome is an inherently smoother numerical grid due to the absence of sharp corners and sudden discontinuities in the geometry. Also worth mentioning is the fact that the point furthest to the right is not precisely located at $(x/c, y/c) = (1, 0)$. However, this is considered to be a minute discrepancy expected to have negligible effects on the aerodynamic simulations, especially for lower values of t_{canopy} .

The values of t_{canopy} and θ_{edge} used to construct the parameterised profile displayed in Figure 5.2 are different from the values used to construct profiles that have been meshed and subsequently simulated for the purposes of this study. The reader should be conscious of the fact that Figure 5.2 serves as a visual guide and is not fully representative of the profiles that have actually been meshed and simulated. The values of the geometric parameters t_{canopy} , $\theta_{suction}$ and θ_{edge} presented in Table 5.1 have been kept constant for every simulated profile.

Table 5.1: Values of fixed geometric parameters used to construct LEI wing profiles for meshing and simulation.

Parameter	Value
t_{canopy}	0.001
$\theta_{suction}$	20°
θ_{edge}	60°

Aside from the leading-edge tube and trailing edge profiles, each curve has been generated by means of a cubic Bézier interpolation scheme further elaborated in the following section.

5.2. Spline Interpolation

As described in Section 2.1.3, there is no standard method for constructing the shape of a LEI wing profile. The means by which Breukels [7] assembled parameterised LEI wing profiles suitable for meshing are unknown, thus necessitating the development of a method that is independent of the primary source. In this study, parameterised LEI wing profiles have been constructed using the spline interpolation system devised by Hobby [25] since it is capable of producing smooth and aesthetically pleasing curves with minimal spline intersection points. It is also possible to impose a gradient at any spline intersection point by assigning a unit vector, which is a necessary feature in order to enforce the geometric constraints described in the preceding section. It should be noted that, in general terms, such an interpolating spline comprises multiple polynomial curves. In the case of open curve problems, where the spline end-points are not connected by a curve, the interpolation system of Hobby [25] generates interpolating splines comprised of $n - 1$ cubic Bézier curves given n spline intersection points. Each cubic Bézier curve comprises 100 discrete points.

Furthermore, a defining geometric characteristic of a LEI wing airfoil that has been replicated using the employed spline interpolation system is the concavity of the membrane canopy profile. This demands an interpolating spline representing the suction side of the canopy that is as close as possible to a concave-downward curve between both ends. The application of so-called “tension” parameters to the relevant spline intersection point(s) permits such a geometric characteristic for cases with minimal spline points. These scalar quantities control the curvature of the spline as it approaches the point(s) of application. An “exit” and “entry” tension parameter can be individually assigned to any spline intersection point, both having a default value of one. The “exit” tension parameter controls the outgoing curve towards the succeeding spline point, whereas the “entry” tension parameter controls the incoming curve from the preceding spline point. As a tension parameter approaches infinity, the part of the curve nearest to the point of application tends to the straight line segment between the two spline points. This is a desired effect towards the trailing edge as there is no explicit gradient constraint at $(x/c, y/c) = (1, 0)$. Therefore, the exit tension of the spline point at $(x/c, y/c) = (1, 0)$ has been prescribed an arbitrarily large value of 1000. Geometric differences between the default and prescribed values are evident in Figure 5.4, where Figure 5.4a shows a discernible point of inflection towards the trailing edge. Increasing the value of the exit tension beyond 1000 has little added effect on the shape

of the spline.

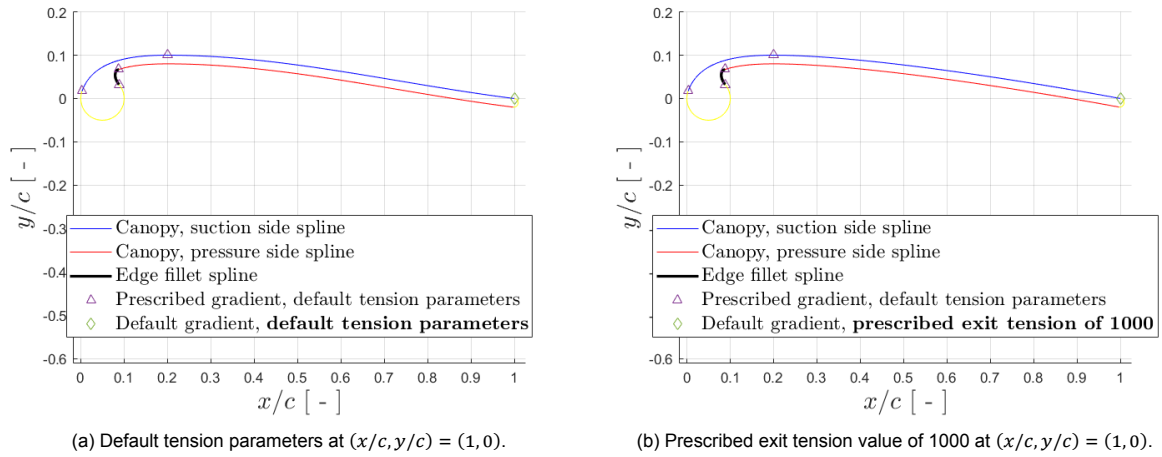


Figure 5.4: Comparison of LEI wing profiles with different tension parameters at spline point $(x/c, y/c) = (1, 0)$ given $t = 0.1$, $\kappa = 0.1$, $\eta = 0.2$, $\theta_{suction} = 20^\circ$, $\theta_{edge} = 40^\circ$ and $t_{canopy} = 0.02$.

The spline representing the pressure side of the membrane canopy is merely a copy of the suction side such that the aforementioned geometric characteristics are emulated. The discrete points of the pressure side spline are each separated by an orthogonal distance equal to t_{canopy} below the equivalent discrete point of the suction side spline. This ensures the membrane canopy has a constant amplified thickness t_{canopy} from the right end-point of the pressure side spline until the point of intersection between the edge fillet and the pressure side spline. This point of intersection is the discrete point of the pressure side spline closest to horizontal alignment (i.e. equal values of x/c) with the lower end of the edge fillet. The remainder of the pressure side spline to the left of this point of intersection is subsequently removed since it occupies the area enclosed by the edge fillet and the leading-edge tube.

The reader is referred to Hobby [25] for detailed insight into the applied spline interpolation system.

6

Mesh Generation & Simulation Set-Up

The process of generating good quality numerical grids is an important consideration for any CFD analysis, as well as the set-up of the analysis itself. Therefore, a description of the mesh generation methodology applied in this study has been presented in Section 6.1, which is followed by an explanation of the employed CFD simulation set-up in Section 6.2.

6.1. Mesh Generation

The generation of a high-quality mesh suitable for CFD simulations is a laborious undertaking that demands thorough attention to detail, a process which is further complicated by the unconventional shape of a LEI wing profile. As such, the following section describes the mesh generation process. The commercial software Pointwise has been used for this purpose, controlled by means of a set of MATLAB functions developed by Buendía [9] (which have been adapted for the demands of this work).

6.1.1. Geometric Approximations

Within the scope of contemporary mesh generation practices, the non-conventional design shape of a LEI wing complicates the process of volume mesh generation if the goal is to develop a high-quality mesh. The combination of the anhedral shape, the thin membrane canopy and the circular profile of the leading edge tube calls for a non-trivial approach when it comes to generating the volume mesh of a three-dimensional wing [43]. Constructing the two-dimensional mesh of a wing profile also requires careful consideration as the merging of the thin membrane canopy and circular profile of the leading edge tube still presents a unique set of challenges.

The first point of contention is the sharp angle between the leading edge tube and the membrane canopy at the intersection of the two respective components. Mesh quality deteriorates rapidly towards sharp corners, hence why it is common practice with regard to both two-dimensional and three-dimensional meshing to smooth the area behind the leading edge tube as depicted in Figure 6.1. Although a smooth filling between the canopy and the leading edge tube does not feature in the actual design shape of the kite, this approximation can be justified due to its negligible effect on the simulated flow field [15, 43].

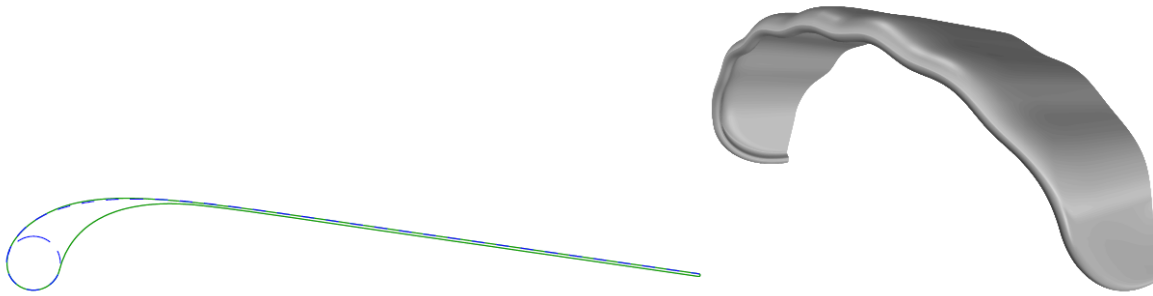


Figure 6.1: LEI wing profile at the mid-section (left image) and 3D CAD model (right image) with smoothed features. The dashed line indicates the original design profile, whereas the solid line indicates the approximated filled profile [43].

The filling behind the leading edge tube introduces a new surface on the pressure side of the airfoil, leading to a membrane canopy with a finite thickness as displayed on the left image of Figure 6.1. Merging the suction side and pressure side surfaces such that the membrane canopy becomes an infinitely thin surface (as the design shape indicates) complicates volume mesh generation due to the implicit blending of two wall boundaries. As such, it is common practice to amplify the thickness of the membrane canopy for the sake of alleviating the need to merge boundaries. Also worth noting is the semi-circular trailing edge of the filled profile displayed in the left image of Figure 6.1. This feature prevents the formation of sharp edges, which have a detrimental effect on mesh quality.

Every geometric approximation described thus far has been applied to each profile simulated for the purposes of this work (see Figure 6.2c and Figure 6.2d).

6.1.2. Mesh Characteristics & Parameters

One can proceed with constructing suitable numerical grids knowing the general shape of a LEI wing profile and having established the required geometric approximations.

Mesh Type & Topology

Numerical grids applied in a CFD context are typically distinguished as *structured*, *unstructured* or *hybrid*, the last form being a combination of the two preceding grid types. Structured grids are characterised by a relatively low cell count (compared to unstructured or hybrid equivalents), thus leading to faster computations. However, more user input is required to generate a high quality mesh, whilst unstructured and hybrid grids benefit from a high degree of automation. Hybrid grids are typically constructed such that the near-wall region is contained within a cluster of structured cells in order to more accurately simulate the high velocity gradients within the boundary layer. A cluster of unstructured cells forms further away from the wall. [20]

Given the large range of airfoil geometries under scrutiny, low computational cost and a highly automated mesh generation procedure are both highly sought after qualities. In order to strike a delicate balance, careful consideration has been given to selecting an appropriate mesh type. A structured O-grid topology, as used in the work of Folkersma et al. [21] and Deaves [15], was deemed to be the most suitable option. The commercial software Pointwise permits the formation of grids with an O-grid topology by means of a hyperbolic extrusion algorithm in the wall normal direction. Given enough mesh layers, the far-field boundary forms into a circular shape as displayed in Figure 6.2b. The extrusion algorithm removes the need to pre-define the boundary of the mesh domain as this is formed automatically in the mesh generation process. As displayed in Figure 6.2, grids generated by means of the hyperbolic extrusion algorithm in the wall normal direction are fully structured, thus benefiting from a relatively low cell count.

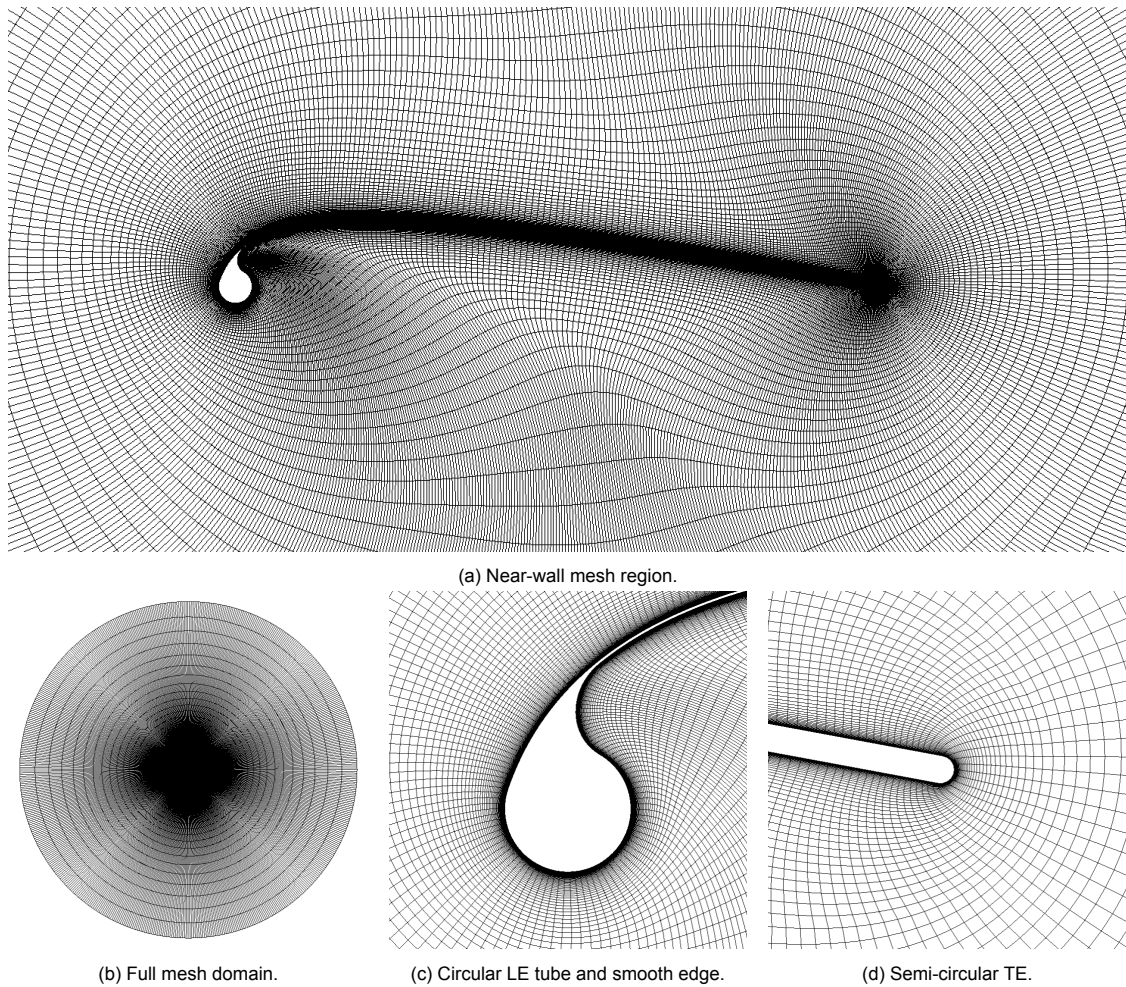


Figure 6.2: Regions of structured mesh with O-grid topology of a LEI wing profile with shape parameters $t = 0.05$, $\kappa = 0.1$ and $\eta = 0.2$ (grid resolution of 576×201).

Grid Point Distribution

The unconventional shape of a LEI wing profile complicates the process of distributing the grid points along the wall boundary. Unlike conventional wing profiles such as the NACA airfoil series, there is no established means of discretising the surface of a LEI wing profile.

Images of LEI wing profile grids, with structured O-grid topologies, have been presented in the work of Folkersma et al. [21] and Deaves [15]. However, both studies do not explicitly describe the means by which the grid points have been distributed. As such, a method for distributing the nodes along the surface of a LEI wing profile grid has been developed such that the qualitative aspects of the reference grids are recreated.

The applied method is evident in Figure 6.3, where the total number of wall nodes (in this case 576) is a prescribed mesh parameter. In order to maintain the circular profiles of the trailing edge and the leading edge tube, the grid points are equally spaced. The number of equidistant nodes along the trailing edge section displayed in Figure 6.3c has been kept constant at 10 throughout this study. In contrast, the number of equally spaced nodes along the surface of the leading edge section displayed in Figure 6.3b is dependent on the curvature of the profile. The same dependency applies to the number of nodes along the canopy section displayed in Figure 6.3a, governed by means of a hyperbolic tangent (\tanh) distribution in order to ensure smooth transitions between the equally spaced sections at both ends. Note that the suction and pressure sides of the canopy section have the same number of grid points.

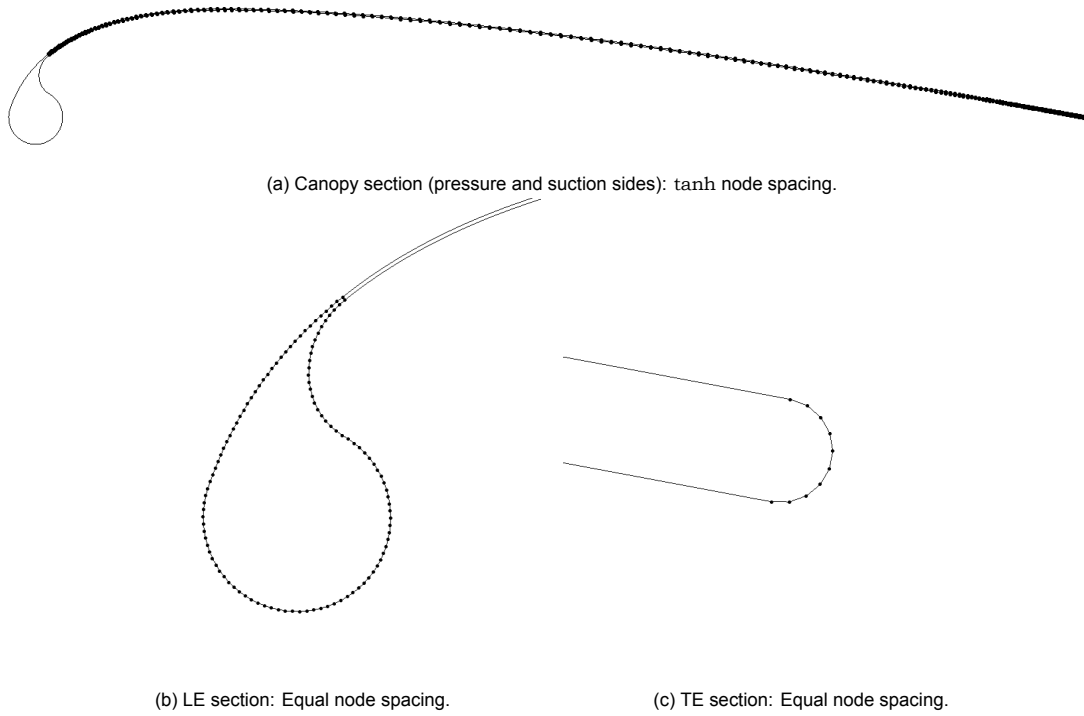


Figure 6.3: Grid point distribution along the surface of a LE1 wing profile with shape parameters $t = 0.05$, $\kappa = 0.1$ and $\eta = 0.2$ (grid resolution of 576×201).

The equations used to calculate the number of nodes n in the variable node sections are the following (given $n_{\text{total}} = 575$ and $n_{\text{TE}} = 10$):

$$n_{\text{LE}} = p \cdot n_{\text{total}} \quad (6.1a)$$

$$n_{\text{canopy}} = \frac{1}{2} (n_{\text{total}} - n_{\text{TE}} - n_{\text{LE}} + 3) \quad (6.1b)$$

The dependency on profile curvature is evident in Equation (6.1a) since the chordwise position of maximum camber η controls the number of nodes in the leading edge section, thus removing the need to individually mesh each profile under consideration. What follows is the calculation of the number of nodes along the pressure and suction sides of the canopy section by means of Equation (6.1b). The calculated values are subsequently rounded to the nearest integer. It should be clarified that the node distribution along the mesh wall boundary is not equivalent to the geometric discretisation of the simulated profile as this is governed by the methodology described in Chapter 5.

Mesh Layer Spacing

The spacing of the grid in the wall-normal direction is controlled by means of a geometric progression method. The cells grow in size in the marching direction at a constant growth rate prescribed by the user, typically between 1.1 and 1.2 [16]. A geometric growth rate of 1.1 was deemed to be suitable and has been used for each grid generated within the scope of this study.

Also required as a prescribed quantity is the height of the wall-adjacent mesh layer y . The value of this mesh parameter is calculated by means of the dimensionless metric of the distance normal to the wall y^+ , governed by the friction velocity $u_\tau = \sqrt{\tau_w / \rho_\infty}$ and the free-stream fluid properties ρ_∞ and μ_∞ (or $\nu_\infty = \mu_\infty / \rho_\infty$):

$$y^+ = \frac{\rho_\infty y u_\tau}{\mu_\infty} = \frac{\rho_\infty y \sqrt{\tau_w / \rho_\infty}}{\mu_\infty} \quad (6.2)$$

The wall coordinate y^+ scales with the boundary layer thickness, which in turn is dependent on the flow conditions. The reason behind the choice of the velocity scale u_τ is the fact that the velocity at the wall is zero due to the no-slip boundary condition and the free-stream velocity U_∞ is of no consequence to the universal shape of the boundary layer that develops close to the wall.

Regarding external aerodynamics cases which exhibit strong curvature, pressure gradient and separation effects, common convention dictates that a wall-resolved boundary layer meets the condition $y^+ < 1$.

What follows is the estimation of the wall shear stress τ_w , defined by Equation (6.3), through an empirical avenue as this quantity is not known *a priori*.

$$\tau_w = \frac{1}{2} c_f \rho_\infty U_\infty^2 \quad (6.3)$$

The empirical relation in question is attributed to turbulent flat-plate boundary layer theory and dictates the value of the local skin friction coefficient c_f . Namely, Prandtl's one-seventh power-law for turbulent flat-plate boundary layers [46]:

$$c_f = \frac{0.027}{\text{Re}_x^{1/7}} \quad (6.4)$$

The chord based Reynolds number has been used to estimate c_f :

$$\text{Re} = \frac{\rho_\infty U_\infty c}{\mu_\infty} = \frac{U_\infty c}{\nu_\infty} \quad (6.5)$$

Assuming $\rho_\infty = 1 \text{ kg m}^{-3}$, $U_\infty = 1 \text{ m s}^{-1}$ and $c = 1 \text{ m}$, the value of the Reynolds number is controlled by altering μ_∞ . The justification for this approach, rather than using representative free-stream quantities, is that the non-dimensional aerodynamic coefficients are of prime interest.

Worth repeating is the fact that the value of the initial cell height y calculated through this approach is an estimate. In practice, y^+ varies over the airfoil surface due to the wall shear stress distribution. But instead of computing the distribution of y^+ , the surface distribution of the turbulent kinetic energy based wall-normal distance y^* , defined by Equation (6.12), has been calculated over the course of each simulation conducted within the scope of this study. Launder and Spalding [28] proposed y^* as an alternative to y^+ as a manner of circumventing singularities due to stagnation and separation points where $\tau_w \approx 0$. Nevertheless, y^* and y^+ generally are equivalent quantities whereby the condition of $y^* < 1$ must be met across the entire surface of the airfoil for a wall-resolved boundary layer. It is not known in advance if the $y^* < 1$ condition is met until the results of a simulation have been processed. If the maximum value of y^* is too large and violates the $y^* < 1$ condition, then the mesh is further refined by reducing the initial cell height y and simulated again. This process is iterated until the $y^* < 1$ condition is met.

Smoothing Parameters

The irregular shape of the LEI wing profile and subsequent high degree of concavity observed in a numerical grid, as evident in the example of Figure 6.2, demands the use of mesh smoothing parameters in order to avoid numerical instabilities and prevent grid lines from intersecting. The hyperbolic extrusion method of Pointwise permits the application of *explicit smoothing*, *implicit smoothing*, *Kinsey Barth smoothing* and *volume smoothing*. The explicit and implicit smoothing parameters both act in the transverse direction, whereby the latter coefficient must always be double the value of the former (the default values are 0.5 and 1.0 respectively). The Kinsey Barth smoothing parameter acts in the wall-normal direction, has a default value of 0.0 and is typically activated in the event of severe concavities leading to grid line intersections. For such circumstances, it is recommended to use a coefficient value

greater than 3.0. Finally, the volume smoothing parameter controls the rate at which grid clustering is relaxed towards the front of the extrusion. This coefficient has a default value of 0.5, but can take any value between 0.0 and 1.0. A volume smoothing coefficient of 0.0 constitutes a fully intact grid clustering towards the boundary of the extruded domain.

Adjusting the mesh smoothing parameters for each individual grid generated for the purposes of this work would be arduous and excessive due to the sheer quantity of profiles under examination. As such, appropriate coefficient values have been determined by means of trial-and-error on a single airfoil. A highly cambered profile with the largest permissible tube diameter was chosen for this purpose in order to maximise the curvature and concavity observed in the numerical grid. A more stringent smoothing regime is required for such a grid since deterioration in mesh quality is more prevalent. The outcome of this approach is a set of smoothing coefficients that can be applied to a wide range of grids with varying degrees of curvature and concavity. The final outcome of the grid smoothing calibration performed on the airfoil in question is displayed in Figure 6.4.

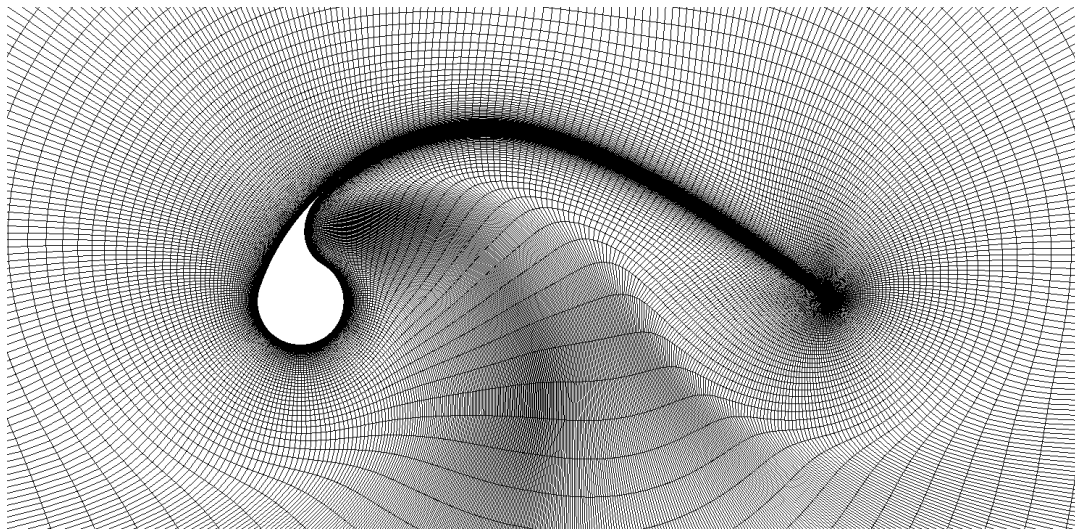


Figure 6.4: Mesh of the profile used to determine suitable smoothing coefficients. Shape parameters are $t = 0.15$, $\kappa = 0.3$ and $\eta = 0.4$. Grid resolution is 575×201 .

The coefficient values acquired from the grid smoothing calibration are the following:

Table 6.1: Values of hyperbolic extrusion smoothing parameters (see visual representations Figure 6.2 and Figure 6.4).

Smoothing parameter	Value	Notes
<i>Explicit</i>	5.0	
<i>Implicit</i>	10.0	Double the explicit coefficient
<i>Kinsey Barth</i>	5.0	High concavity $\rightarrow \geq 3.0$
<i>Volume</i>	0.5	Default value

The values presented in Table 6.1 have been consistently used for the purpose of generating smooth grids used throughout this study.

Stop Conditions

Hyperbolic mesh extrusion is immediately terminated upon the violation of the Jacobian grid quality criteria. The grid generation process ceases for cases which exhibit *positive skew*, *negative skew*, *zero Jacobian*, or *negative Jacobian*. Activating these criteria prevents the formation of negative volume or highly skewed cells.

6.1.3. Mesh Convergence

Failing to meet certain mesh generation standards may cause the CFD solver to never reach convergence or even to diverge. It is also possible that convergence is reached with a poor quality mesh, but at the expense of computational cost and/or simulation accuracy. The quality of a mesh depends on the level of grid refinement and an established set of quality metrics (skewness, cell orthogonality, etc.). Grid refinement affects the simulation accuracy, whereas the grid quality metrics influence the tendency towards convergence and the errors that arise from discretisation. Since a suitable cell count and grid density are not known *a priori*, a mesh convergence study is required to gauge the extent to which the simulation results vary with the level of refinement. As such, an appropriate range of “coarse” and “refined” grids have to be simulated at varied angles-of-attack and Reynolds numbers, after which the results are compared. [20]

The choice of Reynolds numbers for the mesh convergence simulations has been partly based on the experimental in-flight data based estimations presented in Section 2.3. Folkersma et al. [21] conducted numerical simulations using a wide range of Reynolds numbers, including values that are either close to or within the ranges expressed in Section 2.3, namely $Re = 2 \times 10^6$, $Re = 5 \times 10^6$ and $Re = 10 \times 10^6$. The aforementioned Reynolds numbers have been applied in this mesh convergence study in order to allow for comparisons with the numerical results of Folkersma et al. [21]. The numerical results in question are the 2D aerodynamic coefficients C_l , C_d and C_m defined as follows:

$$C_l = \frac{L}{\frac{1}{2}\rho_\infty U_\infty^2 S_r} \quad (6.6) \quad C_d = \frac{D}{\frac{1}{2}\rho_\infty U_\infty^2 S_r} \quad (6.7) \quad C_m = \frac{M}{\frac{1}{2}\rho_\infty U_\infty^2 S_r c} \quad (6.8)$$

The results presented in Table 6.2 and plotted in Figure 6.5 show that the level of refinement along the airfoil surface has a more prominent effect on the lift coefficient than on the other aerodynamic coefficients given $\alpha = 10^\circ$ and $Re = 5 \times 10^6$. It should be noted that the simulations for refinement levels 3 to 5 have not converged for $\alpha = 15^\circ$ since the aerodynamic coefficients do not stabilise over the range of iterations. As such, the results presented for these refinement levels given $\alpha = 15^\circ$ are not converged solutions (see Section 6.2.4). Converged solutions have been attained for each refinement level given $\alpha = 0^\circ$, yet a more prominent mesh dependency is evident compared to the results of $\alpha = 10^\circ$. This is likely a result of pressure side instabilities arising from the recirculation zone behind the leading-edge tube, which is more prominent at lower angles-of-attack and thus leads to greater mesh sensitivity. Nevertheless, it is deemed that sufficient mesh convergence has been attained.

Table 6.2: Computed aerodynamic coefficients (rounded to three significant figures) given $Re = 5 \times 10^6$ for different mesh resolutions **tangent to the surface** of an airfoil with shape parameter specifications $t = 0.15$, $\kappa = 0.3$ and $\eta = 0.4$.

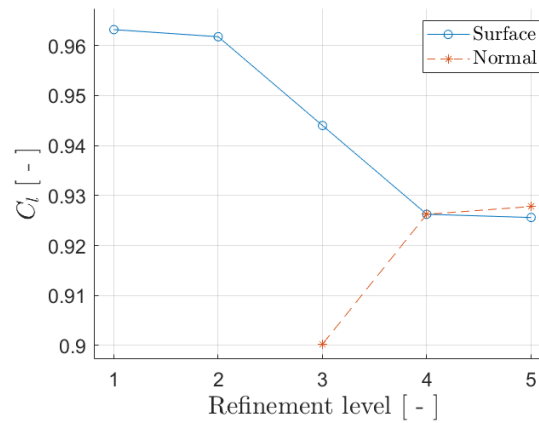
Mesh Resolution	C_l			C_d			C_m		
	$\alpha = 0^\circ$	$\alpha = 10^\circ$	$\alpha = 15^\circ$	$\alpha = 0^\circ$	$\alpha = 10^\circ$	$\alpha = 15^\circ$	$\alpha = 0^\circ$	$\alpha = 10^\circ$	$\alpha = 15^\circ$
171×201 (Level 1)	-0.340	0.963	1.392	0.0906	0.166	0.224	0.0625	-0.214	-0.283
255×201 (Level 2)	-0.329	0.962	1.367	0.0830	0.162	0.221	0.0639	-0.212	-0.278
384×201 (Level 3)	-0.336	0.944	1.408	0.0815	0.162	0.253	0.0644	-0.210	-0.296
575×201 (Level 4)	-0.343	0.926	1.367	0.0801	0.164	0.259	0.0644	-0.210	-0.293
864×201 (Level 5)	-0.331	0.926	1.492	0.0765	0.165	0.300	0.0578	-0.215	-0.326

The mesh refinement levels in the wall normal direction were selected such that the outer boundary of the grid domain maintains a distinct circular profile. This outcome is not guaranteed for surface normal resolutions below the lowest observed refinement level (level 3 in this case). Table 6.3 shows that the effects of the surface normal refinement level are inconsequential with regard to the aerodynamic coefficients and dimensionless wall distance y^* , with the exception of the change in lift coefficient from refinement level 3 to 4 for each observed Reynolds number. Otherwise, the number of mesh layers in the wall normal direction is a near arbitrary quantity. Another observation is the fact that even small changes in the Reynolds number seems to affect the aerodynamic coefficients quite substantially, which is not the case in the work of Folkersma et al. [21]. However, this is likely due to geometric differences between the simulated profiles, as the work of Folkersma et al. [21] examined a far more moderately

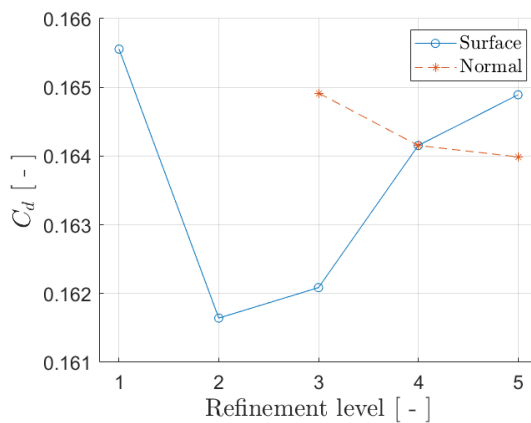
cambered airfoil with a lower tube diameter.

Table 6.3: Computed aerodynamic coefficients (rounded to three significant figures) given $\alpha = 10^\circ$ for different mesh resolutions **normal to the surface** of an airfoil with shape parameter specifications $t = 0.15$, $\kappa = 0.3$ and $\eta = 0.4$.

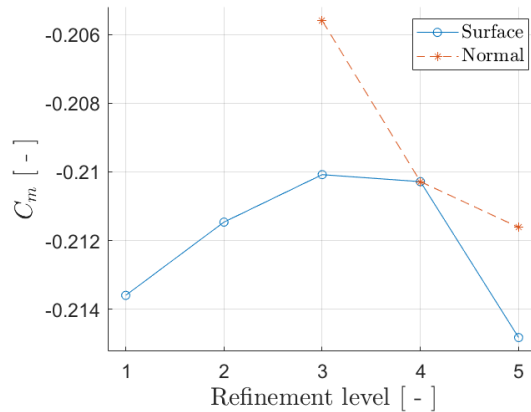
Dimensionless Coefficient [-]	Reynolds Numbers [-]	Mesh Resolutions		
		575×136 (Level 3)	575×201 (Level 4)	575×301 (Level 5)
y_{max}^*	2×10^6	0.128	0.129	0.129
	5×10^6	0.150	0.152	0.152
	10×10^6	0.175	0.176	0.176
C_l	2×10^6	0.743	0.760	0.763
	5×10^6	0.900	0.926	0.928
	10×10^6	1.018	1.056	1.055
C_d	2×10^6	0.176	0.176	0.176
	5×10^6	0.165	0.164	0.164
	10×10^6	0.156	0.154	0.153
C_m	2×10^6	-0.181	-0.184	-0.185
	5×10^6	-0.206	-0.210	-0.212
	10×10^6	-0.222	-0.229	-0.230



(a) Lift coefficients per refinement level.



(b) Drag coefficients per refinement level.



(c) Moment coefficients per refinement level.

Figure 6.5: Aerodynamic coefficients per mesh refinement levels of a parameterised LEI wing airfoil with shape parameters $t = 0.15$, $\kappa = 0.3$ and $\eta = 0.4$ at $\alpha = 10^\circ$ given $Re = 5 \times 10^6$.

6.2. Simulation Set-Up

An in-depth look at the employed CFD simulation set-up starts with a brief summary of the simulation platform in Section 6.2.1. What follows is a detailed description of the applied boundary conditions and initial values in Section 6.2.2, then an exploration of the numerical schemes and solver control settings in Section 6.2.3. Concluding this section is an explanation of the applied simulation convergence monitors in Section 6.2.4.

6.2.1. Simulation Platform

Constructing a polynomial regression model based on CFD data necessitates a considerable amount of simulations due to the many possible configurations of a parameterised LEI kite airfoil. The high performance computer cluster maintained by the Faculty of Aerospace Engineering at the Delft University of Technology has been used for this purpose. Known as the *HPC-12* cluster, this platform is capable of performing large scale parallel computations that would otherwise not be feasible on a single work station. As such, due to the high computational demands of simulating a vast range of airfoil configurations, the HPC-12 cluster has been used to carry out the bulk of the simulations required for this project. Since the operating system of the cluster is Linux-based, a basic grasp of the Linux command line is demanded of the user. The HPC-12 cluster is a *Beowulf* class computer cluster in which an assembly of nodes are connected through a local network to a master node. Each node is an individual computer where parallel computational tasks are executed, whereas the purpose of the master node is to plan and manage the tasks submitted by all users in a queuing system [26]. The master node is accessed via an SSH link between the HPC-12 cluster and the user's work station, permitting remote submission of computational tasks referred to as 'jobs'.

6.2.2. Boundary Conditions & Initial Values

Rather than assessing the effects of the boundary conditions and initial values, this study has appropriated the set-up applied in the work of Folkersma et al. [21]. This calls for a probing of the employed boundary conditions and initial values.

Far-field

The velocity vector \vec{U}_i of the flow at the inlet is defined by Equation (6.9) as a function of the angle-of-attack α and the free-stream velocity magnitude U_∞ . The vector components i , j and k denote the chordwise, transverse and spanwise directions respectively. In the case of two-dimensional flow, the spanwise vector component drops out (i.e. $k = 0$) since side-slipping flow is inherently unfeasible.

$$\vec{U}_i = U_\infty \cdot (i, j, k) = U_\infty \cdot (\cos(\alpha), \sin(\alpha), 0) \quad (6.9)$$

Adjusting the inlet velocity vector with the angle-of-attack omits the need to rotate and re-mesh the airfoil geometry. This is made possible by the O-grid topology of the structured grids.

The turbulent kinetic energy at the inlet k_i depends on the free-stream velocity U_∞ and the turbulence intensity I :

$$k_i = \frac{3}{2} (U_\infty I)^2 \quad (6.10)$$

The specific turbulent dissipation rate at the inlet ω_i is a function of the initial turbulent kinetic energy k_i and the free-stream eddy viscosity ratio $\frac{\nu_t}{\nu_\infty}$:

$$\omega_i = \frac{k_i}{\nu_\infty} \left(\frac{\nu_t}{\nu_\infty} \right)^{-1} \quad (6.11)$$

Given the context of low-turbulence external aerodynamics, prescribing an eddy viscosity ratio is preferable to estimating a turbulent length scale. The latter option is typically better suited for internal flows or flows in which the cause of turbulence can be attributed to a defining physical feature.

The free-stream eddy viscosity ratio $\frac{\nu_t}{\nu_\infty}$ and the turbulence intensity I at the inlet are prescribed quantities. Foldersma et al. [21] assessed the impact of varying the eddy viscosity ratio within the range $0.1 \leq \frac{\nu_t}{\nu_\infty} \leq 10$, concluding that the effects on the results are negligible. Demkowicz [16] came to the same conclusion for the range $1 \leq \frac{\nu_t}{\nu_\infty} \leq 50$, whilst also disclosing that varying the turbulence intensity from 0.5% to 20% similarly has an inconsequential outcome with regard to the aerodynamic coefficients. Demkowicz [16] and Foldersma et al. [21] conducted simulations with a constant turbulence intensity of 2% (i.e. $I = 0.02$) and a constant eddy viscosity ratio of $\frac{\nu_t}{\nu_\infty} = 10$. Therefore, in order to permit comparisons with the aforementioned studies, the same prescribed quantities have been used in this work.

Wall

A viscous fluid flowing across an impermeable solid will stick to the boundary of that solid. The so-called *no-slip* boundary condition follows from this viscous flow phenomena, stating that the velocity of a viscous fluid relative to a solid impermeable boundary is equal to the velocity at which the wall travels. The assumption of impermeability equates the velocity of the flow normal to a solid boundary to the normal velocity of the wall itself. Therefore, in the case of a stationary impermeable solid boundary, the tangential and normal velocity components of the flow at any point on the wall are both equal to zero. This condition applies to both the mean and fluctuating velocities. [19, 46]

Since the effects of turbulent fluctuations are inconsequential in the immediate vicinity of an impermeable solid boundary, the flow in this region is essentially laminar even in the context of a fully turbulent boundary layer. As such, a turbulent boundary layer can be divided into *sub-layers*, whereby the effectively laminar near-wall region is referred to as the *viscous sub-layer*. Since the viscous sub-layer is characterised by an effectively laminar flow regime, both the turbulent kinetic energy k and eddy viscosity ν_t at the wall are zero. As such, the effective viscosity at the wall $\nu_w (= \nu + \nu_t)$ is equivalent to the molecular viscosity of the fluid ν since $\nu_t = 0$. In contrast, the specific turbulent dissipation rate ω is not zero at the wall due to the damping effect a solid boundary has on turbulent fluctuations. [19]

OpenFOAM Boundary Settings

The initial values and types of boundary conditions used in the OpenFOAM set-up have been summarised in Table 6.4:

Table 6.4: OpenFOAM initial values and boundary conditions

Variable	Far-field type	Far-field value	Wall type	Wall value
U [m/s]	inletOutlet	inletValue = U_i Initial value = U_i	fixedValue	(0, 0, 0)
$P (= p/\rho)$ [m^2/s^2]	outletInlet	outletValue = 0 Initial value = 0	zeroGradient	-
k [m^2/s^2]	inletOutlet	inletValue = k_i Initial value = k_i	fixedValue	Value = 0
ω [1/s]	inletOutlet	inletValue = ω_i Initial value = ω_i	omegaWallFunction	Initial value = ω_i
ν_t [m^2/s]	calculated	Initial value = 0	nutkWallFunction	Initial value = 0

The `inletOutlet` and `outletInlet` boundary types have been applied to the far-field such that initial values can be prescribed for the given variables either at the inflow or the outflow respectively. Regarding the

inletOutlet boundary type, a fixed value is prescribed by the user at the inflow whilst a zero-gradient condition is imposed at the outflow. The reverse applies to the outletInlet boundary type, in which case the zero-gradient condition is administered to the inflow whilst a user-prescribed fixed value is specified at the outflow.

The calculated boundary type has been used to determine the eddy viscosity ν_t at the far-field since it is calculated using the prescribed inlet values of the turbulent quantities. In the case of the $k - \omega$ SST turbulence model, the eddy viscosity at the inlet is calculated using Equation (4.10) with k_i and ω_i (Equation (6.10) and Equation (6.11) respectively). Nevertheless, an arbitrary initial value has to be prescribed to start the simulation, as is the case for a variable to which a wall function has been applied.

The nutkWallFunction boundary type sets the eddy viscosity in the wall adjacent cells to $\nu_t = 0$ if the viscous sub-layer is resolved. Having met this condition, the effective viscosity at any point within the confines of a wall adjacent cell is equivalent to the molecular kinematic viscosity of the fluid ν . Also worth noting, the nutkWallFunction boundary type applies the turbulent kinetic energy based dimensionless wall-normal distance y^* instead of the wall shear stress based y^+ :

$$y^* = \frac{y_p \sqrt{C_\mu^{1/2} k_p}}{\nu} \quad (6.12)$$

As shown by Equation (6.12), the wall coordinate y^* is a function of the kinematic viscosity of the fluid ν , the empirical constant $C_\mu (= 0.09)$, the turbulent kinetic energy at the cell centroid k_p and the normal distance between the wall (at $y = 0$) and the cell centroid y_p . As is the case with y^+ , a condition of $y^* < 1$ must be met.

The turbulent kinetic energy at the wall has been prescribed a fixed value of $k_w = 0$. The same does not apply to the specific turbulent dissipation rate at the wall ω_w given the following near-wall condition [30]:

$$\omega \rightarrow \frac{6\nu}{\beta_1 y^2} \quad \text{as } y \rightarrow 0 \quad (6.13)$$

Nevertheless, an arbitrary non-zero initial value is prescribed at the wall: $\omega_w = \omega_i$. What follows is the calculation of the specific turbulent dissipation rate at the centroid of each wall adjacent cell ω_p by means of the omegaWallFunction boundary type:

$$\omega_p = \frac{6\nu}{\beta_1 y_p^2} \quad (6.14)$$

6.2.3. Numerical Schemes & Solver Control Settings

The following mathematical terms calculated in OpenFOAM simulations are approximated using numerical schemes:

- *Time derivatives:* $\frac{\partial}{\partial t}, \frac{\partial^2}{\partial t^2}$
- *Gradient terms:* ∇
- *Divergence terms:* $\nabla \cdot$
- *Laplacian terms:* ∇^2
- *Interpolation schemes:* Interpolation of values from cell centroid to cell faces.
- *Surface normal gradient terms:* Cell face normal gradient component.

The numerical schemes applied to the mathematical terms listed above are assigned in the `fvSchemes` dictionary and have been listed (in OpenFOAM format) in Table 6.5. Assessing the capabilities of different numerical schemes available in OpenFOAM is beyond the scope of this work. As such, the same settings applied in the work of Folkersma et al. [21] have been utilised.

Table 6.5: Applied numerical schemes

Category	Numerical scheme
Time	<code>steadyState</code>
Gradient	<code>Gauss linear</code>
Divergence (U)	<code>bounded Gauss linearUpwind default</code>
Divergence (k, ω)	<code>bounded Gauss upwind</code>
Laplacian	<code>Gauss linear corrected</code>
Interpolation	<code>linear</code>
Surface normal gradient	<code>corrected</code>

Since the `simpleFoam` solver is inherently steady-state, all time derivatives have been set to zero by applying the `steadyState` time scheme. Assigning a transient numerical scheme instead would lead to erroneous solutions. Gradient terms have been approximated by means of the `Gauss linear` numerical scheme, the implication being that Gaussian integration comprises a linear interpolation from the cell node centres to the cell faces.

Numerical schemes are assigned to advective terms by using the `div(phi,...)` identifier, where the `phi` term denotes the volumetric velocity flux at the cell faces when simulating incompressible flow: $\phi = U_f \cdot S_f$. Gauss integration forms the basis of all divergence schemes, where the `bounded` version is used in order to improve the stability of the steady-state solution convergence. The `upwind` interpolation scheme is first order and bounded, whereas the `linearUpwind` interpolation scheme is second order, unbounded and upwind-biased. The latter interpolation scheme requires an assigned velocity gradient discretisation and is not available for the advection of scalar fields such as the turbulent quantities k and ω .

As with any CFD solver utilising the finite volume method, flow variables are calculated and stored at the centroid of a cell. This necessitates the implementation of an interpolation scheme in order to calculate the values of the flow variables at the centre of each cell face. This only concerns internal faces that connect two cells, whereas the treatment of boundary faces that connect a cell to the wall has been described in Section 6.2.2. The calculation of a flow variable quantity at the centre of an internal face depends on the values stored at the centroids of the connected cells (the owner cell and the neighbouring cell). Linear (central differencing) interpolation is the most straightforward scheme since the variation of a flow field quantity between cell centroids is linear. Although a second order accurate interpolation scheme, its unboundedness makes it prone to oscillations, a particularly detrimental phenomenon often observed in steady-state simulations. Whilst suitable for interpolating the diffusion term $\nu \nabla^2 U$ in the RANS equations, the convection term $\nabla \cdot (UU)$ requires a different approach in order to prevent non-physical oscillations in the solution. An alternative interpolation scheme suitable for the convection term is the *upwind differencing* method, which is dependent on the mass flux direction. If the mass flows out of the owner cell, then the value of a flow variable at the shared cell face centre is equal to the centroid value of the owner cell. Otherwise, the value at the cell face centre is equal to the centroid value of the neighbouring cell for cases in which the mass flows into the owner cell. As such, upwind differencing is a first-order accurate interpolation scheme since the value of a flow variable remains constant between the centroid and the cell face centre. Although upwind differencing is not as accurate as central differencing, it is nonetheless more suitable for convection dominated flows since it is a bounded interpolation scheme that leads to non-oscillatory solutions. A more accurate alternative is the *linear upwind differencing* scheme which conducts an extrapolation using the gradient of the interpolated field quantity. This leads to a linear variation of the interpolated flow variable between the cell centroid and cell face centre, thus implying (nominal) second-order accuracy. But what is gained in solution accuracy is lost in stability due to the possible formation of local maxima and minima if the

gradient is not limited.

The surface normal gradient is the component of a gradient term normal to the centre of a shared face connecting two cells. If the face normal vector is not aligned with the vector connecting the two cell centroids, then the shared face is classified as *non-orthogonal* with the angle between the two vectors referred to as the *non-orthogonality angle*. Such is the case for the numerical grids simulated as part of this study (and most practical applications for that matter). Common convention dictates a highly non-orthogonal cell as comprising a non-orthogonality angle in excess of 70° , a guideline which OpenFOAM adheres to. Cells with non-orthogonality angles well below the aforementioned threshold, as observed in the grids simulated throughout this study, justify the application of the `corrected` numerical scheme to the surface normal gradient terms. This numerical scheme applies an explicit non-orthogonal correction for the purpose of maintaining second-order accuracy.

The `corrected` numerical scheme has also been used to evaluate the surface normal gradients of the Laplacian terms. Discretisation of the Laplacian terms is limited to the `Gauss` scheme where only the `linear` interpolation scheme can be applied to the diffusion coefficient. Linear interpolation of variables from cell centroids to face centres is made possible by the `linear` numerical scheme.

Table 6.6: Applied solver control settings

Category	Settings
Solver (p)	GAMG smoother GaussSeidel
Solver (U, k, ω)	smoothSolver smoother symGaussSeidel
SIMPLE	consistent yes nNonOrthogonalCorrectors 0
Relaxation factors Equations	
U	0.9
k, ω	0.7

The multi-grid method is capable of solving large sets of linear algebraic equations encountered in CFD simulations. The main working principle of the multi-grid method is to utilise solutions acquired from a coarse grid, which benefit from faster convergence due to smaller sets of algebraic equations, as initial conditions for solving a finer grid.

The numerical order of the cells in a grid is typically randomly generated by the mesh generation software. Since the cell numbering affects the convergence speed of the Gauss-Seidel algorithm, renumbering the cells of a mesh may lead to faster convergence. Mesh renumbering in OpenFOAM is realised by means of the Cuthill-McKee algorithm. Convergence is further improved with the symmetric Gauss-Seidel algorithm in which every other solution propagation acts in the opposite direction of the numerical order.

Grids comprising highly non-orthogonal cells require supplementary inner loops of the pressure equation when simulated with the SIMPLEC algorithm. Such additional inner loops are referred to as *non-orthogonal correctors* and are prescribed using the `nNonOrthogonalCorrectors` entry in the `fvSolution` dictionary. As displayed in Table 6.6, no additional non-orthogonal corrector loops have been introduced since the maximum non-orthogonality angle is well below the 70° threshold for all simulated grids. For such grids, convergence is attainable by means of the outer loops in the SIMPLEC algorithm. Introducing additional non-orthogonal correctors would slow-down the simulation with little added benefit.

Steady-state solvers are highly prone to divergence unless numerically stabilised. Alleviation of this adverse computational phenomenon is made possible by applying an iterative relaxation method. The

advancement of a steady-state solution, with relaxation, is similar to the development of a solution over time of a transient simulation. An iterative relaxation method assigns the same relaxation factor to every cell in the grid, which corresponds to a different pseudo time step in each cell. The value of the relaxation factor only affects the intermediate solutions of a flow variable and not the converged solution. A relaxation factor lower than one constitutes *under-relaxation*, which is the method applied to the flow variables listed in Table 6.6. Reducing the under-relaxation factor alleviates oscillatory motions and improves stability. However, convergence speed is increased with a larger under-relaxation factor. Default values of CFD solvers have been selected such that a careful balance is struck between stability and convergence speed based on a wide range of cases. OpenFOAM allows either explicit or implicit relaxation, whereby the former method modifies a field quantity directly and the latter method adapts the algebraic equations of a field quantity prior to solving. Under-relaxation of the pressure field is inherently absent in the context of a consistent formulation of the SIMPLE algorithm. The remaining variables have been subject to implicit under-relaxation, proposed by Patankar [34] as a means to address momentum equation non-linearities observed in the SIMPLE algorithm.

6.2.4. Convergence Monitoring

Assessing whether a steady-state CFD simulation has converged requires a considerable number of iterations for greater assurance. For this particular convergence study, a fixed total of 5000 iterations per simulation was deemed suitable when accounting for computational cost and simulation accuracy. The conventional means of assessing simulation convergence is to monitor the progression of the initial residual of each flow variable over the full range of iterations. However, using the progression of the initial residuals as the sole measure of convergence would lead to an insufficient and incomplete conclusion. For this reason, convergence is also monitored via the progression of the aerodynamic coefficients over the fixed iteration range. As an example, Figure 6.6 displays the progression of the residuals and aerodynamic coefficients of a converged simulation. The continually decreasing residuals and stabilised aerodynamic coefficients are characteristics that reliably indicate convergence.

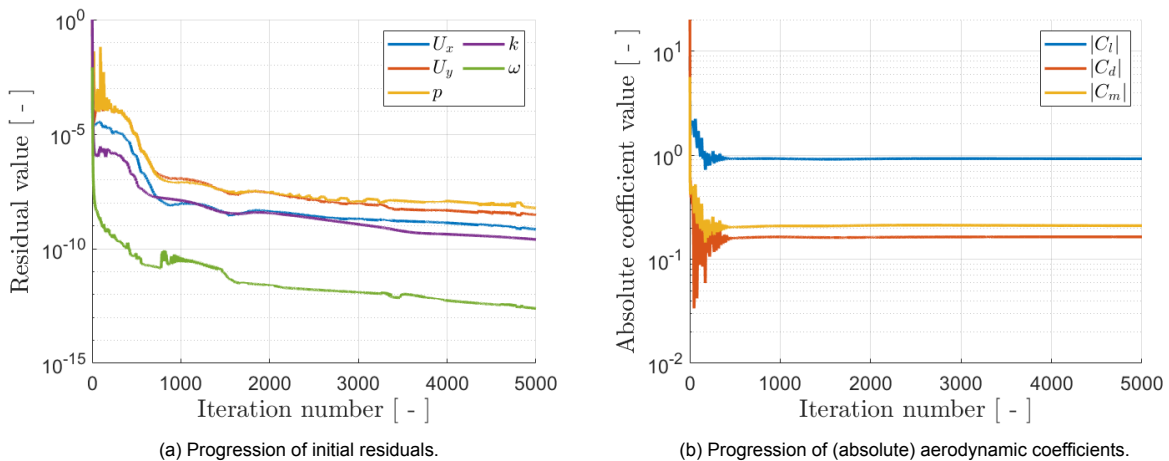
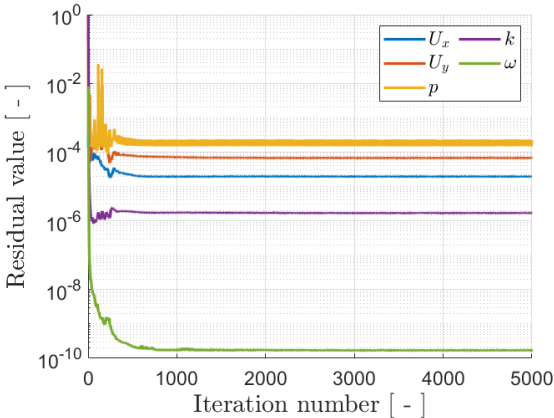
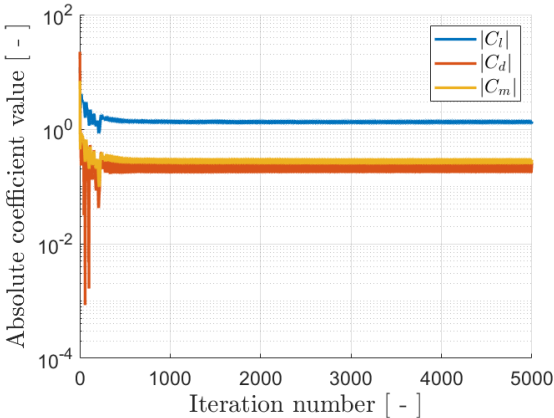


Figure 6.6: Example of converged simulation of LEI wing profile with parameters $t = 0.15$, $\kappa = 0.3$ and $\eta = 0.4$ at $\alpha = 10^\circ$.

In contrast, stagnant residuals and oscillating aerodynamic coefficients imply that a simulation has not converged, as is the case for the progressions displayed in Figure 6.7. The oscillatory motions evident in Figure 6.7 are indicative of transient flow behaviour since unsteadiness in the flow field can be manifested as unsteadiness in the residual progressions. Poor mesh quality and poorly specified boundary conditions may also be the cause of oscillatory progressions. In order to gauge the true cause of the oscillatory motions, it is necessary to conduct transient simulations.



(a) Progression of initial residuals.



(b) Progression of (absolute) aerodynamic coefficients.

Figure 6.7: Example of non-converged simulation of LEI wing profile with parameters $t = 0.15$, $\kappa = 0.3$ and $\eta = 0.4$ at $\alpha = 15^\circ$.

LEI Wing Profile Aerodynamics

Results from the CFD simulations have been visualised, examined and scrutinised in this chapter in order to gain insight into the various flow phenomena endured by a LEI wing profile immersed in a flow field. All results presented in this chapter have been acquired from CFD simulations given $Re = 5 \times 10^6$. Every measurement of the moment coefficient C_m has been taken about the quarter-chord point $c/4$. The effects of the non-dimensional shape parameters on the flow fields and the aerodynamic coefficients have been examined in Section 7.1. The findings of this study have been compared to the results of preceding studies in Section 7.2.

7.1. Shape Parameter Effects

A scrutiny of the applied airfoil parameterisation is made viable through examining the holistic effects the non-dimensional shape parameters have on the aerodynamic loads acting on a LEI wing profile immersed in a flow field. The purpose of this analysis is to gauge whether the applied non-dimensional shape parameters are indeed required to accurately represent the geometry of a parameterised airfoil. Of particular interest is how the incorporation of the chordwise position of maximum camber η as a shape parameter affects the flow field since this has not been examined in the study of Breukels [7]. As such, the influences of the shape parameters on the flow field have been individually assessed and compared.

A crucial aspect of this analysis has been to examine the impact the shape parameters have on reversed flow regions. The occurrence of flow reversal is certified by the chordwise distribution of the x -component of the local skin friction coefficient $c_{f,x}$ (defined by Equation (7.1)) since a negative value of $c_{f,x}$ is a manifestation of flow reversal.

$$c_{f,x} = \frac{\tau_{w,x}}{\frac{1}{2}\rho_{\infty}U_{\infty}^2} \quad (7.1)$$

As is evident in Equation (7.1), $c_{f,x}$ is dependent on the x -component of the wall shear stress $\tau_{w,x}$:

$$\tau_{w,x} = \mu \left. \frac{\partial U_x}{\partial y} \right|_{y=0} \quad (7.2)$$

Furthermore, the extent to which the shape parameters affect the chordwise distribution of the pressure

coefficient C_p has also been examined:

$$C_p = \frac{p - p_\infty}{\frac{1}{2}\rho_\infty U_\infty^2} \quad (7.3)$$

The chordwise distribution of C_p provides insight into the flow field characteristics since flow separation is caused by a steep adverse pressure gradient, which entails a rapid increase in the static pressure p downstream. A consequence of flow separation is a substantial decrease in lift and the introduction of pressure drag, which increases the total drag exerted on the airfoil. The distribution of C_p along the chord length also reveals the position of the stagnation point, where $C_p = 1$ for incompressible flows, near the leading edge.

Regarding flow simulations that incorporate transition modelling, the chordwise distributions of $c_{f,x}$ and of C_p can be used to estimate the point at which the boundary layer transitions from laminar to turbulent. In the case of the chordwise distribution of $c_{f,x}$, an abrupt increase away from the leading edge (assuming a low enough Reynolds number) is indicative of laminar-to-turbulent transition. As to the chordwise distribution of C_p , it is known that a favourable pressure gradient (implying a downstream decrease in the static pressure p) near the leading edge helps preserve laminar flow, whereas an adverse pressure gradient promotes the onset of boundary layer transition.

Nevertheless, the assumption of a fully turbulent boundary layer with regard to the simulations conducted for the purposes of this study negates the occurrence of laminar flow and a subsequent downstream delay in transition. As such, a downstream surge in $c_{f,x}$ is only observed near the leading edge and the presence of a steep adverse pressure gradient is solely a manifestation of flow separation.

7.1.1. Non-dimensional LE Tube Diameter t

The influence of the LE tube diameter is manifested by the non-dimensional airfoil thickness t (i.e. non-dimensional tube diameter). For each case displayed in Figure 7.1, C_l decreases with t . It is also evident that increments in the maximum camber magnitude κ do not always lead to an increase in C_l as is observed for $\alpha = 10^\circ$. In fact, at $\alpha = 15^\circ$ an increase in κ leads to a decrease in C_l , which is not the case for $\alpha = 0^\circ$ and $\alpha = 5^\circ$.

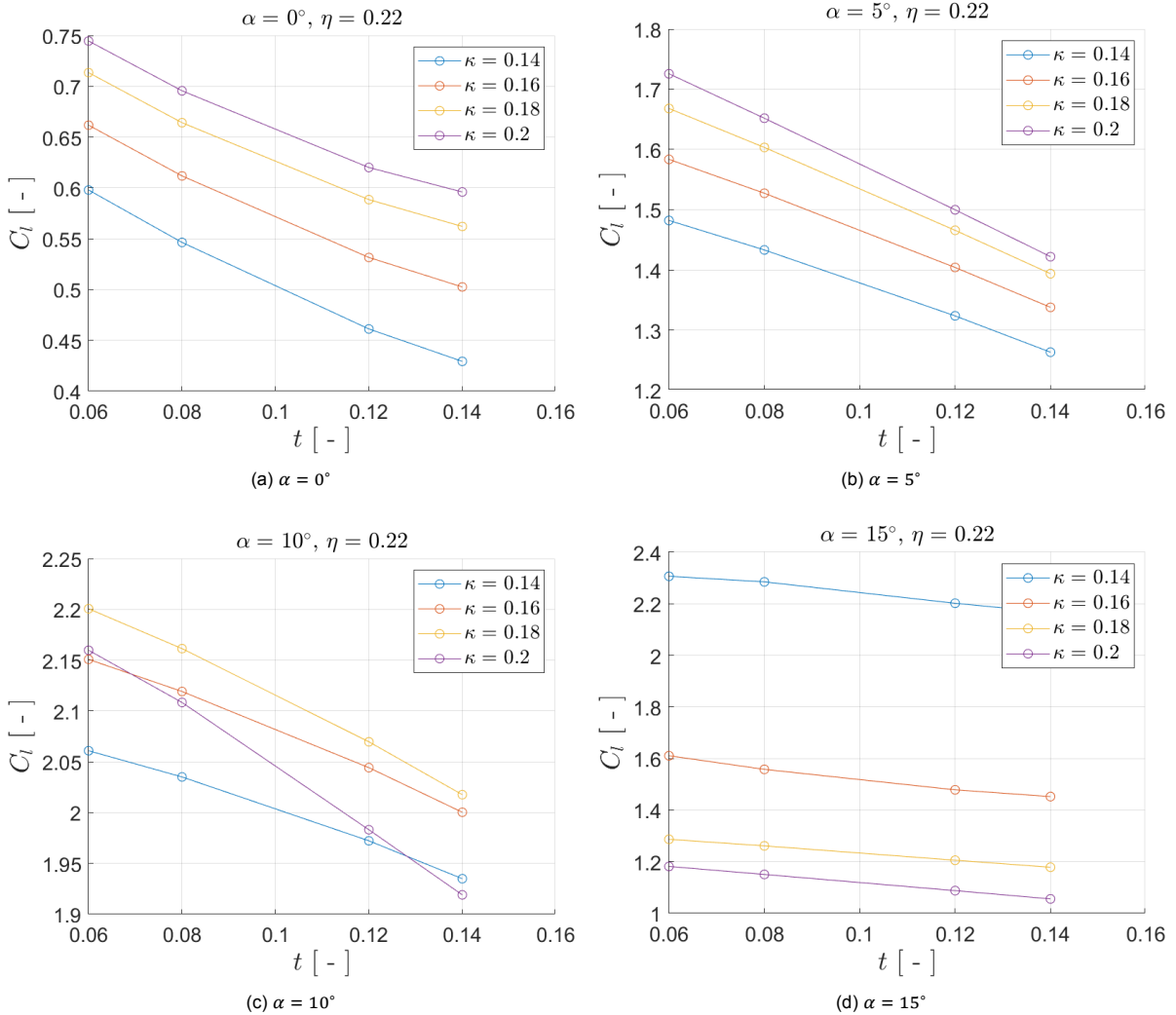


Figure 7.1: C_l versus t given a constant $\eta = 0.22$ and varying κ .

Figure 7.2 shows that C_d increases with t for $\alpha = 0^\circ, 5^\circ$ and 10° for all displayed curves. In the case of $\alpha = 15^\circ$, the aforementioned trend appears to be reversed for larger values of κ . What is apparent though is that an increase in κ leads to an increase in C_d for each observed angle-of-attack.

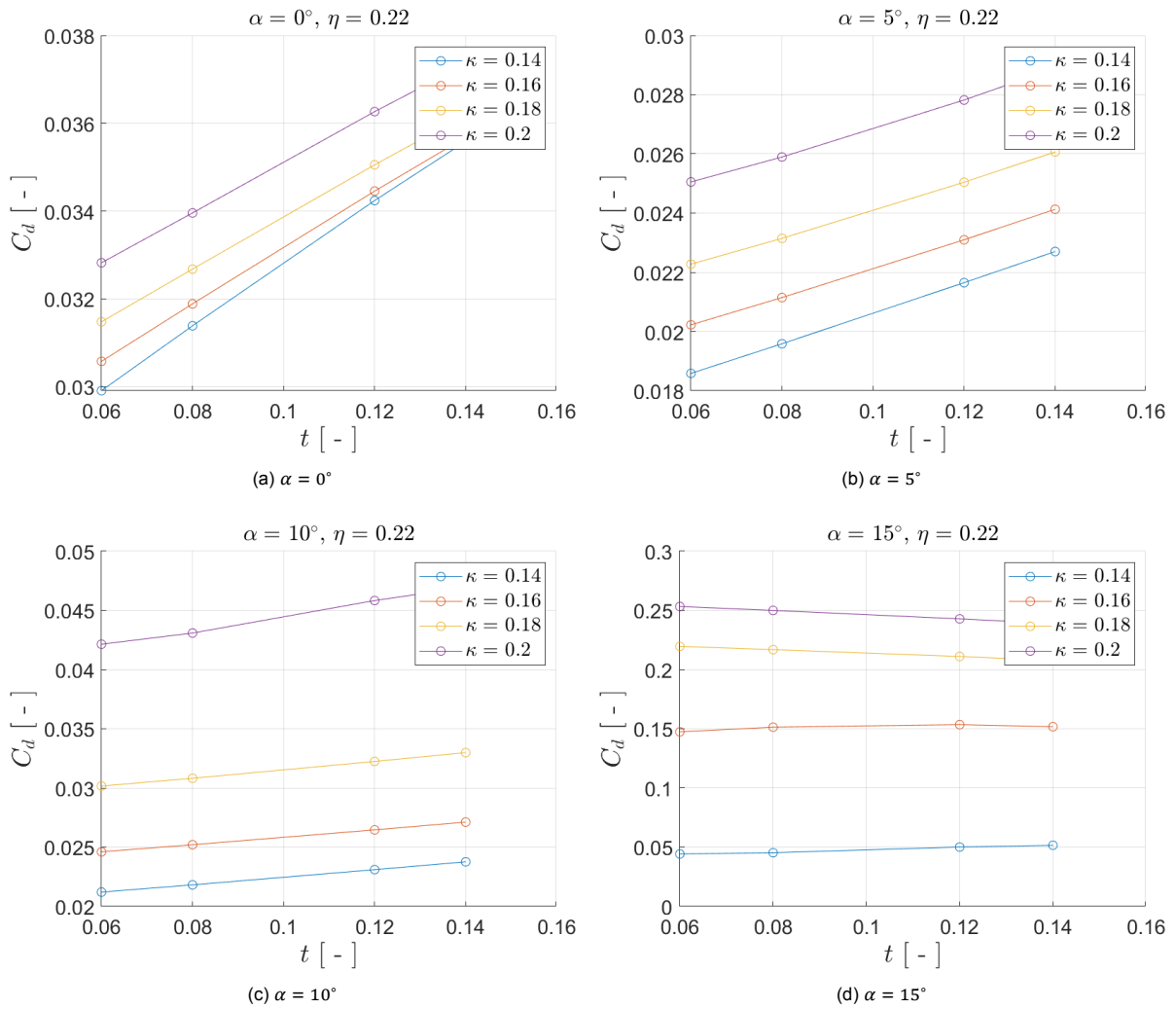


Figure 7.2: C_d versus t given a constant $\eta = 0.22$ and varying κ .

Judging from Figure 7.3, increments in C_m with t are evident for $\alpha = 0^\circ, 5^\circ$ and 10° . For $\alpha = 15^\circ$, it is clear that the effects of t on C_m are negligible for the low maximum camber magnitudes $\kappa = 0.14$ and 0.16 , whereas small increments in C_m with t are evident for the larger $\kappa = 0.18$ and 0.20 . Furthermore, the impact of κ on C_m becomes more pronounced as the angle-of-attack increases.

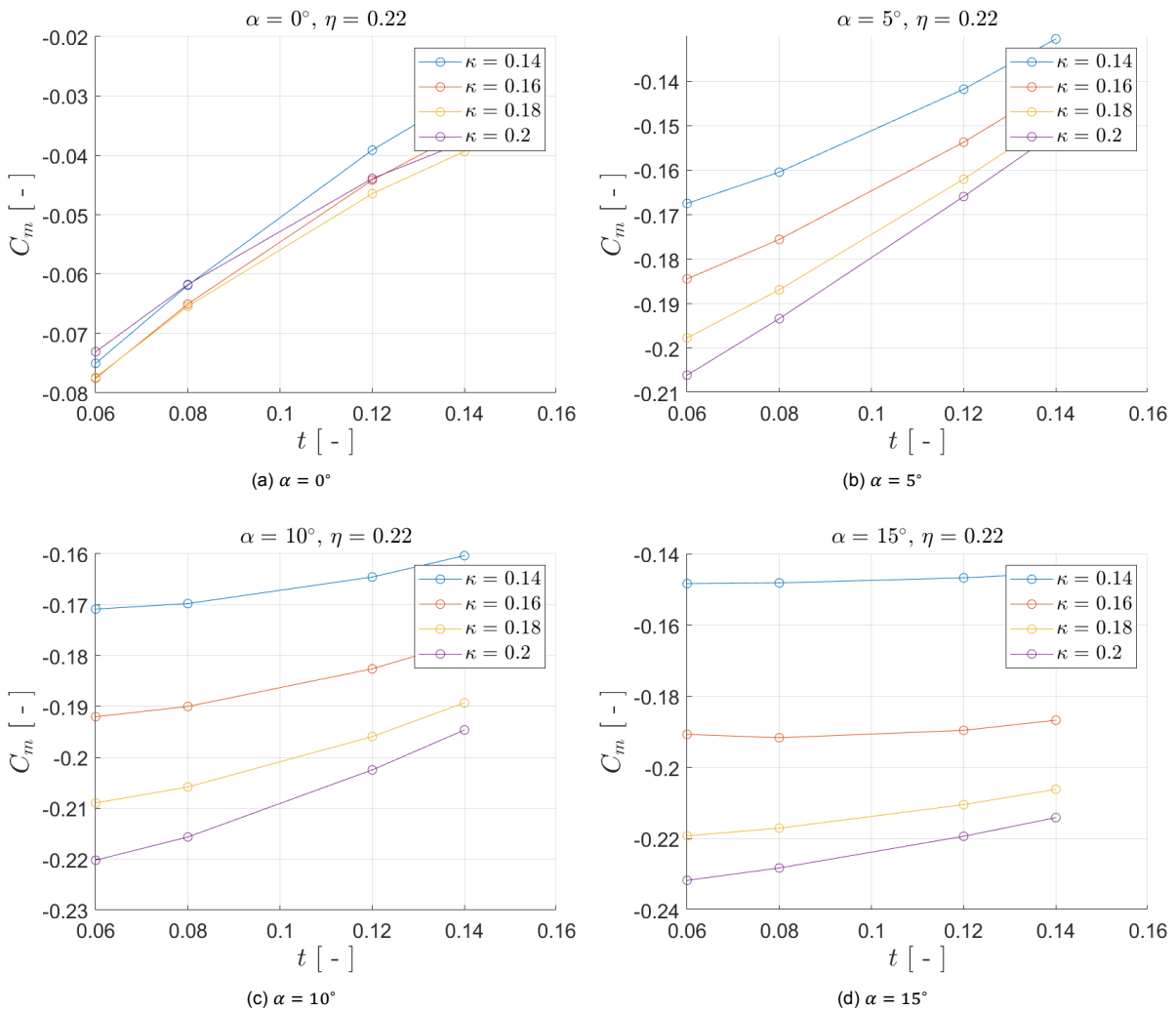


Figure 7.3: C_m versus t given a constant $\eta = 0.22$ and varying κ .

The $c_{f,x}$ distributions displayed in Figure 7.4 show that the flow remains fully attached over the suction side for each observed value of t given $\alpha = 0^\circ$. The small variations in the suction side $c_{f,x}$ distribution with increasing t evidently show mild changes in the shape of the membrane canopy near the leading edge. Varying t changes the slope at the canopy-tube intersection point, thus affecting the suction-side flow near the leading edge. Switches in sign of $c_{f,x}$ on the pressure side are delayed with increasing t . The implication of these delays is that increments in t cause the pressure-side separation and reattachment points to shift further downstream. Nevertheless, the region of recirculating flow behind the LE tube on the pressure side remains relatively consistent in chordwise length with increasing values of t .

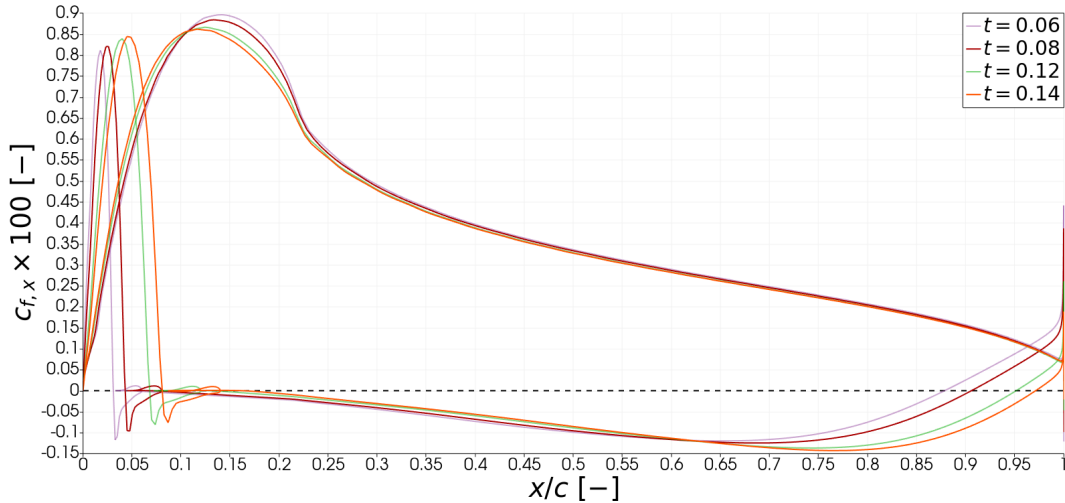


Figure 7.4: Chordwise distributions of $c_{f,x}$ for different values of t given $\alpha = 0^\circ$, $\kappa = 0.14$ and $\eta = 0.22$.

The occurrence of suction-side flow separation given $\alpha = 15^\circ$ is clearly distinguishable for all observed values of t in Figure 7.5. The movement of the suction-side separation point with increasing t is rather muted compared to the downstream shift of the pressure-side separation and reattachment points. Similar to the $\alpha = 0^\circ$ case, the chordwise length of the pressure-side recirculating flow region remains relatively stable the same with varying t . What is also apparent is the negative peak near the leading edge that is quelled with increasing t and is the result of the flow having to move up the circular LE tube profile where $\tau_{w,x}$ acts opposite to the streamwise direction.

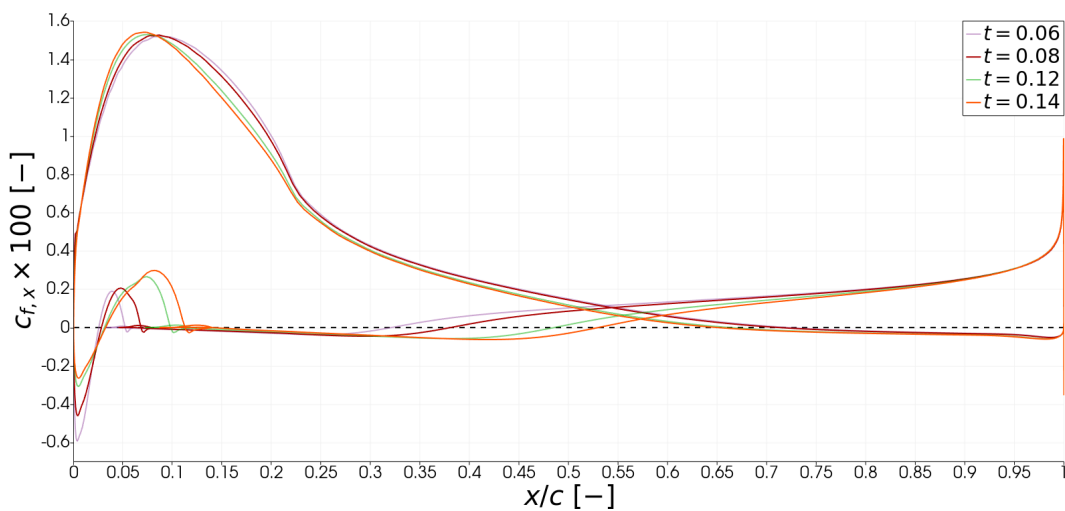


Figure 7.5: Chordwise distributions of $c_{f,x}$ for different values of t given $\alpha = 15^\circ$, $\kappa = 0.14$ and $\eta = 0.22$.

Substantial pressure-side load relief with increasing t is evident in Figure 7.6 over the entire length of the chord. Given $\alpha = 0^\circ$, the pressure-side recirculation zone encompasses almost the entire area enclosed by the membrane canopy. Increasing t also has the effect of mildly increasing the loads acting on the suction side due to the modest decrements of the suction-side peak. Whilst the suction-side adverse pressure gradient of each C_p distribution is not steep enough to facilitate flow separation, each distribution does display a strong adverse pressure gradient on the pressure side such that the flow separates from the leading-edge tube. An increase in t evidently shifts the pressure-side separation point further downstream given the changes in chordwise position of the adverse pressure gradient.

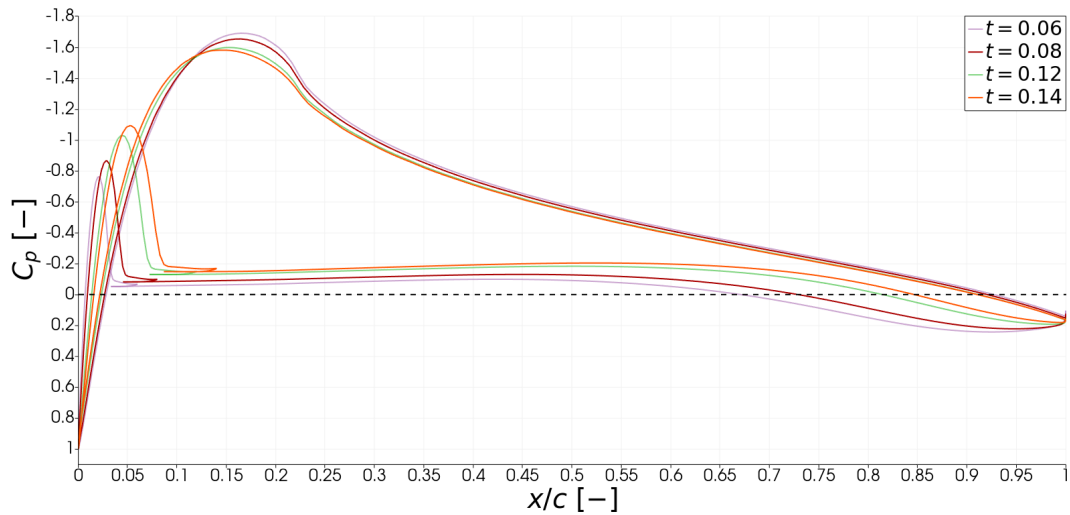


Figure 7.6: Chordwise distributions of C_p for different values of t given $\alpha = 0^\circ$, $\kappa = 0.14$ and $\eta = 0.22$.

Regarding the pressure distributions displayed in Figure 7.7, the pressure-side pressure gradient moves further downstream with increasing t given $\alpha = 15^\circ$, implying a delay in pressure-side flow separation. Increasing t also leads to a slight relieving of the pressure side load distribution upstream $x/c = 0.5$, which is the area encompassed by the diminished recirculating flow region (given the high angle-of-attack). As for suction-side flow separation, a slight alleviation of the pressure gradient is evident with increasing t .

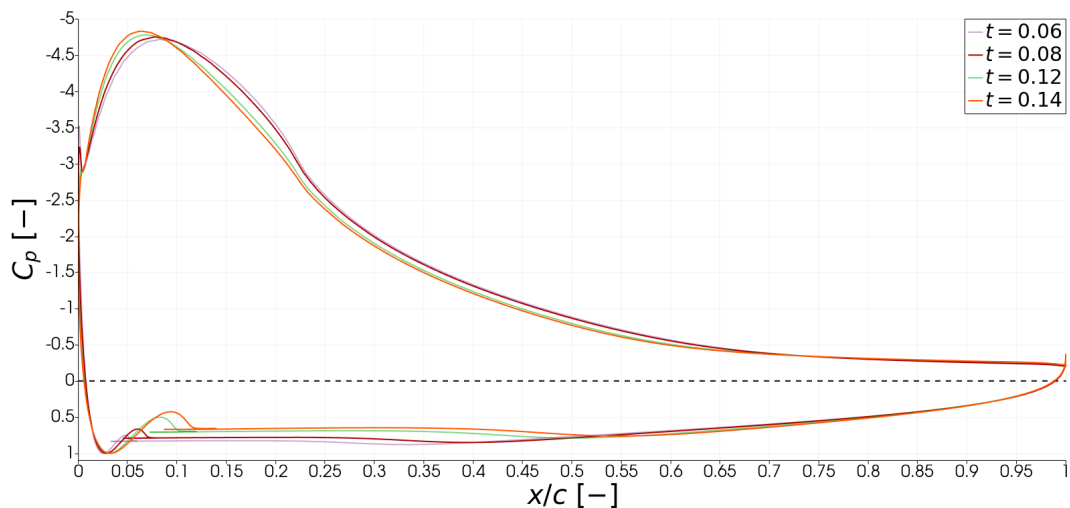


Figure 7.7: Chordwise distributions of C_p for different values of t given $\alpha = 15^\circ$, $\kappa = 0.14$ and $\eta = 0.22$.

The contour plot displayed in Figure 7.8 exhibits fully attached flow on the suction side and a region of recirculating flow on the pressure side of the LEI wing profile with shape parameters $\eta = 0.22$, $\kappa = 0.14$ and $t = 0.14$ immersed in a flow field given $\alpha = 0^\circ$. The region of recirculating flow emanating from the pressure side of the leading-edge tube extends nearly all the way to the trailing edge. The pressure-side separation point is approximately located at the bottom of the leading-edge tube, whereas the reattachment point is positioned just upstream the trailing edge. Comparing Figure 7.8 to Figure 7.17 and Figure 7.26 shows that an increase in the angle-of-attack leads to a decrease in the size of the recirculating flow region.

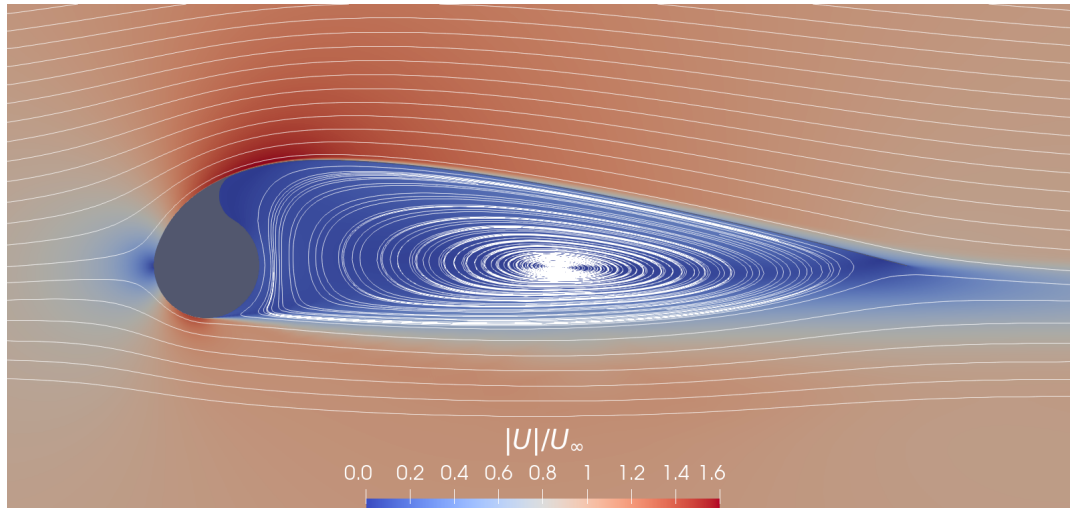
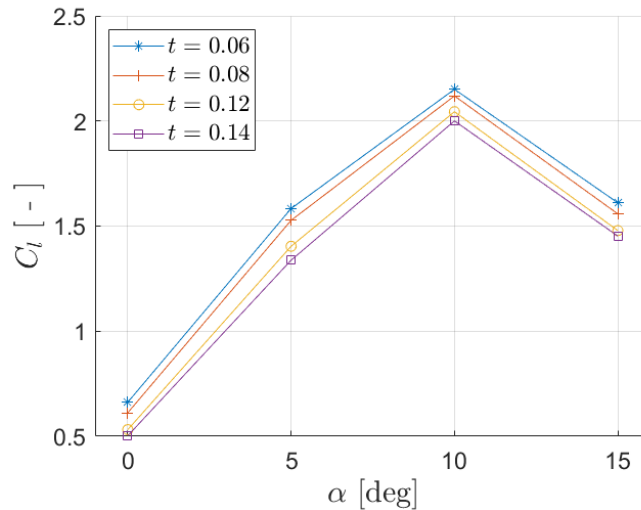


Figure 7.8: Visualisation of normalised flow velocity and streamlines around LEI wing profile with shape parameters $\eta = 0.22$, $\kappa = 0.14$ and $t = 0.14$ at $\alpha = 0^\circ$.

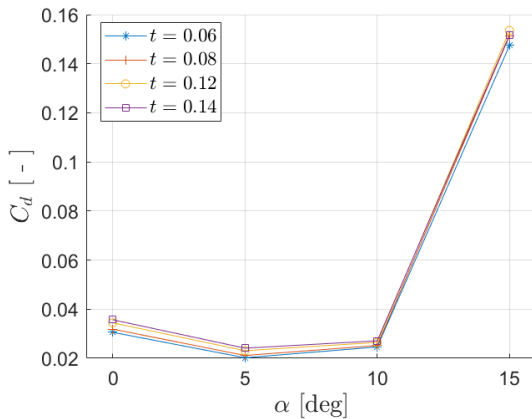
Whilst the pressure distribution along the suction side remains relatively consistent with varying values of t , Figure 7.6 shows an increase in t leads to a decrease in pressure on the pressure side given the same position along the chord. Therefore, increasing t reduces the pressure difference between the upper and lower surfaces, leading to a loss of lift and subsequent decrease in C_l as observed in Figure 7.1a. This outcome can be attributed to the fact that an increase in t shifts the pressure-side separation point further downwards, thus extending the vertical length of the pressure-side reversed flow region along the chord whilst maintaining an approximately constant chordwise length. The overall increase in size of this region of reversed flow is what causes the loss of lift and increase in pressure drag, leading to an increase in C_d with t evident in Figure 7.2a. The observed changes in the pressure-side pressure distribution with increasing t also have the effect of increasing C_m (see Figure 7.3a), thus diminishing the tendency of the airfoil to pitch downwards. The pressure difference near the trailing edge becomes more narrow with increasing t which subsequently relieves the rearward loading as a result. Given the large moment arms between loads exerted near the trailing edge and the quarter-chord point, the disposition to pitch-downwards is abated with increasing t and is manifested by a less negative C_m .

With increasing angle-of-attack, the overall size of the pressure-side recirculating flow region decreases as the reattachment point moves further upstream, thus leading to an increase in lift and decrease in pressure drag. This favourable development is subsequently counteracted by suction-side flow separation upon reaching $\alpha = 15^\circ$, causing a drop in lift evident in Figure 7.9a and introducing additional pressure drag leading. Figure 7.9b shows a decrease in C_d for all values of t with respect to the progression from $\alpha = 0^\circ$ to $\alpha = 5^\circ$. As the flow over the suction-side remains attached after the given rise in angle-of-attack, it is evident that the subsequent reduction in pressure drag due to a diminishing pressure-side recirculating flow region causes the drop in C_d . But in the progression from $\alpha = 5^\circ$ to $\alpha = 10^\circ$, C_d remains relatively the same. In this case, the decrease in pressure drag due to the pressure-side reversed flow region is balanced out by an increase in skin-friction drag and the introduction of additional pressure drag from a mild pocket of suction-side reversed flow at the trailing edge.

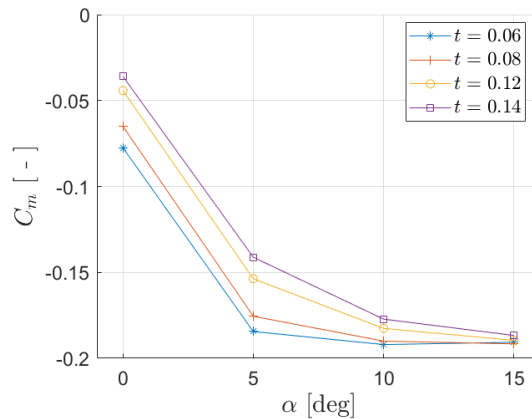
The ensuing surge in C_d going from $\alpha = 10^\circ$ to $\alpha = 15^\circ$ is a result of the increase in pressure drag due to separation from the suction-side largely overcoming the decrease in pressure drag from the pressure-side recirculating flow region. An increase in t also expands the wetted area (i.e. the total surface area exposed to the external flow) since the widening of the leading-edge tube diameter leads to a larger surface area on the pressure side. As displayed in Figure 7.4 and Figure 7.5, the pressure-side spike in $c_{f,x}$ over the leading-edge tube is prolonged given an increase in diameter, thus leading to an overall increase in skin-friction drag. Regarding C_m , Figure 7.9c shows that variations with t become more subdued for larger angles-of-attack, an observation which is supported by Figure 7.7 given the relatively small differences between the displayed pressure distributions of the applied range of t .



(a) C_l versus α .



(b) C_d versus α .



(c) C_m versus α .

Figure 7.9: Aerodynamic coefficients versus α for varying values of t given a constant $\eta = 0.22$ and $\kappa = 0.14$.

7.1.2. Chordwise Position of Maximum Camber η

Judging from Figure 7.10, the small increments in C_l with the chordwise position of maximum camber η at $\alpha = 0^\circ$, 5° and 10° suggest that η has a meager influence on C_l at low-to-moderate angles-of-attack. At $\alpha = 15^\circ$ the flow separates from the suction side of the airfoil (see Figure 7.14), leading to amplified changes in C_l with η . An increase in η delays the flow separation at $\alpha = 15^\circ$, thus leading to an increase in C_l . In all cases, C_l increases with η .

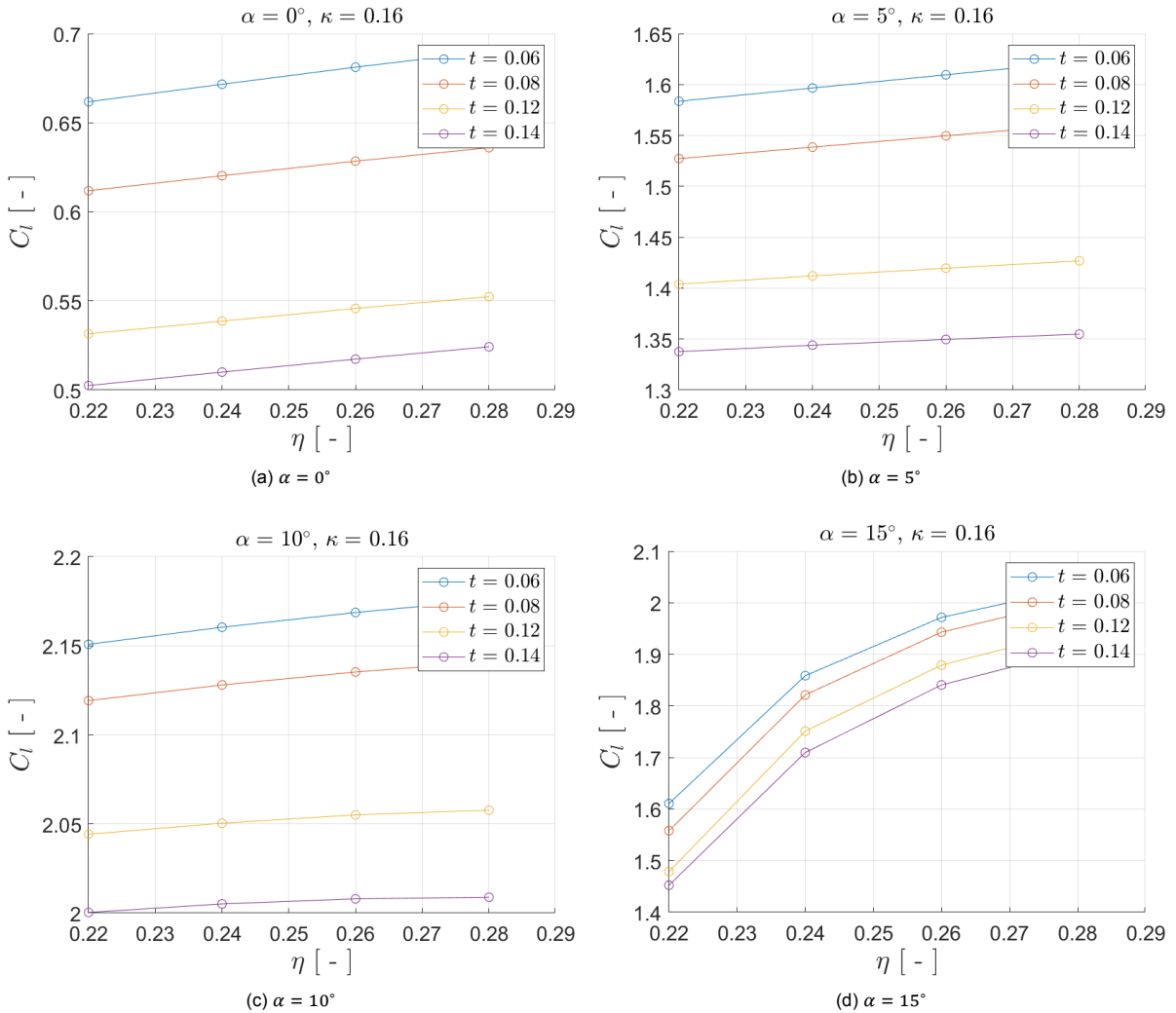


Figure 7.10: C_l versus η given a constant $\kappa = 0.16$ and varying t .

Figure 7.11 reveals a similar pattern for C_d as observed with C_l , namely that the chordwise position of maximum camber η has a greater influence on C_d as the angle-of-attack increases. The effects of η on C_d at $\alpha = 0^\circ$ and 5° appear to be inconsequential. Discernible increments in C_d with η are evident at $\alpha = 10^\circ$. But at $\alpha = 15^\circ$ the flow separates from the suction side of the airfoil, leading to more drastic changes in C_d as η is varied. As previously stated, flow separation is delayed with increasing η , which leads to a drop in C_d at $\alpha = 15^\circ$.

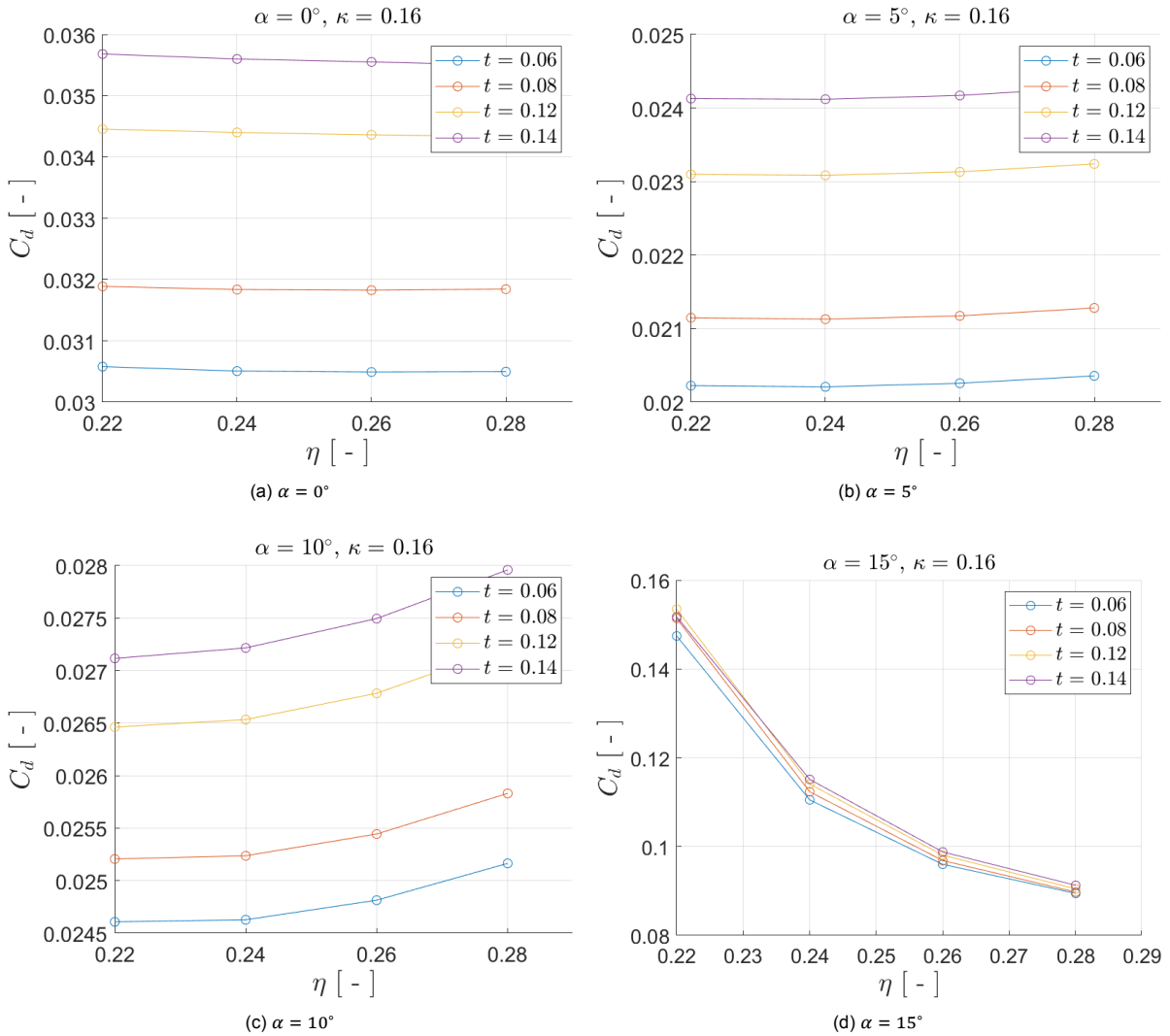


Figure 7.11: C_d versus η given a constant $\kappa = 0.16$ and varying t .

As similarly observed with C_l and C_d , Figure 7.12 shows that the influence of the chordwise position of maximum camber η on C_m increases with the angle-of-attack. At $\alpha = 0^\circ$, 5° and 10° it is clear that C_m decreases with η . This pattern is reversed at $\alpha = 15^\circ$ where there appears to be a change in slope.

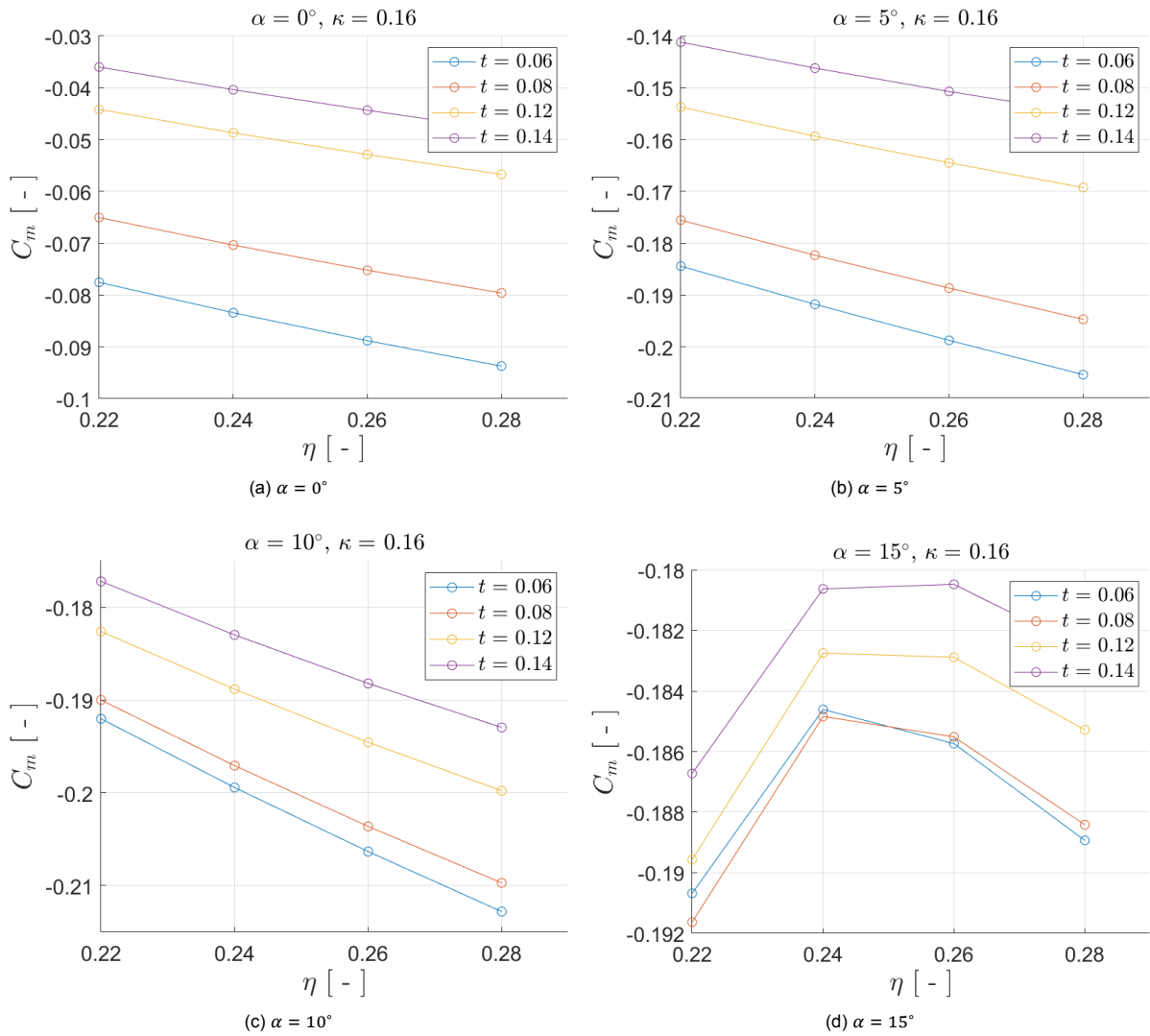


Figure 7.12: C_m versus η given a constant $\kappa = 0.16$ and varying t .

As is evident in Figure 7.13, the chordwise distribution of $c_{f,x}$ on the pressure-side is not discernibly affected by changes in η since the attachment and reattachment points remain effectively fixed in position along the chord. The differences between the given suction-side distributions of $c_{f,x}$ show that an increase in η reduces the wall shear stress over the front of the surface due to lower velocity gradients. However, the contraction of the suction-side peak leads to a slower descent in $c_{f,x}$ towards the trailing edge.

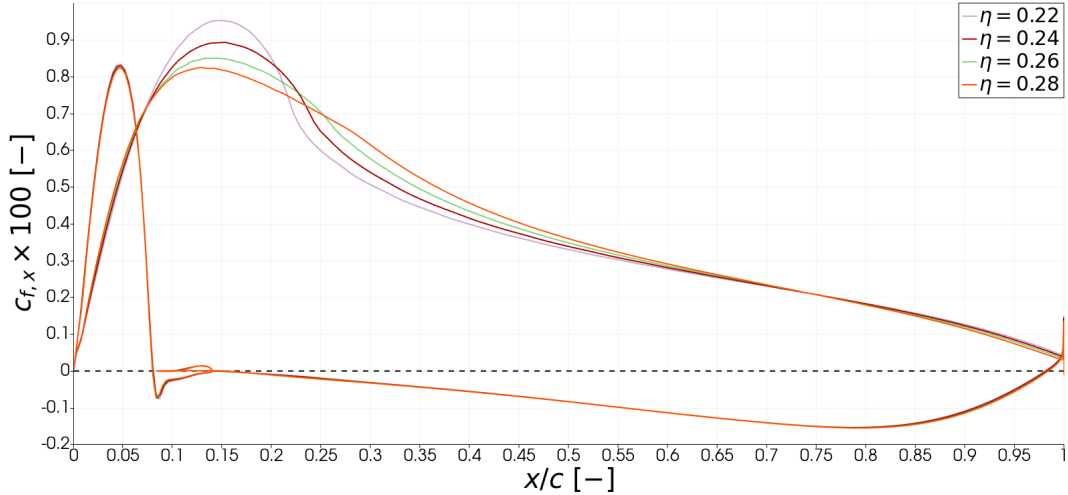


Figure 7.13: Chordwise distributions of $c_{f,x}$ for different values of η given $\alpha = 0^\circ$, $\kappa = 0.16$ and $t = 0.14$.

Proof of delayed flow separation with increasing η for $\alpha = 15^\circ$ is confirmed by the chordwise distributions of $c_{f,x}$ displayed in Figure 7.14. As η increases, $c_{f,x}$ switches from positive to negative on the suction side further towards the trailing edge, implying that the separation point is moved further downstream. What is also evident in Figure 7.14 is the fact that changes in η appear to have little effect on the chordwise positions of the separation and reattachment points of the pressure-side recirculating flow region.

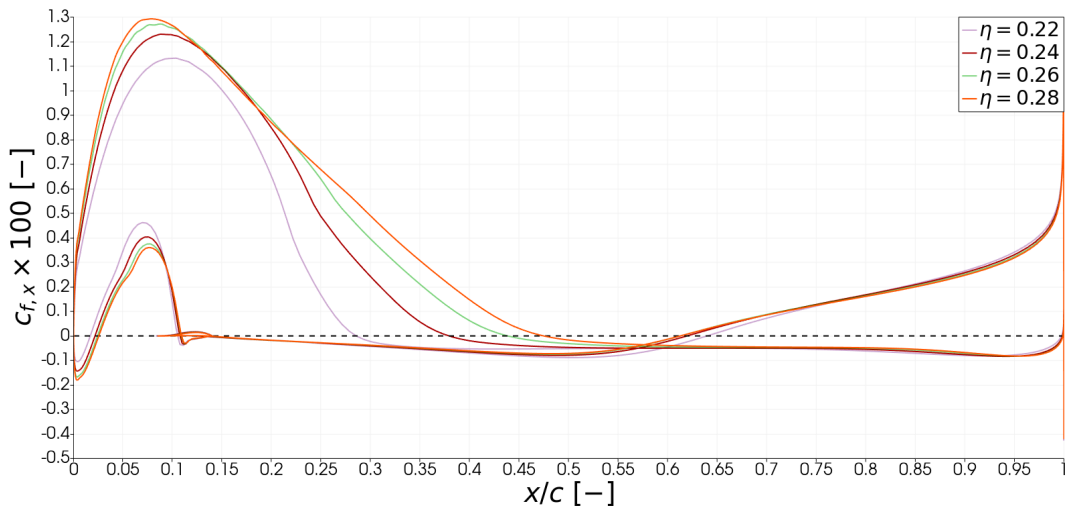


Figure 7.14: Chordwise distributions of $c_{f,x}$ for different values of η given $\alpha = 15^\circ$, $\kappa = 0.16$ and $t = 0.14$.

Whilst the pressure-side pressure distribution remains consistent with increasing η , a reduction in the suction-side peak (i.e. an increase in pressure) is apparent in Figure 7.15. As a result, the adverse pressure gradient becomes less steep, thus bolstering the conditions for attached flow.

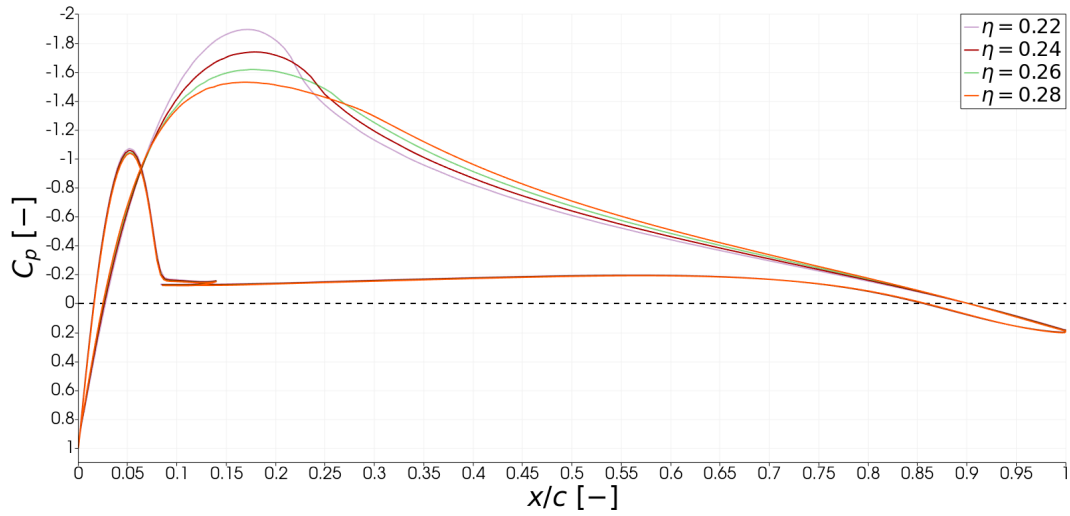


Figure 7.15: Chordwise distributions of C_p for different values of η given $\alpha = 0^\circ$, $\kappa = 0.16$ and $t = 0.14$.

The chordwise distributions of C_p displayed in Figure 7.16 further prove that η has a minor effect on the pressure-side flow. It is evidently clear in Figure 7.16 that increasing η leaves the pressure-side pressure distribution along the chord relatively unchanged, but causes a substantial decrease in pressure on the suction side region near the leading edge given the onset of flow separation when $\alpha = 15^\circ$. This subsequently leads to a larger pressure difference, thus increasing the lift. What is also apparent is that the suction-side adverse pressure gradient becomes less steep with increasing η , thus implying a downstream shift of the separation point and a reduction in the overall size of the reversed flow region.

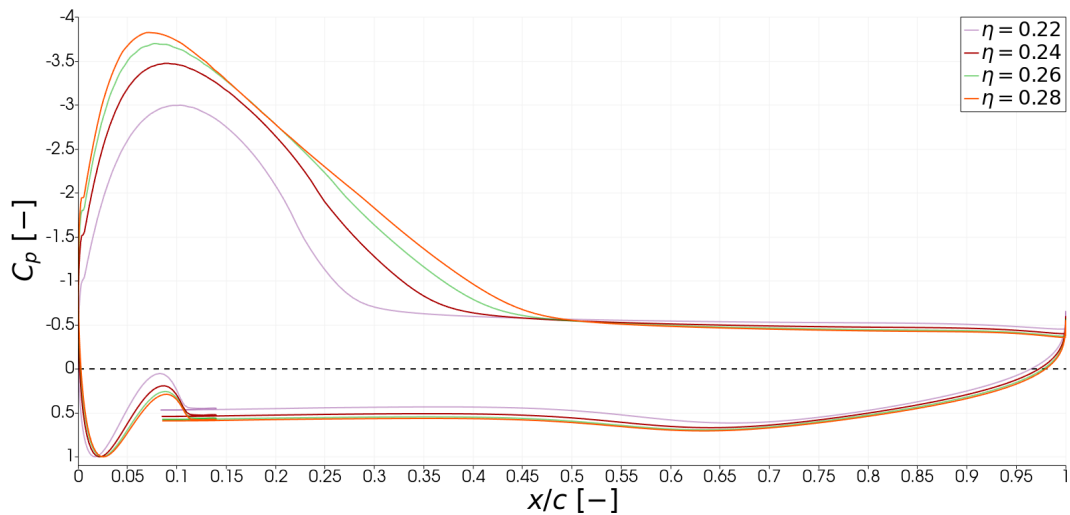


Figure 7.16: Chordwise distributions of C_p for different values of η given $\alpha = 15^\circ$, $\kappa = 0.16$ and $t = 0.14$.

The visualisation of the flow field surrounding the airfoil with shape parameters $\eta = 0.22$, $\kappa = 0.16$ and $t = 0.14$ inclined at $\alpha = 15^\circ$ displayed in Figure 7.17 complements the observation that an increase in angle-of-attack leads to an upstream shift of the pressure-side reattachment point. As a result, the region of recirculating flow on the pressure side reduces in size. But the subsequent increase in lift and decrease in pressure drag is counteracted by the adverse effects of the flow separating from the suction side of the airfoil.

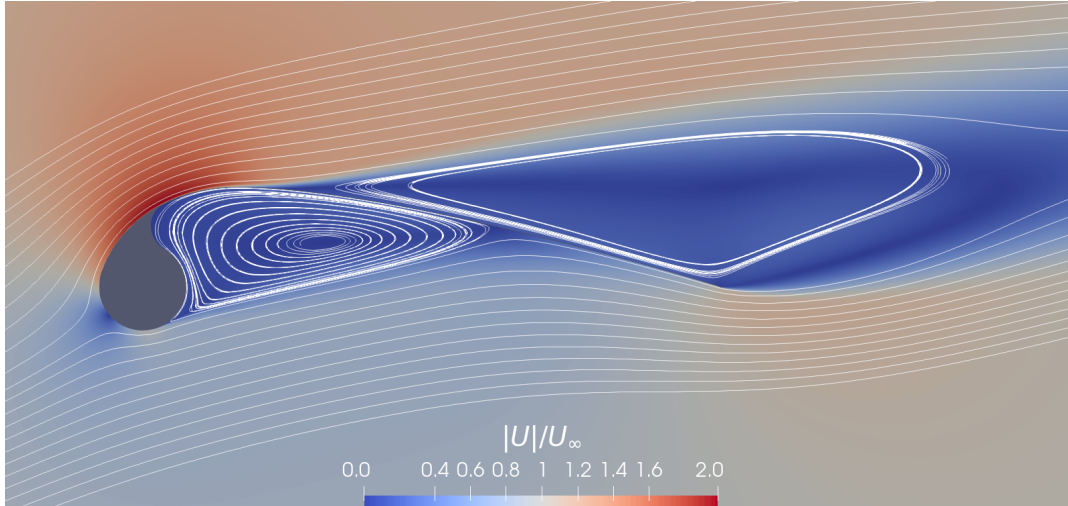
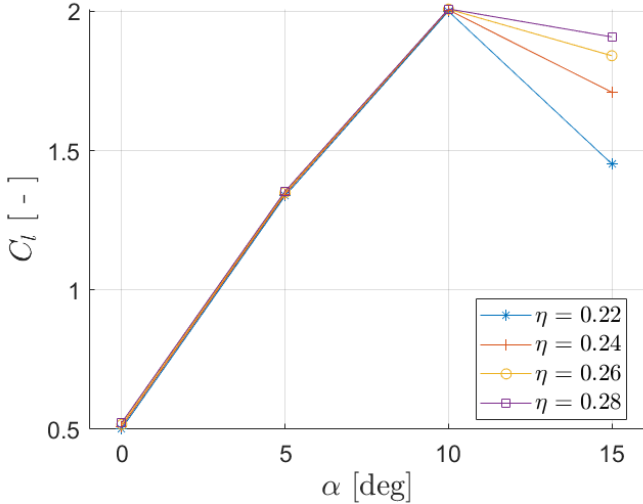


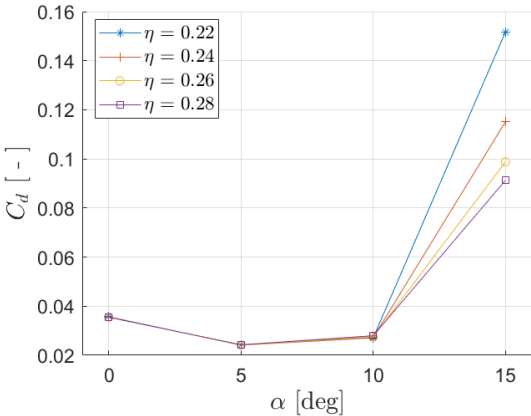
Figure 7.17: Visualisation of normalised flow velocity and streamlines around LE1 wing profile with shape parameters $\eta = 0.22$, $\kappa = 0.16$ and $t = 0.14$ at $\alpha = 15^\circ$.

Given the conditions for suction-side flow separation, increasing η shifts the separation point further downstream, thus reducing the overall size of the reversed flow region emanating from the suction side. This subsequently leads to an increase in lift and decrease in pressure drag due to the flow separating from the suction side. It has already been established that η has an inconsequential effect on the chordwise positions of the pressure-side separation and reattachment points. As such, the drop in lift and increase in pressure drag associated with the pressure-side reversed flow region remain relatively consistent with varying η . Therefore, increasing η given suction-side flow separation leads to an increase in C_l and decrease in C_d as observed in Figure 7.10d and Figure 7.11d respectively. The chordwise distributions of C_p displayed in Figure 7.16 show that front loading on the suction side is alleviated with increasing η , whereas rearward loading downstream $x/c = 0.5$ remains effectively the same. Whilst this has the effect of subsiding the tendency to pitch downwards in the progression from $\eta = 0.22$ to $\eta = 0.24$, given the increase in C_m evident in Figure 7.12d, further increasing η causes the reverse effect as an amplification of the propensity to pitch downwards is revealed by a decreasing C_m . Increasing η leads to larger pressure differences just downstream the quarter-chord point, thus introducing larger pitch-downward loads that overcome the upstream front loading.

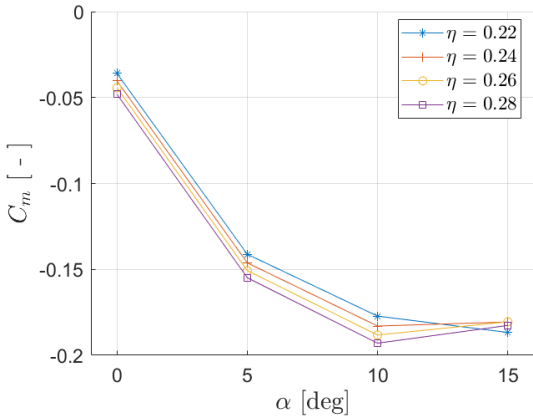
In the case of attached flow over the suction-side, the slight increments in C_l with increasing η evident in Figure 7.10 are attributed to a slight enlargement of the pressure difference resulting from a less steep pressure gradient (see Figure 7.15). Nevertheless, Figure 7.18a affirms that changes in C_l due to η given attached flow are indeed marginal. Increasing η also has the effect of intensifying the front loading on the suction side, thus leading to a stronger pitch-downward bias manifested as decrements in C_m (see Figure 7.12 and Figure 7.18c). The fact that C_d remains effectively constant over the applied range of η for $\alpha = 0^\circ$ and $\alpha = 5^\circ$ as observed in Figure 7.11 implies that the pressure drag resulting from the pressure-side recirculating flow region and the skin-friction drag are practically not affected by η . Figure 7.18b confirms this observation, whilst also showing that the slight increments in C_d due to η given $\alpha = 10^\circ$ evident in Figure 7.11c are of little consequence to the drag curve. Nevertheless, this is the result of a small pocket of suction-side reversed flow near the trailing edge given the combination of $\kappa = 0.16$ and $\alpha = 10^\circ$. Varying η over the applied range does not appear to cause substantial changes in the wetted area, thus constituting a diminished impact on the skin-friction drag.



(a) C_l versus α .



(b) C_d versus α .



(c) C_m versus α .

Figure 7.18: Aerodynamic coefficients versus α for varying values of η given a constant $\kappa = 0.16$ and $t = 0.14$.

7.1.3. Maximum Camber Magnitude κ

Judging from Figure 7.19, C_l increase with the maximum camber magnitude κ at $\alpha = 0^\circ$ and 5° . At $\alpha = 10^\circ$ there is a distinct change in slope and at $\alpha = 15^\circ$ changes are amplified as C_l decreases with κ . Given the occurrence of flow separation from the suction side of the airfoil at $\alpha = 15^\circ$ (see Figure 7.23), it would appear that an increase in κ leads to an earlier onset of flow separation due to the steady decrease in C_l .

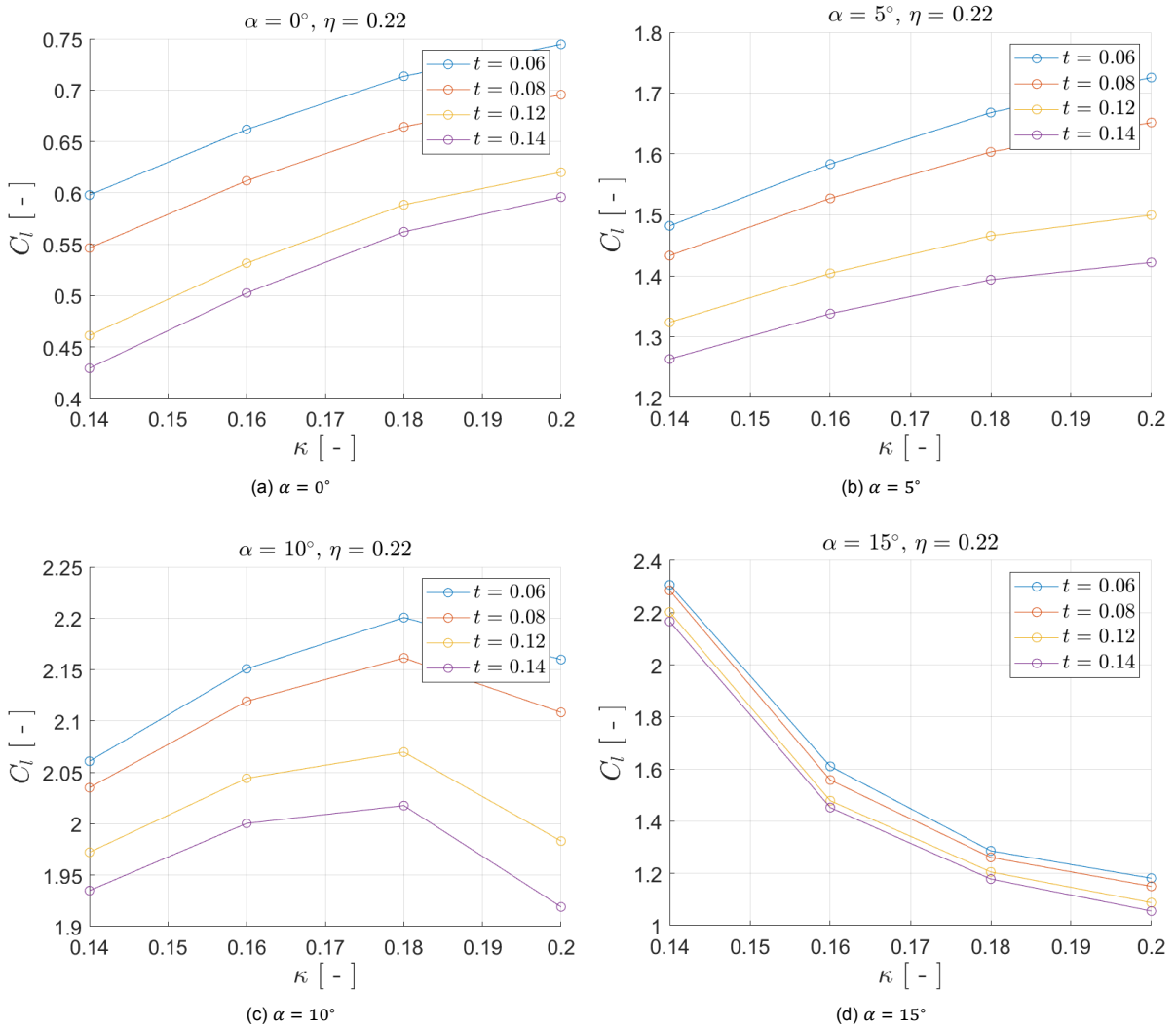


Figure 7.19: C_l versus κ given a constant $\eta = 0.22$ and varying t .

Figure 7.20 shows that in all cases C_d increases with the maximum camber magnitude κ . Variations in C_d are steadily amplified as the angle-of-attack increases. As observed with C_l , an increase in κ leads to an earlier onset of flow separation for $\alpha = 15^\circ$ since C_d increases with κ .

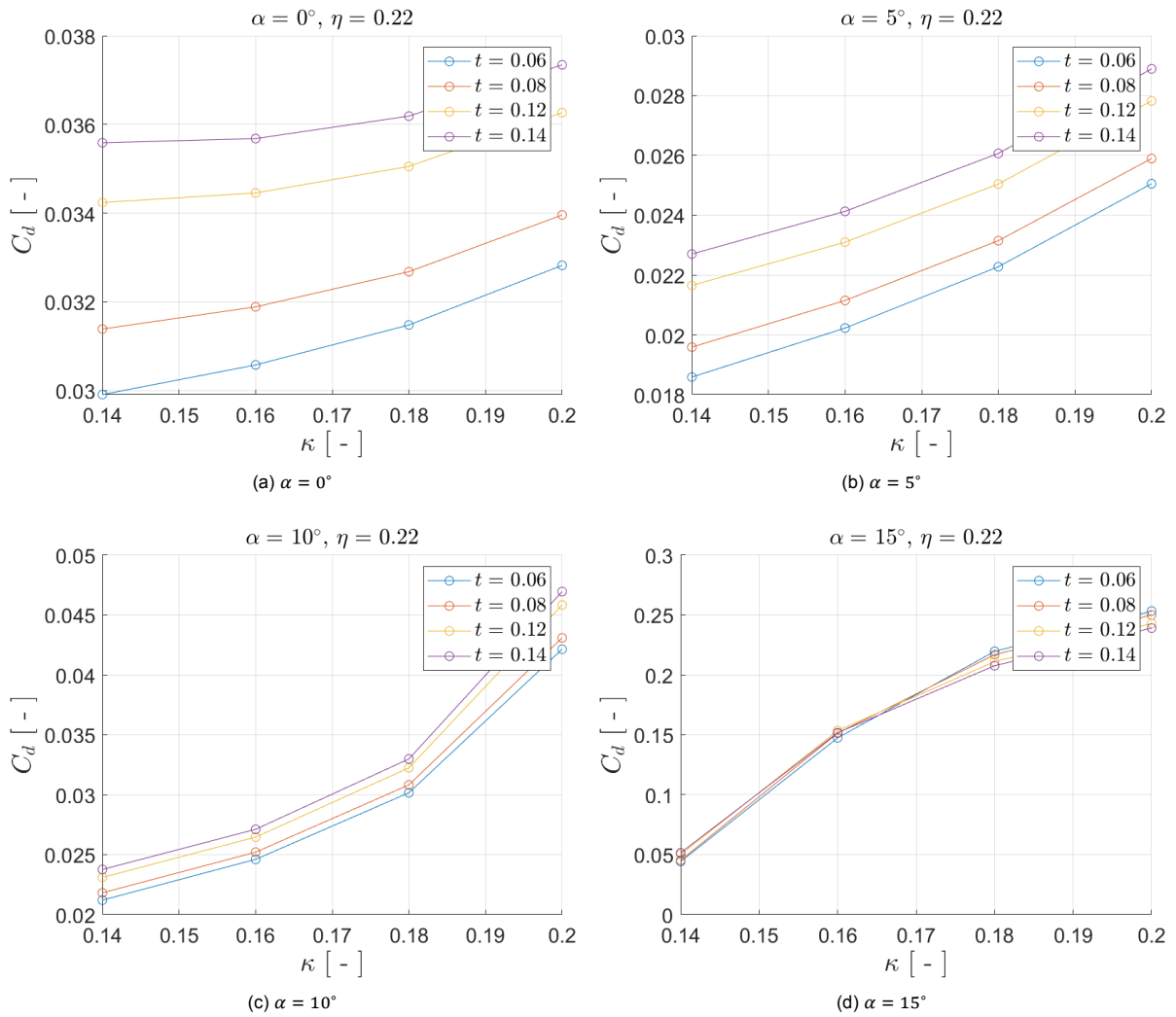


Figure 7.20: C_d versus κ given a constant $\eta = 0.22$ and varying t .

As observed with C_d , Figure 7.21 reveals that the influence of the maximum camber magnitude κ on C_m increases with the angle-of-attack. At $\alpha = 5^\circ$, 10° and 15° it is evident that C_m consistently decreases with κ . At $\alpha = 0^\circ$ there appears to be a change in slope.

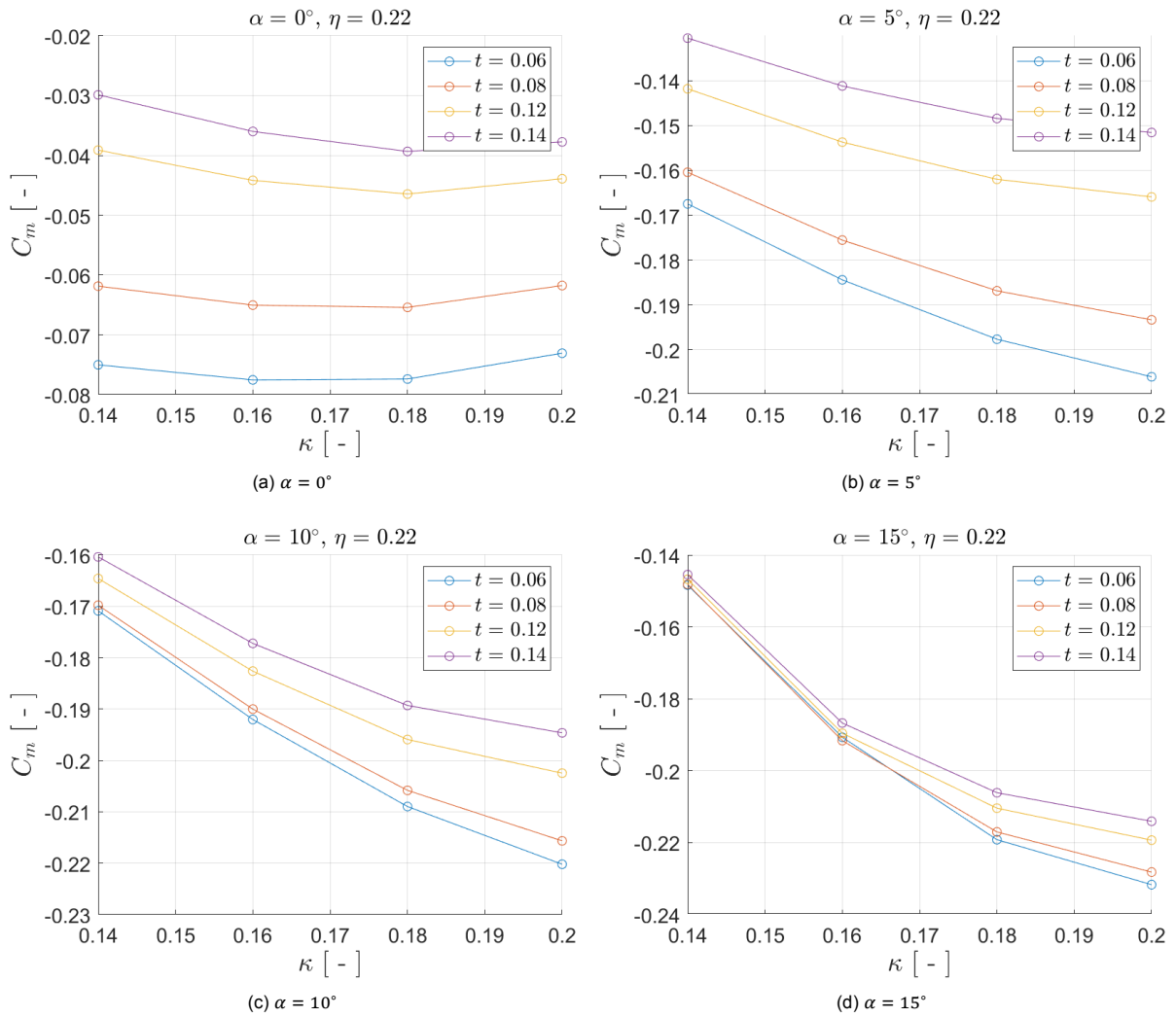


Figure 7.21: C_m versus κ given a constant $\eta = 0.22$ and varying t .

Judging from Figure 7.22, the flow over the suction side given $\alpha = 0^\circ$ remains attached for all displayed chordwise distributions of $c_{f,x}$. However, increasing κ has the effect of diminishing $c_{f,x}$ over the rearward section of the suction-side, thus promoting the onset of mild flow separation. Influences on the pressure-side recirculating flow region are inconsequential given the negligible shifts in separation and reattachment points along the chord. What is also apparent is the ascent of the peak near the leading edge as κ increases due to higher local flow velocities over the suction side, which inevitably causes an increase in skin-friction drag.

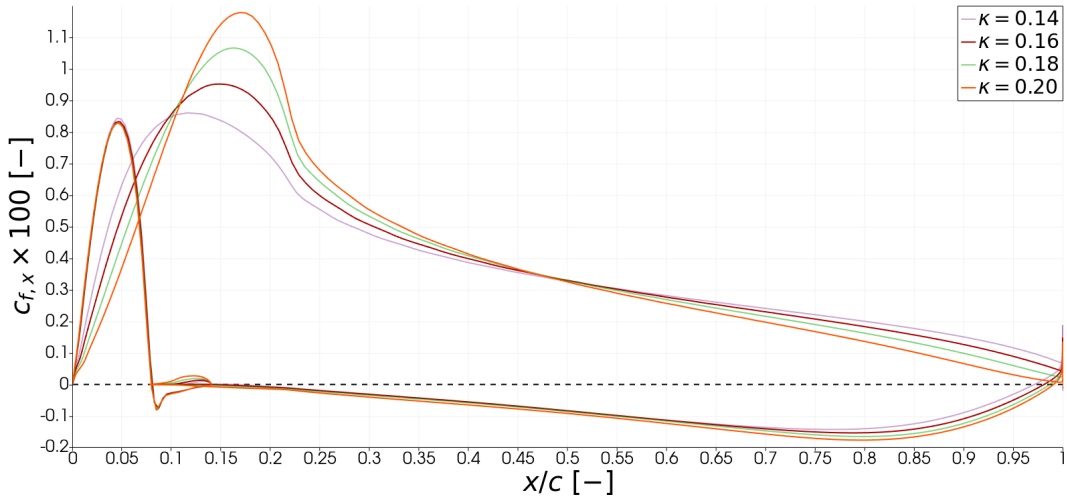


Figure 7.22: Chordwise distributions of $c_{f,x}$ for different values of κ given $\alpha = 0^\circ$, $\eta = 0.22$ and $t = 0.14$.

The chordwise distributions of $c_{f,x}$ displayed in Figure 7.23 prove that an increase in the maximum camber magnitude κ causes an earlier onset of flow separation from the suction side given $\alpha = 15^\circ$. The switch from positive to negative $c_{f,x}$ on the suction side of the airfoil occurs closer towards the leading edge as κ increases, implying the separation point moves further upstream. There also appears to be an increase in the chordwise length of the pressure-side recirculation zone as κ increases since the change in sign of $c_{f,x}$ from negative to positive is delayed with increasing κ , implying that the reattachment point moves further downstream.

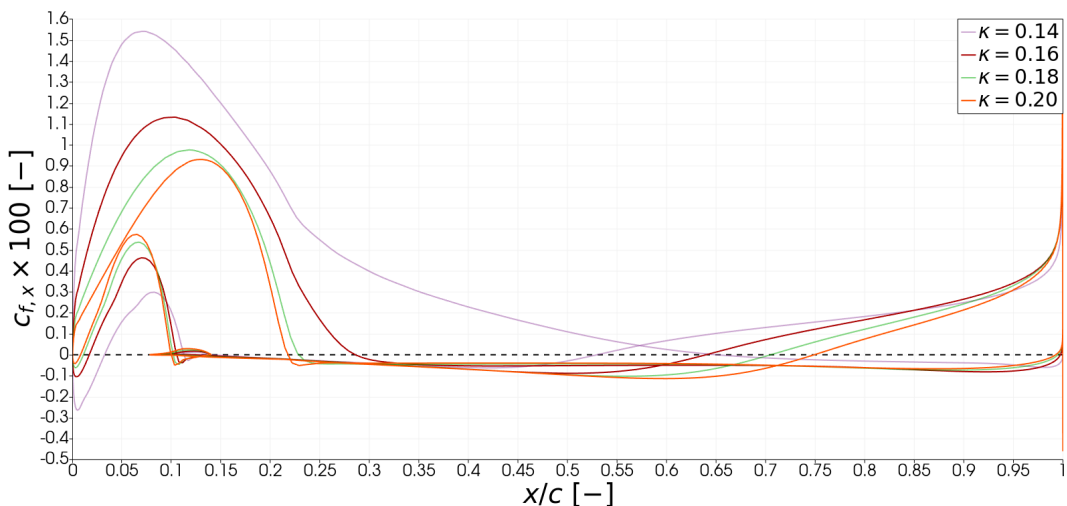


Figure 7.23: Chordwise distributions of $c_{f,x}$ for different values of κ given $\alpha = 15^\circ$, $\eta = 0.22$ and $t = 0.14$.

A drop in suction-side front loading with increasing κ is evident in Figure 7.24 whilst the rearward loading near the trailing edge remains effectively the same. This subsequently amplifies the adverse pressure gradient, but not enough to warrant suction-side flow separation for $\alpha = 0^\circ$. Disparities between the pressure distributions exerted on the two surfaces become more pronounced with increasing κ since changes in C_p across the pressure side are negligible. This has the effect of increasing the lift force.

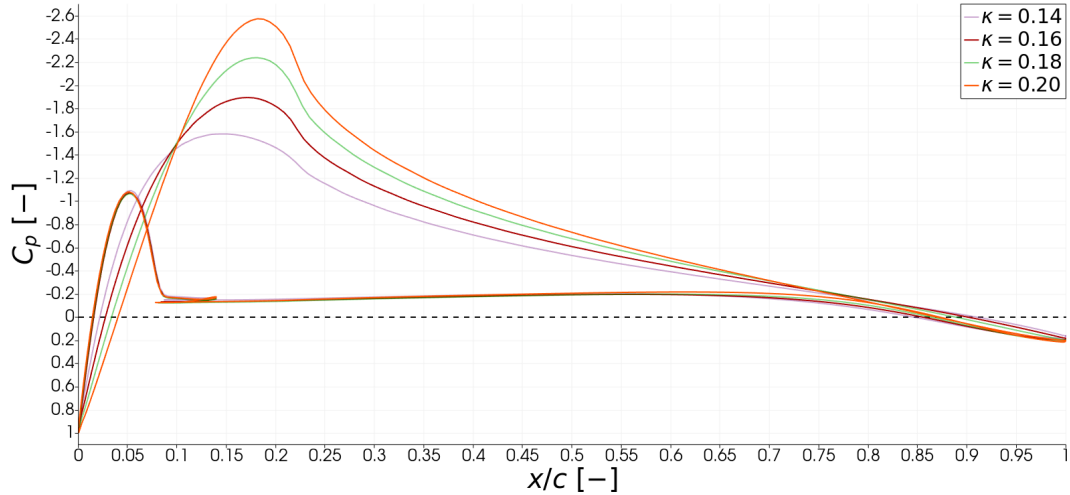


Figure 7.24: Chordwise distributions of C_p for different values of κ given $\alpha = 0^\circ$, $\eta = 0.22$ and $t = 0.14$.

Adverse pressure gradients on the suction side become more steep and move further upstream in Figure 7.25 as κ increases, which is consistent with the fact that an earlier onset of suction-side flow separation occurs with increasing κ for $\alpha = 15^\circ$. What is also evident is the substantial decrease in pressure difference that is a result of intensified front loading on the suction side and relieved loading on the pressure side as κ increases.

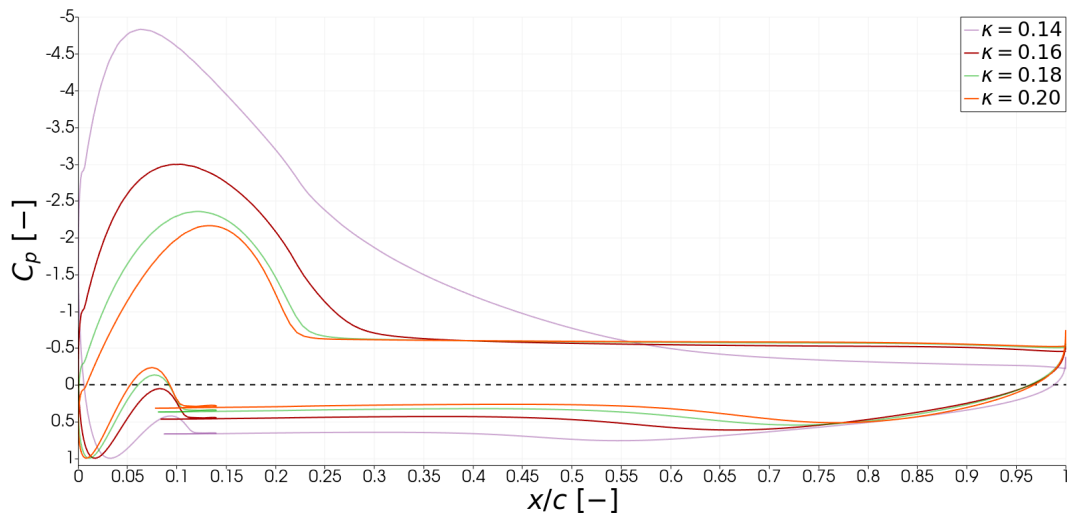


Figure 7.25: Chordwise distributions of C_p for different values of κ given $\alpha = 15^\circ$, $\eta = 0.22$ and $t = 0.14$.

The flow field around the airfoil with shape parameters $\eta = 0.22$, $\kappa = 0.20$ and $t = 0.14$ at $\alpha = 15^\circ$ has been visualised in Figure 7.26. Comparing Figure 7.17 and Figure 7.26 reveals that both the region of recirculating flow on the pressure side of the airfoil and the area encompassed by the separated flow emanating from the suction side increase in size with κ .

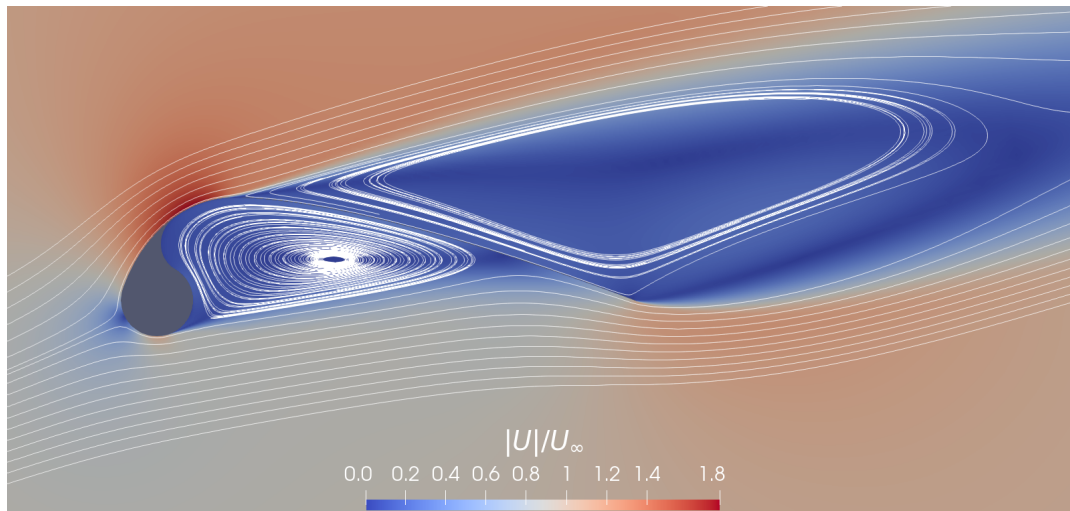
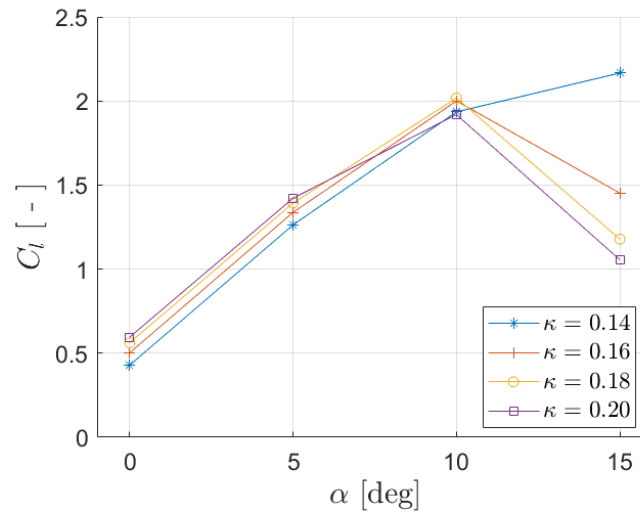
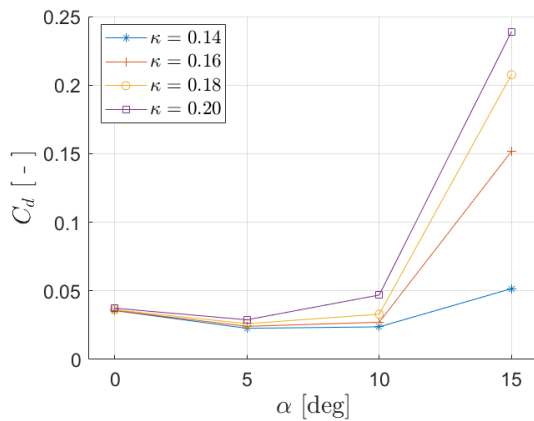
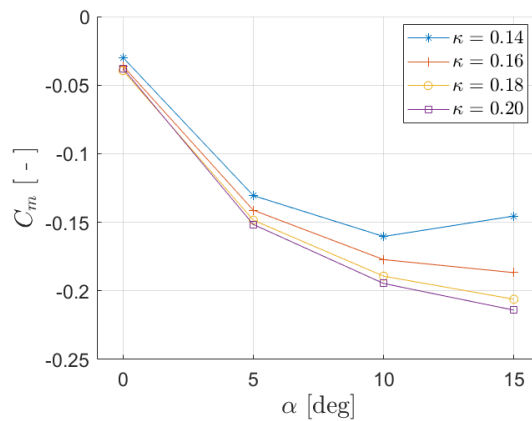


Figure 7.26: Visualisation of normalised flow velocity and streamlines around LEI wing profile with shape parameters $\eta = 0.22$, $\kappa = 0.20$ and $t = 0.14$ at $\alpha = 15^\circ$.

Since both the pressure-side and suction-side regions of reversed flow increase in size with κ , the combined pressure drag resulting from both regions also increases whilst the lift decreases. The added effects explain the substantial decline in C_l and surge in C_d with increasing κ as observed in Figure 7.19d and Figure 7.20d respectively. The drop in C_m with increasing κ evident in Figure 7.21d is attributed to the amplification of suction-side front loading and relieved loading on the pressure side. This has the effect of diminishing the pitch-upward loads upstream the quarter-chord point and subsequently exacerbating the pitch-downward trend.

The substantial effect κ has on the flow stability is further emphasised by Figure 7.27. In the case of $\alpha = 0^\circ$ and $\alpha = 5^\circ$, the flow over the suction side remains attached and an increase in κ causes a mild gain in C_l as evidenced by Figure 7.19a and Figure 7.19b respectively (as well as Figure 7.27a). But for $\alpha = 10^\circ$, the rise in C_l with κ becomes progressively more subdued until eventually a decrease in C_l moving from $\kappa = 0.18$ to $\kappa = 0.20$ is observed in both Figure 7.19c and Figure 7.27a. As is evident in Figure 7.22, the flow is more inclined to separate from the suction side given a larger value of κ , a tendency which is amplified for high angles-of-attack. This is evidently the case for the applied range of κ given $\alpha = 10^\circ$, whereby increasing κ further expands the region of separated flow emanating from the suction to the point where the loss in lift causes a reduction in C_l . The subsequent increase in pressure drag due to the suction-side separated flow is evident in both Figure 7.20c and Figure 7.27b given the larger differences in C_d between the curves as the angle-of-attack increases. Similar to the results of $\alpha = 15^\circ$, increasing κ given $\alpha = 10^\circ$ also shifts the pressure-side reattachment point further downstream whilst the separation point remains at approximately the same chordwise location. This has the effect of increasing the total pressure drag and lowering the lift, thus adding to the adverse effects of the suction-side flow reversal. Intuitively, the area enclosed by the canopy is expanded upon increasing κ , thus leading to a larger region of recirculating flow on the pressure side. This appears to have a negligible effect on the pressure-side flow for low angle-of-attack cases (see Figure 7.22 and Figure 7.24). Furthermore, increasing κ expands the wetted area, thus leading to a higher skin-friction drag contribution to C_d .

Similar to the C_d curves displayed in Figure 7.27b, differences in C_m between the curves displayed in Figure 7.27c are more distinct with an increasing angle-of-attack. Judging from Figure 7.20a and Figure 7.27c, the rise in suction-side front loading with increasing κ roughly balances out the rise in rearward loading downstream the quarter chord point as variations in C_m are minimal compared to larger angles-of-attack. Regarding the $\alpha = 5^\circ$ and $\alpha = 10^\circ$ cases presented in Figure 7.21b and Figure 7.21c respectively, the distributed load imbalance with increasing κ exacerbates the tendency to pitch downwards.

(a) C_l versus α .(b) C_d versus α .(c) C_m versus α .Figure 7.27: Aerodynamic coefficients versus α for varying values of κ given a constant $\eta = 0.22$ and $t = 0.14$.

7.2. Comparisons with Literature

The numerical study of Demkowicz [16] examined the flow field around a 3D LEI wing using the $k - \omega$ SST turbulence model both with and without the $\gamma - \widetilde{Re}_{\theta t}$ transition model. The findings of cases in which the transition model is utilised show that a laminar separation bubble forms near the leading edge of the airfoil for low Reynolds numbers (in this case $Re = 5 \times 10^5$). Given the same flow conditions, the separation bubble does not manifest without the activation of the $\gamma - \widetilde{Re}_{\theta t}$ transition model. However, even with the $\gamma - \widetilde{Re}_{\theta t}$ transition model activated, a laminar separation bubble does not form near the leading edge from $Re = 3 \times 10^6$ onward since laminar-to-turbulent transition occurs earlier. The 2D numerical results of Folkersma et al. [21] attained from $k - \omega$ SST simulations of the flow field around a LEI wing profile with the $\gamma - \widetilde{Re}_{\theta t}$ activated show that a laminar separation bubble does not form near the leading edge from $Re = 5 \times 10^6$ onward. The absences of laminar separation bubbles in the contour plots of Figure 7.8, Figure 7.17 and Figure 7.26 are consistent with the findings of Demkowicz [16] and Folkersma et al. [21] given the omission of transition modelling from the simulations conducted for the purposes of this study. Simulating the same flow fields with integrated turbulence and transitions models would likely not lead to the formation of laminar separation bubbles near the leading edge of a parameterised LEI wing profile given the same flow conditions since the applied Reynolds number of $Re = 5 \times 10^6$ meets the threshold established by Folkersma et al. [21] for 2D profiles.

Remaining on the subject of reversed flow, a key finding of the work of Folkersma et al. [21] is the fact that the region of recirculating flow on the pressure side of a LEI wing profile immersed in a flow field decreases in size with the angle-of-attack, leading to an increase in lift and decrease in pressure drag. One can come to the same conclusion when comparing Figure 7.8 to Figure 7.17 and Figure 7.26. It is evidently clear in Figure 7.8 that for $\alpha = 0^\circ$ the recirculating flow region extends over the entire area enclosed by the pressure side of the canopy and leading-edge tube. In contrast, both Figure 7.17 and Figure 7.26 show a diminished region of recirculating flow for $\alpha = 15^\circ$. But the subsequent increase in lift and decrease in pressure drag is counteracted by the adverse effects of flow separation on the suction side of the airfoil.

The effects of the aforementioned viscous flow phenomena emerge in the computed lift and drag coefficients. Therefore, comparisons have been made with the lift and drag curves of Folkersma et al. [21] in Figure 7.28. The displayed reference results have been attained from fully turbulent (i.e. no transition modelling) $k - \omega$ SST simulations on a LEI wing profile given $Re = 5 \times 10^6$.

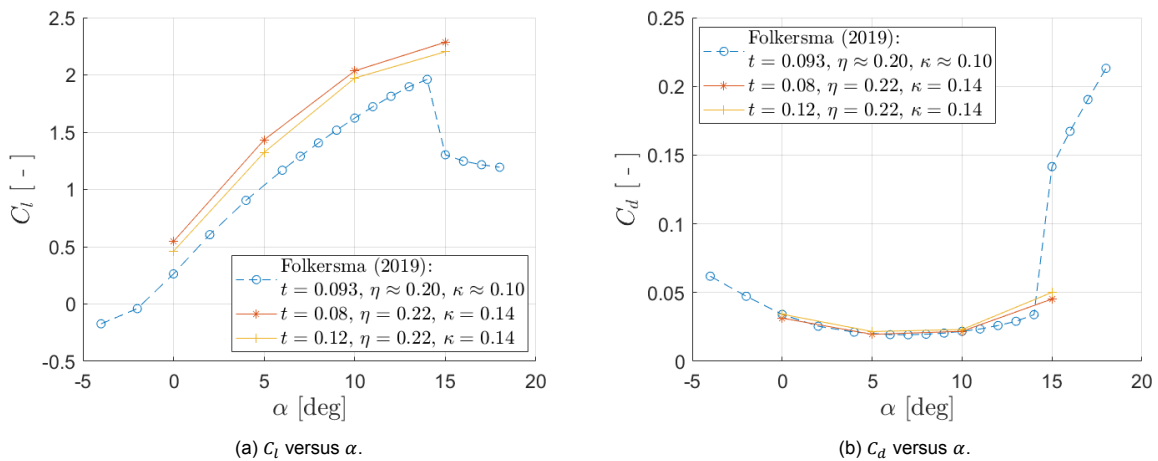


Figure 7.28: Aerodynamic coefficients computed in this study (solid lines) compared to numerical results from the work of Folkersma et al. [21] (dashed lines). The shape parameters κ and η of the airfoil examined in the study of Folkersma et al. [21] have been estimated according to the definitions used in this study (see Section 2.1.3).

Despite differences in shape parameters, the drag coefficients computed for the purposes of this study appear to closely match the drag curve relation established by Folkersma et al. [21] given the same flow conditions. An exception to this trend is observed for $\alpha = 15^\circ$ as the airfoil examined by Folkersma et al. [21] stalls earlier given the surge in C_d and drop in C_l . Discernible differences in C_l are evident in Figure 7.28a given the same free-stream conditions. This outcome is consistent with the observation that an airfoil with a larger maximum camber magnitude κ generates a higher lift force given the same free-stream conditions and attached flow over the suction side. The earlier onset of stall observed with regard to the simulation results of Folkersma et al. [21] for a lower value of κ is not consistent with the findings of this study. This is likely due to differences in the shape of the canopy resulting from the application of different systems of interpolation. The rearward section of the membrane canopy of the airfoil examined by Folkersma et al. [21] is effectively approximated as a straight line extending from the trailing edge to just downstream the maximum camber point where the line starts to curve and descend towards the leading edge. This evidently has the effect of reducing the critical angle-of-attack compared to the similar parameterised airfoils of this study which are characterised by more curvature.

The method of parameterisation applied by Breukels [7] has led to similarly curved airfoils. The contour plot displayed in Figure 7.29 from the work of Breukels [7] has been used to estimate the maximum camber magnitude κ of the displayed airfoil according to the definition used in this study (see Section 2.1.3). According to the definition of “airfoil camber” used by Breukels [7], it has a camber of 8% (assumed to be relative to the chord length). But according to the definition of “maximum camber magnitude” used in this study, $\kappa \approx 0.17$ for the airfoil displayed in Figure 7.29. The “airfoil thickness” of the LEI wing profile displayed in Figure 7.29 has not been explicitly stated in the work of Breukels [7]. However, based on the profile displayed in Figure 2.2, which is claimed to have an “airfoil thickness” of 20% (also assumed relative to the chord length), it would appear Breukels [7] uses the same definition of “airfoil thickness” as has been used in this study (see Section 2.1.3).

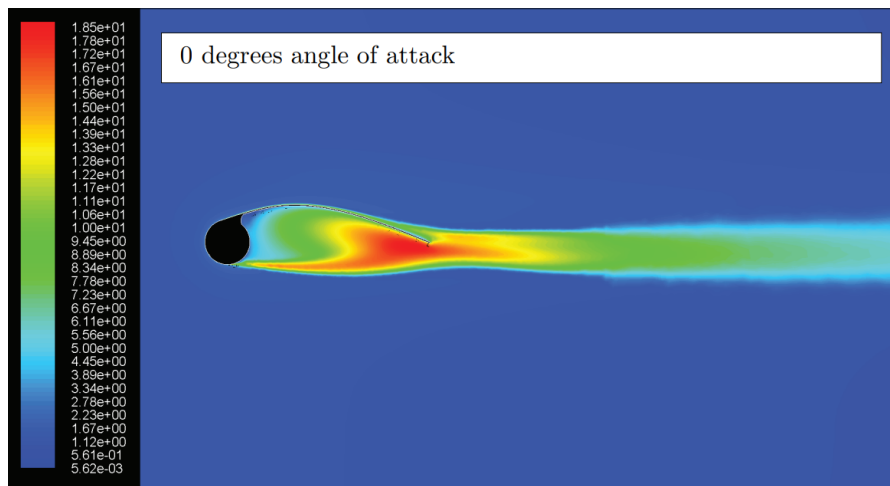
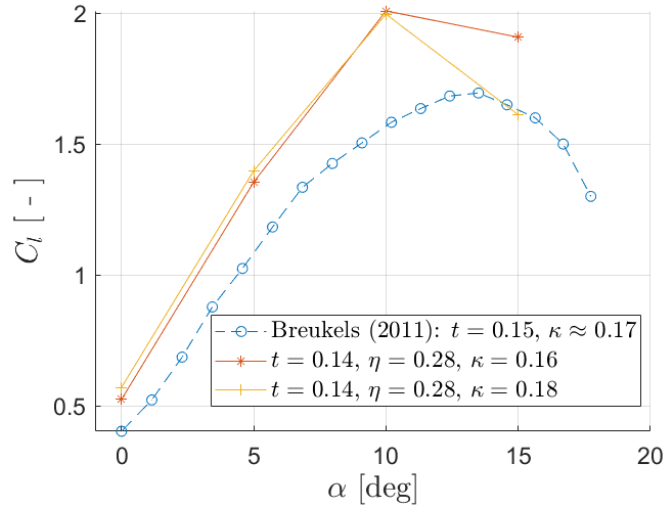
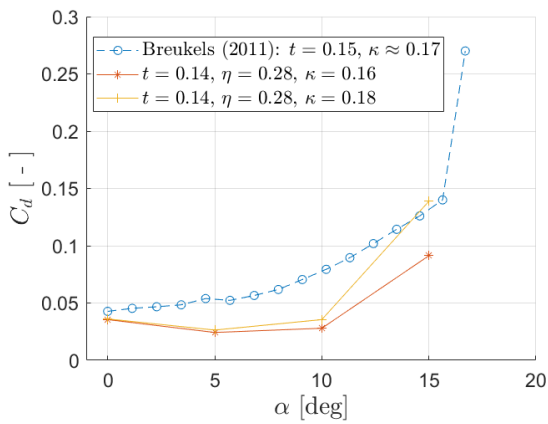


Figure 7.29: Turbulence intensity contour plot from the work of Breukels [7]. The displayed LEI wing profile is inclined at $\alpha = 0^\circ$ and has a camber of 8% according to the definition of “airfoil camber” used by Breukels [7]. According to the definition of “maximum camber magnitude” used in this study, $\kappa \approx 0.17$ for the displayed airfoil.

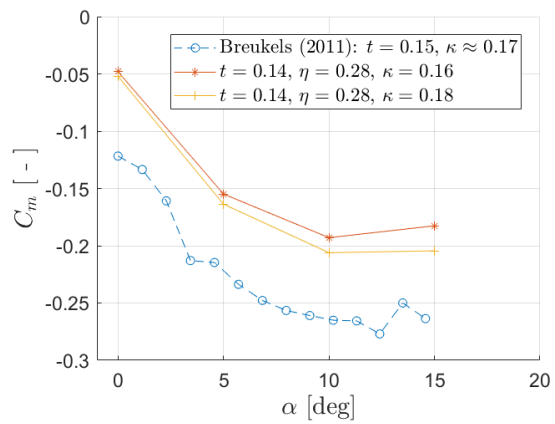
As such, it is assumed the same definition of “airfoil thickness” has been used and that a camber of 8% in the work of Breukels [7] is equivalent to a maximum camber magnitude of $\kappa \approx 0.17$ as per this study. The calculated aerodynamic coefficients of an airfoil inclined at a wide range of angles-of-attack with shape parameters $t = 0.15$ and $\kappa \approx 0.17$ from the results of Breukels [7] have been compared to the numerical results attained in this study from parameterised LEI wing profiles with similar shape parameters in Figure 7.30. Note that Breukels [7] kept the chordwise position of maximum camber constant for all simulated airfoils [8].



(a) C_l versus α .



(b) C_d versus α .

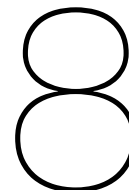


(c) C_m versus α .

Figure 7.30: Aerodynamic coefficients computed in this study (solid lines) compared to numerical results from the work of Breukels [7] (dashed lines). Note that the maximum camber magnitude κ of the reference has been estimated according to the definition used in this study (see Section 2.1.3).

The numerical results from the work of Breukels [7] presented in Figure 7.30 have been attained by means of the $k - \omega$ SST turbulence model whilst also “incorporating transitional flows” [7]. This quote is interpreted as an allusion to the inclusion of transition modelling, although exactly which transition model has been implemented has not been explicitly stated. Another critical missing piece of information is the Reynolds number or flow velocity used to simulate the flow fields from which the aerodynamic coefficients have been calculated. The Reynolds number has a substantial effect on the boundary layer thickness and the size of the recirculating flow region on the pressure side of the airfoil, as established by Folkersma et al. [21], which in turn affects the aerodynamic coefficients.

Compared to the reference lift and drag curves, the values of C_l and C_d from the given examples of this study are generally greater and smaller respectively given the same angle-of-attack. Since the airfoil from the reference study has a value of κ between the two given examples and a similarly curved canopy, a close match between the reference and example curves would be expected if the free-stream conditions were the same. This is evidently not the case and is indicative of different free-stream conditions.



Regression Analysis

An elucidation of the general principles constituting regression analysis is required for the purposes of this work. This chapter commences with a description of the method of least squares in Section 8.1, followed by an explanation of statistical quality indicators in Section 8.2 used to assess the regression model. The final development of the revised aerodynamic load model has been presented in Section 8.3.

8.1. Method of Least Squares

Whilst the method for solving least squares problems described in Section 8.1.1 gives a more intuitive understanding of the method of least squares, the actual method applied in this study is explained in Section 8.1.2.

8.1.1. Normal Equations

At its core, regression analysis serves as a means to model a relationship between a response variable Y and a set of predictor variables $X_i = (X_1, X_2, \dots, X_m)$ in the following general form:

$$Y = f(X_i, \vec{\beta}) + \epsilon \quad (8.1)$$

The model function $f(X_i, \vec{\beta})$ is defined by the predictor variables X_i and the unknown parameters (i.e. constant coefficients) in vector $\vec{\beta}$, which are to be estimated from the data. The random error ϵ resulting from the regression analysis is usually assumed to be independent, with a zero mean normal distribution [18]. Although the data fitted model may be non-linear, as is the intended outcome of polynomial regression, the statistical estimation itself is linear in the parameters of vector $\vec{\beta}$.

Therefore, it is possible to express the model as a system of linear equations given multiple observations of the response variable Y :

$$\vec{Y} = \mathbf{X}\vec{\beta} + \vec{\epsilon} \quad (8.2)$$

Equation (8.2) expresses the vector of observations \vec{Y} in terms of the matrix of predictor variables (i.e. design matrix) \mathbf{X} , the vector of parameters to be estimated $\vec{\beta}$ and the error vector $\vec{\epsilon}$. A crucial note is the fact that $\vec{\beta}$ and $\vec{\epsilon}$ are unknown. Whilst ϵ changes with every observation of Y , the parameters of vector

$\vec{\beta}$ remain fixed and are estimated using a sufficiently large set of observations. Vector $\hat{\beta}$ comprises the estimated parameters whereby the values of the response variable Y are predicted for a given X_i by means of the matrix relation $\hat{Y} = \mathbf{X}\hat{\beta}$ (the symbol $\hat{\cdot}$ denotes a vector of predicted or estimated values). The method of least squares, whereby the sum of squared errors $\vec{\epsilon}^T \vec{\epsilon}$ is minimised, is employed for the purpose of estimating the parameters.

The calculation of the least squares estimates starts with the following formulation of the sum of squared errors:

$$\vec{\epsilon}^T \vec{\epsilon} = (\vec{Y} - \mathbf{X}\vec{\beta})^T (\vec{Y} - \mathbf{X}\vec{\beta}) \quad (8.3)$$

Differentiating Equation (8.3) with respect to $\vec{\beta}$, equating the outcome to zero and subsequently rearranging the resultant matrix equation with $\vec{\beta}$ replaced by $\hat{\beta}$ leads to the so-called *normal equations*:

$$(\mathbf{X}^T \mathbf{X}) \hat{\beta} = \mathbf{X}^T \vec{Y} \quad (8.4)$$

The inverse of $\mathbf{X}^T \mathbf{X}$ exists only if it is non-singular, a necessary condition to permit the rearrangement of Equation (8.4) such that the least squares estimates $\hat{\beta}$ can be calculated:

$$\hat{\beta} = (\mathbf{X}^T \mathbf{X})^{-1} \mathbf{X}^T \vec{Y} \quad (8.5)$$

If the inverse of $\mathbf{X}^T \mathbf{X}$ exists, the least squares estimates $\hat{\beta}$ are subsequently used to calculate the response variable estimates \hat{Y} .

8.1.2. QR Decomposition

Although the implementation of the normal equations is more straightforward in a least squares context, the regression analysis is subsequently more prone to numerical instabilities. An alternative and more numerically stable approach would be to decompose the $m \times n$ design matrix \mathbf{X} (given $m > n$) as the product of an $m \times m$ orthogonal matrix \mathbf{Q} and an $m \times n$ upper triangular matrix \mathbf{R} , a process referred to as *QR decomposition* or *QR factorisation* [23]. The design matrix \mathbf{X} has more rows than columns given the over-determined linear system of equations.

Furthermore, the elements of the bottom $m - n$ rows of matrix \mathbf{R} are all zero (and contained within the zero matrix $\mathbf{0}$), thus permitting the following matrix partition:

$$\mathbf{X} = \mathbf{QR} = [\mathbf{Q}_1 \quad \mathbf{Q}_2] \begin{bmatrix} \mathbf{R}_1 \\ \mathbf{0} \end{bmatrix} = \mathbf{Q}_1 \mathbf{R}_1$$

Referred to as *thin QR factorisation*, the outcome of this adaptation is a design matrix \mathbf{X} defined as the product of an $m \times n$ semi-orthogonal matrix \mathbf{Q}_1 and an invertible $n \times n$ upper triangular matrix \mathbf{R}_1 [23]. The columns of matrix \mathbf{Q}_1 are orthonormal vectors since the number of rows exceeds the number of columns ($m > n$), from which can be deduced that $\mathbf{Q}_1^T \mathbf{Q}_1 = \mathbf{I}_n$ where \mathbf{I}_n denotes the $n \times n$ identity matrix. The reader should be conscious of the fact that $\mathbf{Q}_1^T \mathbf{Q}_1$ and $\mathbf{Q}_1 \mathbf{Q}_1^T$ are not equivalent since \mathbf{Q}_1 is not a square matrix.

Plugging $\mathbf{X} = \mathbf{Q}_1 \mathbf{R}_1$ into Equation (8.4) transforms the normal equations to the upper triangular system, leading to the unique least squares solution after rearrangement:

$$\hat{\beta} = \mathbf{R}_1^{-1} \mathbf{Q}_1^T \vec{Y} \quad (8.6)$$

In the case of *pivoted QR decomposition*, the design matrix \mathbf{X} is column-permuted by means of the permutation matrix \mathbf{P} such that the absolute values of the diagonal elements of matrix \mathbf{R} decrease in

magnitude towards the last column:

$$\mathbf{XP} = \mathbf{QR} \quad (8.7)$$

For further insight into QR decomposition the reader is referred to Golub and van Loan [23].

8.2. Statistical Quality Indicators

Any deviation between an observation of Y and its predicted value is stored in the residual vector $\vec{e} = \vec{Y} - \hat{Y}$. Intuitively, small residuals are indicative of a suitable model that accurately fits the data. The standard measure of this particular statistical quality is the *residual sum of squares* RSS, which equates to $\vec{e}^T \vec{e}$ when expressed in the same format as Equation (8.3).

Similar statistical quality assessment quantities are the *explained sum of squares* ESS and the *total sum of squares* TSS. The former quantity is defined as the sum of all squared discrepancies between the predicted values of the response variable Y and the overall mean \bar{y} of the response vector \vec{Y} , whereas the latter is the sum of all squared differences between the actual observations of the response variable Y and \bar{y} .

The construction of vector \bar{Y} , with the sample mean \bar{y} as each element (i.e. $\bar{Y} = (\bar{y}, \bar{y}, \dots, \bar{y})$) and given the same dimension as \vec{Y} and \hat{Y} , permits the expression of ESS and TSS in matrix form (NB the mean of the estimated quantities is equivalent to the mean of the observations Y):

$$\text{RSS} = (\vec{Y} - \hat{Y})^T (\vec{Y} - \hat{Y}) = \vec{e}^T \vec{e} \quad (8.8a)$$

$$\text{ESS} = (\hat{Y} - \bar{Y})^T (\hat{Y} - \bar{Y}) \quad (8.8b)$$

$$\text{TSS} = (\vec{Y} - \bar{Y})^T (\vec{Y} - \bar{Y}) = \text{RSS} + \text{ESS} \quad (8.8c)$$

Intuitively, ESS is a measure of the variations of the model estimated quantities, whereas TSS indicates the extent to which the actual observed quantities vary. The relation $\text{TSS} = \text{RSS} + \text{ESS}$ shows that variations in the observations of Y about the mean are partially a result of the regression analysis itself and partially due to the fact that the actual observations are not an exact fit of the model. If the latter case were to be true instead, where each observation of Y is estimated exactly by the model, then $\text{RSS} = 0$. Though ideal, this is an improbable scenario and instead the focus lies in minimising the value of RSS relative to TSS.

Therefore, the following expression is used to assess the quality of a regression analysis:

$$R^2 = \frac{\text{ESS}}{\text{TSS}} = 1 - \frac{\text{RSS}}{\text{TSS}} \quad (8.9)$$

The statistical quantity R^2 , which ranges between 0 and 1, gives the "*proportion of total variation about the mean explained by the regression*" [18]. The regression analysis should lead to a value of R^2 as close as possible to unity as this implies that most of the total variation in the data is explained by the fitted model.

Another prominent quality indicator is the *root-mean-squared error* (RMSE), which is the square root of the mean of the RSS:

$$\text{RMSE} = \sqrt{\frac{\text{RSS}}{n}} = \sqrt{\frac{\vec{e}^T \vec{e}}{n}} \quad (8.10)$$

Contrary to R^2 , the RMSE is to be minimised since a low value is indicative of better accuracy. The RMSE is either positive or equal to 0, whereby the latter case constitutes a perfect data fit and is a rare occurrence in practice.

Although R^2 and the RMSE give insight into the overall quality of a fitted model, by no means are these statistical quantities the sole measures by which a regression analysis should be scrutinised. Suitable values of R^2 and the RMSE are also attained in cases of over-fitting whereby the fitted model shows poor overall performance as an estimator. Large variances of the estimated parameters are evidence of over-fitting, thus showing a considerable dependence on the data used for the regression analysis.

8.3. Polynomial Equations of Aerodynamic Coefficients

The ultimate goal of the regression analysis is to devise polynomial equations expressing the aerodynamic coefficients in terms of the angle-of-attack α and the non-dimensional airfoil shape parameters η , κ and t :

$$C_l = f(\alpha, \eta, \kappa, t)$$

$$C_d = g(\alpha, \eta, \kappa, t)$$

$$C_m = h(\alpha, \eta, \kappa, t)$$

Assessing the fidelity and accuracy of the polynomial fits is made possible by the established statistical quality indicators described in Section 8.2. Finding suitable approximating equations is an iterative process in which one gauges the effects of omitting certain polynomial terms (e.g. $\alpha^2\eta\kappa$, which is a 4th degree term). The omission of terms should partly be based on the desired degree of the approximating polynomial since it is equivalent to the highest observed degree in the terms. For example, if the fitted equation is to be a 3rd degree polynomial, then the 4th degree term $\alpha^2\eta\kappa$ will have to be omitted along with every other term with a degree larger than three.

Therefore, if the degree of an approximating polynomial is known, one can proceed to omit the relevant terms, thus simplifying the equation. Plotting the aerodynamic coefficients vs. an input variable whilst keeping the other predictors constant reveals the degree the examined predictor variable should take in the approximating equation. Common convention dictates that a lift-polar is suitably modelled by a cubic curve, whilst the drag and moment coefficients benefit from a lower order quadratic fit in α . The example given in Figure 8.1 satisfies this notion, as is the case for all other simulated parameterised airfoil configurations.

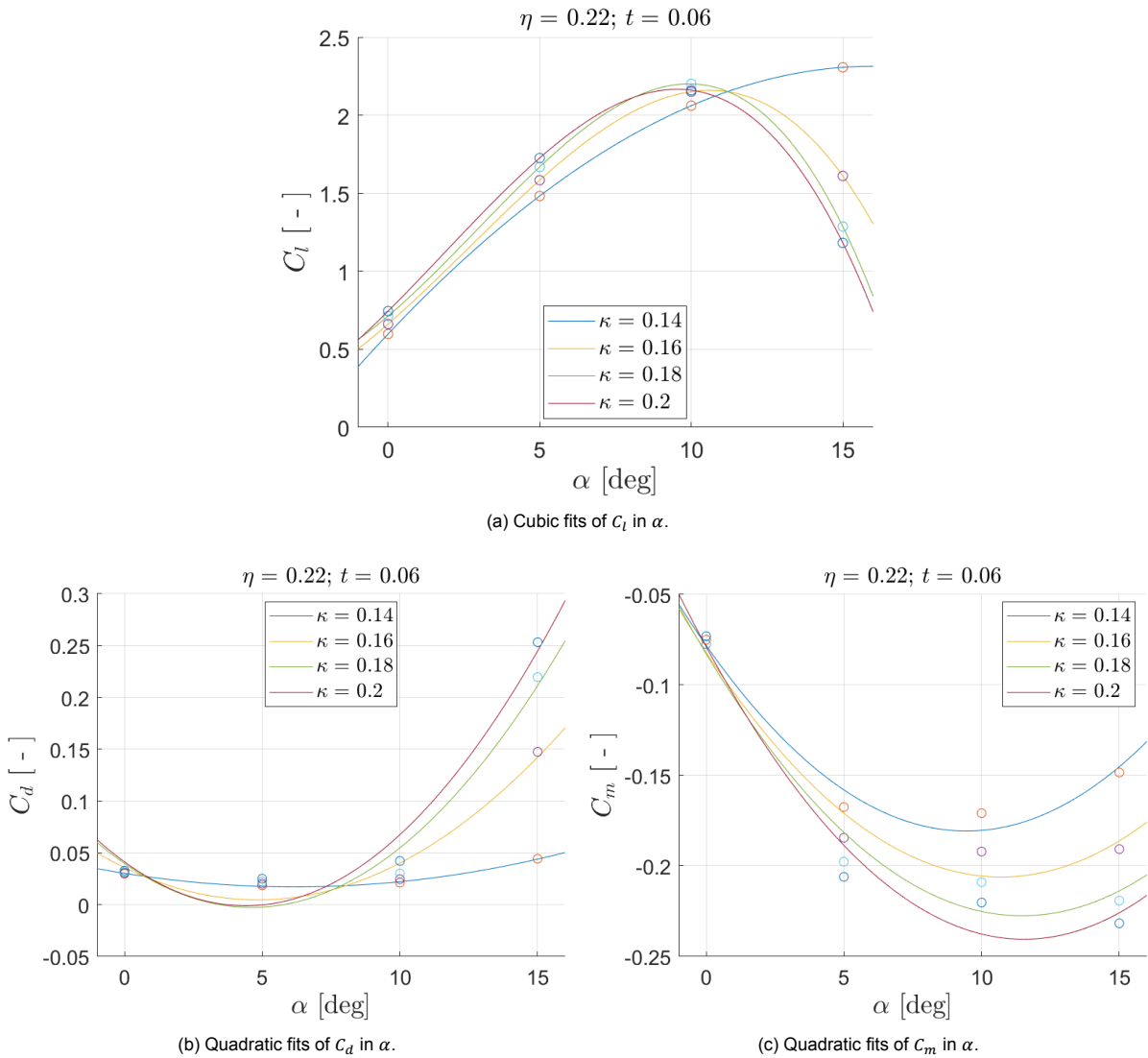


Figure 8.1: Example plots of aerodynamic coefficients versus α given a constant $\eta = 0.22$ and $t = 0.06$.

Determining the degrees of the remaining predictor variables, namely the non-dimensional shape parameters, in the approximating polynomials is less straightforward since general trends are less evident. Nevertheless, either linear or quadratic curves seem to best describe the relations between the aerodynamic coefficients and the shape parameters with the remaining predictor variables kept constant. Based on these observations, the range of suitable approximating polynomials is further narrowed down for the regression analysis.

The numerical data used to calculate the least squares estimates has been acquired from the simulated flow fields of 64 unique parameterised LEI wing profiles, each subjected to four different angles of attack ($\alpha = [0^\circ, 5^\circ, 10^\circ, 15^\circ]$), thus leading to a total of 256 data points. The parameterised profiles were generated using all combinations of $\eta = [0.22, 0.24, 0.26, 0.28]$, $\kappa = [0.14, 0.16, 0.18, 0.20]$ and $t = [0.06, 0.08, 0.12, 0.14]$. The Reynolds number was kept constant at $Re = 5 \times 10^6$ for each simulation.

Whilst the parameter estimates for C_d (see Table 8.2) and C_m (see Table 8.3) seem satisfactory, the inflated estimates of the C_l equation presented in Table 8.1 are indicative of over-fitting. Possible causes are deficiencies in the quality or quantity of the numerical data, or perhaps even the applied statistical method itself is not suitable for modelling in this particular case. Irregardless, it is expected that Equation (8.11) will exhibit poor predictive qualities.

After iterating the regression analyses with different combinations of degrees in the shape parameters, the following approximating polynomials and parameter estimates have been settled upon (α inputs need to be in radians and must not exceed deep stall thresholds):

$$C_l = \hat{\beta}_1 \alpha^3 + \hat{\beta}_2 \alpha^2 + [\hat{\beta}_3 \eta + \hat{\beta}_4 \kappa + \hat{\beta}_5 t + \hat{\beta}_6] \alpha + [\hat{\beta}_7 \kappa + \hat{\beta}_8 t + \hat{\beta}_9] \eta + [\hat{\beta}_{10} t + \hat{\beta}_{11}] \kappa + \hat{\beta}_{12} t^2 + \hat{\beta}_{13} t + \hat{\beta}_{14} \quad (8.11)$$

Table 8.1: Parameter estimates governing Equation (8.11) [$R^2 = 0.9582$, RMSE = 0.1181].

	Value		Value
$\hat{\beta}_1$	-146.2217	$\hat{\beta}_8$	-1.6721
$\hat{\beta}_2$	16.4505	$\hat{\beta}_9$	-2.5755
$\hat{\beta}_3$	16.5034	$\hat{\beta}_{10}$	-9.8052
$\hat{\beta}_4$	-66.1728	$\hat{\beta}_{11}$	4.1254
$\hat{\beta}_5$	2.9489	$\hat{\beta}_{12}$	-0.2872
$\hat{\beta}_6$	16.7412	$\hat{\beta}_{13}$	-0.5613
$\hat{\beta}_7$	11.8057	$\hat{\beta}_{14}$	0.3124

$$C_d = \hat{\beta}_{15} \alpha^2 + [\hat{\beta}_{16} \eta + \hat{\beta}_{17} \kappa + \hat{\beta}_{18} t + \hat{\beta}_{19}] \alpha + [\hat{\beta}_{20} \kappa + \hat{\beta}_{21} t + \hat{\beta}_{22}] \eta + [\hat{\beta}_{23} t + \hat{\beta}_{24}] \kappa + \hat{\beta}_{25} t^2 + \hat{\beta}_{26} t + \hat{\beta}_{27} \quad (8.12)$$

Table 8.2: Parameter estimates governing Equation (8.12) [$R^2 = 0.8971$, RMSE = 0.0184].

	Value		Value
$\hat{\beta}_{15}$	3.7796	$\hat{\beta}_{22}$	0.8397
$\hat{\beta}_{16}$	-2.7567	$\hat{\beta}_{23}$	-0.9996
$\hat{\beta}_{17}$	9.7603	$\hat{\beta}_{24}$	0.6498
$\hat{\beta}_{18}$	-0.3538	$\hat{\beta}_{25}$	-0.0332
$\hat{\beta}_{19}$	-1.5589	$\hat{\beta}_{26}$	0.2367
$\hat{\beta}_{20}$	-3.9806	$\hat{\beta}_{27}$	-0.1214
$\hat{\beta}_{21}$	0.0592		

$$C_m = \hat{\beta}_{28} \alpha^2 + [\hat{\beta}_{29} \eta + \hat{\beta}_{30} \kappa + \hat{\beta}_{31} t + \hat{\beta}_{32}] \alpha + [\hat{\beta}_{33} \kappa + \hat{\beta}_{34} t + \hat{\beta}_{35}] \eta + [\hat{\beta}_{36} t + \hat{\beta}_{37}] \kappa + \hat{\beta}_{38} t^2 + \hat{\beta}_{39} t + \hat{\beta}_{40} \quad (8.13)$$

Table 8.3: Parameter estimates governing Equation (8.13) [$R^2 = 0.9791$, RMSE = 0.0088].

	Value		Value
$\hat{\beta}_{28}$	3.9178	$\hat{\beta}_{35}$	-0.3243
$\hat{\beta}_{29}$	0.6127	$\hat{\beta}_{36}$	2.1179
$\hat{\beta}_{30}$	-4.0266	$\hat{\beta}_{37}$	-0.2190
$\hat{\beta}_{31}$	-1.8405	$\hat{\beta}_{38}$	0.3620
$\hat{\beta}_{32}$	-0.7922	$\hat{\beta}_{39}$	-0.0460
$\hat{\beta}_{33}$	-0.4343	$\hat{\beta}_{40}$	0.0128
$\hat{\beta}_{34}$	0.9448		

Conclusions & Recommendations

As there is no standardised means to generate the shape of a LEI wing profile, unlike the conventional NACA airfoil series for example, the parameterisation and geometric construction of such an unconventional shape should be given a detailed description. Such an explanation is missing from the primary source of the reference aerodynamic load model developed by Breukels [7]. Whilst the general shape of a 2D LEI wing appears to have been parameterised by Breukels [7], the shape parameters have not been explicitly defined. As a result, there have been inconsistencies between the assertions of the primary source and interpretations by users of the model in succeeding studies. In order to alleviate this problem for potential future users, a detailed description of the shape parameterisation and geometric construction can be found in Chapter 5. In this regard, the revised aerodynamic load model is likely an improvement over the original due to relative ease of interpretation.

As for the addition of the chordwise position of maximum camber η as a shape parameter, greater control over the shape of the parameterised LEI wing profile has been granted. Given attached flow over the suction side, increasing η leads to a more negative C_m due to changes in the load distribution whilst C_l and C_d remain effectively the same given a low-to-moderate angle-of-attack. In the case of suction-side flow separation at high angles-of-attack, an increase in η shifts the chordwise position of the separation point further downstream, thus alleviating the loss in lift and reducing the resultant pressure drag. The aforementioned descriptions allude to a discernible impact on the flow field, thus favouring the inclusion of the chordwise position of maximum camber η as a non-dimensional quantity describing the shape of a parameterised LEI wing profile.

The maximum camber magnitude κ has a prominent effect on the flow stability at high angles-of-attack. All simulations of the flow fields around parameterised profiles given $\kappa = 0.3$ and $\alpha = 15^\circ$ did not converge, a phenomenon indicative of exacerbated transient flow effects since converged solutions were acquired from simulations of profiles given $\kappa \leq 0.2$ and $\alpha = 15^\circ$. As such, numerical data acquisition for the regression analysis has been limited to LEI wing profiles that satisfy the $t/2 \leq \kappa \leq 0.2$ condition. Even within this limit, an increase in κ reduces the critical angle-of-attack, leading to an earlier onset of stall.

A strong interdependence between κ and η became evident when generating profiles since the suction-side spline would often overshoot vertically beyond the maximum camber point if there were compatibility issues between the two shape parameters. For this reason, the approach to generating profiles for the purposes of this work was first to establish the range of values for t and then the κ range as these shape parameters have a more dominant effect on the flow field. Then either a suitable range for η would be settled upon after enough iterations, or a new range of values for t and/or κ would be selected and scrutinised according to the same iterative process. Whilst the employed system of interpolation described in Chapter 5 may seem sensitive and limited in scope, it does provide a more firm

foundation since a strong interdependence between κ and η is expected in reality.

Possibilities for further improving the method of parameterisation such that greater control over the shape of a LEI wing profile is granted would be the addition of another possible shape parameter. Namely, the point of intersection between the suction-side spline profile of the canopy and the circular profile of the LE tube, which is represented by the angular position $\theta_{suction}$ relative to the centre of the leading-edge tube. This point dictates the extent to which the circular LE tube profile is present on the suction side of the LEI wing profile. As the suction side of a rigid LEI wing profile shows similar aerodynamic characteristics to a conventional airfoil, further investigation of the effects of altering $\theta_{suction}$ could be warranted for future work. If it follows that $\theta_{suction}$ has a substantial impact on the flow field, there may be a case for its incorporation into an updated aerodynamic load model depending on user demand.

As for the aerodynamic load model developed within the scope of this study (see Chapter 8), evidence of over-fitting necessitates a revision of the applied strategy. Including more data points may potentially lead to an improved model, but the problem may also lie with the applied method of statistical modelling itself. Further research into alternatives to multivariate polynomial regression analysis could facilitate the development of an improved model.

Bibliography

- [1] U. Ahrens, M. Diehl, and R. Schmehl, editors. *Airborne Wind Energy*. Green Energy and Technology. Springer, Berlin Heidelberg, 2013.
- [2] J.D. Anderson. *Fundamentals of Aerodynamics*. McGraw-Hill Series in Aeronautical and Aerospace Engineering. McGraw-Hill, New York, 5th edition, 2011.
- [3] P. Bechtle, M. Schelbergen, R. Schmehl, U. Zillmann, and S. Watson. Airborne wind energy resource analysis. *Renewable Energy*, 141:1103–1116, 2019. ISSN 18790682. doi: 10.1016/j.renene.2019.03.118.
- [4] J. Berens. Dynamic Nonlinear Aeroelastic Behaviour of Flexible Wings in an Airflow. Master's thesis, TU Delft, Delft, The Netherlands, 2015.
- [5] A. Bosch, R. Schmehl, P. Tiso, and D. Rixen. Dynamic nonlinear aeroelastic model of a kite for power generation. *Journal of Guidance, Control, and Dynamics*, 37(5):1426–1436, 2014. ISSN 15333884. doi: 10.2514/1.G000545.
- [6] H.A. Bosch. Finite element analysis of a kite for power generation: Computational modelling of flight dynamics of a tethered wing including non-linear fluid-structure interaction. Master's thesis, TU Delft, Delft, The Netherlands, 2012.
- [7] J. Breukels. *An Engineering Methodology for Kite Design*. PhD thesis, TU Delft, Delft, The Netherlands, 2011.
- [8] J. Breukels and W.J. Ockels. A Multi-Body System Approach to the Simulation of Flexible Membrane Airfoils. *Aerotecnica Missili & Spazio*, 89(3):119–134, 2010. URL <http://www.kitepower.eu/images/stories/publications/breukels10.pdf>.
- [9] G. Buendía. Low and High Fidelity Aerodynamic Simulations for Airborne Wind Energy Box Wings. Master's thesis, TU Delft, Delft, The Netherlands, 2022.
- [10] O. Cayon. Fast aeroelastic model of a leading-edge inflatable kite for the design phase of airborne wind energy systems. Master's thesis, TU Delft & DTU, 2022.
- [11] G. Chen, Q. Xiong, P.J. Morris, E.G. Paterson, A. Sergeev, and Y. Wang. OpenFOAM for Computational Fluid Dynamics. *Notices of the American Mathematical Society*, 61(4):354, 2014. ISSN 0002-9920. doi: 10.1090/noti1095.
- [12] S.J. Collie, M.G. Gerritsen, and M.J. O'Sullivan. Numerical Simulation of the Turbulent Flow Past Upwind Yacht Sails. *Journal of Wind Engineering and Industrial Aerodynamics*, 91(2):185–197, 2002.
- [13] T. Coudou. Numerical modeling of inflatable airborne wind energy systems. Master's thesis, Faculté Polytechnique de Mons, 2017.
- [14] S.G.C. de Groot, J. Breukels, R. Schmehl, and W.J. Ockels. Modeling kite flight dynamics using a multibody reduction approach. *Journal of Guidance, Control, and Dynamics*, 34(6):1671–1682, 2011. ISSN 15333884. doi: 10.2514/1.52686.
- [15] M. Deaves. An Investigation of the Non-Linear 3D Flow Effects Relevant for Leading Edge Inflatable Kites. Master's thesis, TU Delft & DTU, 2015.

- [16] P. Demkowicz. Numerical analysis of the flow past a leading edge inflatable kite wing using a correlation-based transition model. Master's thesis, TU Delft, Delft, The Netherlands, 2019.
- [17] R.G. den Boer. Low speed aerodynamic characteristics of a two-dimensional sail wing with adjustable slack of the sail. Technical report, Technische Hogeschool Delft, Delft, Netherlands, 1980. URL <http://repository.tudelft.nl/view/ir/uuid:18ae2cc6-434e-49c8-9296-d3fa450850a5/>.
- [18] N.R. Draper and H. Smith. *Applied Regression Analysis*. Wiley Series in Probability and Statistics. John Wiley & Sons, Inc., New York, 3rd edition, 1998.
- [19] J.H. Ferziger, M. Perić, and R.L. Street. *Computational Methods for Fluid Dynamics*. Springer, Cham, Switzerland, 4th edition, 2020.
- [20] M. Folkersma. *Aeroelasticity of Membrane Kites - Airborne Wind Energy Applications*. PhD thesis, TU Delft, Delft, The Netherlands, 2022.
- [21] M. Folkersma, R. Schmehl, and A. Viré. Boundary layer transition modeling on leading edge inflatable kite airfoils. *Wind Energy*, 22(7):908–921, 2019. ISSN 10991824. doi: 10.1002/we.2329.
- [22] M. Folkersma, R. Schmehl, and A. Viré. Steady-state aeroelasticity of a ram-air wing for airborne wind energy applications. *Journal of Physics: Conference Series*, 1618(3), 2020. ISSN 17426596. doi: 10.1088/1742-6596/1618/3/032018.
- [23] G.H. Golub and C.F. van Loan. *Matrix Computations*. Johns Hopkins University Press, Baltimore, Maryland, 3rd edition, 1996.
- [24] A. Gouttière. Direct numerical simulation of flow around wind energy harvesting kites. Master's thesis, Faculté Polytechnique de Mons, 2019.
- [25] J.D. Hobby. Smooth, Easy to Compute Interpolating Splines. *Discrete & Computational Geometry*, 1:123–140, 1986.
- [26] S. Jamshed. *Using HPC for computational fluid dynamics: a guide to high performance computing for CFD engineers*. Academic Press, Waltham, MA, 2015.
- [27] R.B. Langtry and F.R. Menter. Correlation-based transition modeling for unstructured parallelized computational fluid dynamics codes. *AIAA Journal*, 47(12):2894–2906, 2009. ISSN 00011452. doi: 10.2514/1.42362.
- [28] B.E. Launder and D.B. Spalding. The Numerical Computation of Turbulent Flows. *Computer Methods in Applied Mechanics and Engineering*, 3:269–289, 1974. URL <https://www.researchgate.net/publication/312919474>.
- [29] G. Lebesque. Steady-state RANS simulation of a leading edge inflatable wing with chordwise struts. Master's thesis, TU Delft, Delft, The Netherlands, 2020.
- [30] F.R. Menter. Zonal Two Equation $k - \omega$ Turbulence Models for Aerodynamic Flows. *AIAA Paper 93-2906*, pages 1–22, 1993.
- [31] F.R. Menter. Two-equation eddy-viscosity turbulence models for engineering applications. *AIAA Journal*, 32(8):1598–1605, 1994. ISSN 00011452. doi: 10.2514/3.12149.
- [32] F.R. Menter, M. Kuntz, and R. Langtry. Ten Years of Industrial Experience with the SST Turbulence Model. *Turbulence, Heat and Mass Transfer*, 4, 2003.
- [33] J. Oehler and R. Schmehl. Aerodynamic characterization of a soft kite by in situ flow measurement. *Wind Energy Science*, 4(1):1–21, 2019. doi: 10.5194/wes-4-1-2019.
- [34] S.V. Patankar. *Numerical Heat Transfer and Fluid Flow*. Hemisphere Publishing Corporation, Washington, D.C., 1980.

- [35] S.V. Patankar and D.B. Spalding. A Calculation Procedure for Heat, Mass and Momentum Transfer in Three-Dimensional Parabolic Flows. *Int. J. Heat Mass Transfer*, 15:1787–1806, 1972.
- [36] S.B. Pope. *Turbulent Flows*. Cambridge University Press, Cambridge, 2000.
- [37] S. Sachdeva. Impact of Turning-Induced Shape Deformations on Aerodynamic Performance of Leading Edge Inflatable Kites. Master's thesis, TU Delft, Delft, The Netherlands, 2017.
- [38] R. Schmehl, editor. *Airborne Wind Energy: Advances in Technology Development and Research*. Green Energy and Technology. Springer, Singapore, 2018.
- [39] R. Smith and W. Shyy. Computation of aerodynamic coefficients for a flexible membrane airfoil in turbulent flow: A comparison with classical theory. *Physics of Fluids*, 8(12):3346–3353, 1996. ISSN 10706631. doi: 10.1063/1.869122.
- [40] G. Spierenburg. Continued Development and Experimental Validation of a Kite Design and Simulation Tool. Master's thesis, TU Delft, Delft, The Netherlands, 2005.
- [41] J.P. van Doormaal and G.D. Raithby. Enhancements of the SIMPLE Method for Predicting Incompressible Fluid Flows. *Numerical Heat Transfer*, 7:147–163, 1984.
- [42] R.H.M. van Kappel. Aerodynamic Analysis Tool for Dynamic Leading Edge Inflated Kite Models: A Non-Linear Vortex Lattice Method. Master's thesis, TU Delft, Delft, The Netherlands, 2012.
- [43] A. Viré, P. Demkowicz, M. Folkersma, A. Roullier, and R. Schmehl. Reynolds-averaged Navier-Stokes simulations of the flow past a leading edge inflatable wing for airborne wind energy applications. *Journal of Physics: Conference Series*, 1618(3), 2020. ISSN 17426596. doi: 10.1088/1742-6596/1618/3/032007.
- [44] A. Viré, G. Lebesque, M. Folkersma, and R. Schmehl. Effect of Chordwise Struts and Misaligned Flow on the Aerodynamic Performance of a Leading-Edge Inflatable Wing. *Energies*, 15(4), 2022. ISSN 19961073. doi: 10.3390/en15041450.
- [45] F.M. White. *Viscous Fluid Flow*. McGraw-Hill, New York, NY, 3rd edition, 2006.
- [46] F.M. White. *Fluid Mechanics*. McGraw-Hill, New York, NY, 7th edition, 2011.